EXPERIMENTAL INVESTIGATION OF ULTRA-HIGH-PERFORMANCE CONCRETE PANELS UNDER TORNADO IMPACT LOADS

by

HANNAH ROSE KNIFFIN

SRIRAM AALETI, COMMITTEE CHAIR
ARMEN AMIRKHANIAN
SAAHASTARANSHU BHARDWAJ
VISHESH VIKAS

A THESIS

Submitted in partial fulfilment of the requirements
for the degree of Master of Science in the Department of
Civil, Construction, and Environmental Engineering
in the Graduate School of
The University of Alabama

TUSCALOOSA, ALABAMA

2021

Copyright Hannah Rose Kniffin 2021
ALL RIGHTS RESERVED

ABSTRACT

Tornado events pose a threat to millions of people living in the tornadic-prone areas of the United States. Although many tornado shelters and safe rooms are commercially available that satisfy the extreme loading conditions required by the International Code Council and National Storm Shelter Association, there is a need for a simple yet safe design which can be easily assembled and used for multiple purposes. New engineering materials, such as ultra-high-performance concrete (UHPC), have the potential to improve tornado shelter options and save lives. This study experimentally investigates the performance of thin UHPC panels subjected to impact of standard wood 2x4 projectiles, following the requirements of ICC/NSSA 500, the leading standard on storm shelter design. 1.25-inch-thick and 1.625-inch-thick UHPC panels were cast and impacted with 15-lb wood projectiles at speeds ranging from 50 mph to 100 mph to maintain a similar impact-energy-to-panel-mass ratio. The failure response of each panel was characterized by excessive flexural deflection or punching shear. In the case of excessive deflection, a single-degree-of-freedom dynamic displacement model describes the motion of the panel during impact and the profile of the maximum deflection. In the case of punching shear, a modified equation from ACI 318 predicts the capacity of the panel. The results of the impact testing show UHPC is a promising material for future tornado shelters: UHPC panels with half the thickness of a traditional concrete shelter can be built for a similar or lower price, creatively integrated into homes, and increase accessibility of the tornado shelter for residents.

LIST OF ABREVIATIONS AND SYMBOLS

CDC	Centers for Disease Control and Prevention
FHWA	Federal Highway Administration
FPL	Forest Products Laboratory
ICC	International Code Council
NAHB	National Association of Home Builders
NEI	Nuclear Energy Institute
NOAA	National Oceanic and Atmospheric Administration
NSSA	National Storm Shelter Association
NSSL	National Severe Storms Laboratory
NWS	National Weather Service
UCAR	University Corporation for Atmospheric Research
UHPC	Ultra-High-Performance Concrete
UHPFRC	Ultra-High-Performance Fiber-Reinforced Concrete
USDA	United States Department of Agriculture
USDOC	United States Department of Commerce
a	Coefficient of drag or shape factor
b_o	Critical perimeter of punching shear failure
b_w	Width of beam
C_p	External pressure coefficient
DFE	Design flood elevation

DFE_o	Minimum design flood elevation
d	Depth of steel in panel
d_h	Surcharge depth
E	Modulus of elasticity
F	Flood load
F_{AVG}	Average force of impact
f'_c	Compressive strength of concrete
f_t	Tensile strength of concrete
G	Gust-effect factor
GC_{pi}	Product of internal pressure coefficient and gust-effect factor
g	Gravity constant
h	Thickness of panel
I	Bending moment of inertia
J	Impulse
J_o	Impulse delivered by impact
K_d	Wind directionality factor
K_Z	Velocity pressure exposure coefficient at height *z*
k	Stiffness of panel
k_{zt}	Topographic factor
L	Length of column
M	Mass of panel

m	Mass of projectile
n	Number of peaks
p	Pressure
p_o	Force delivered by impact
q	Velocity pressure
t	Time
t_d	Time of impact duration
u	Displacement of panel over time
u_p	First peak displacement
u_{p+n}	n^{th} peak displacement
V	Basic wind speed
V_c	Shear strength of concrete
v	Average velocity of flood water
v_1	Projectile outgoing velocity
v_2	Projectile incoming velocity
W	Wind speed
y	Height from center of panel
γ	Specific weight of water
Δt	Change in time
Δv	Change in projectile velocity
$\Delta(y)$	Deflection along height of panel
ζ	Damping ratio

φ	Strength reduction factor
ω_d	Damped frequency
ω_n	Natural frequency

ACKNOWLEDGEMENTS

Thank you to the University of Alabama, College of Engineering, and Department of Civil, Construction, and Environmental Engineering for the generous resources provided to their students. Having access to large-scale testing facilities as well as innumerable scientific publications was crucial to the success of this project. Thank you also to Dr. Lawrence Powell, Director of the Alabama Center for Insurance Information and Research, for providing financial support to conduct this research.

To my committee members, Drs. Armen Amirkhanian, Saahastaranshu Bhardwaj, and Vishesh Vikas, thank you for your academic guidance and expertise. Thank you especially to Dr. Sriram Aaleti, my lead committee member and principal investigator, for supporting me through the master's thesis process as well as previously in my undergraduate studies. First as a structural analysis professor, then as a research lab director, and finally as a graduate level mentor, the countless hours you have spent teaching and challenging me have been instrumental to my growth as a young engineer.

This project would not be possible without the help of my other lab group members: thank you to Barry Battle and Sumedh Sharma for your deep knowledge of the lab and always being available to help around my unpredictable schedule; to Daniel Valentim and Gabi Willis for teaching me about instrumentation and data analysis techniques; and to Allie Ćemalović, Dedrick Minniefield, Emma Hutcheson, JJ Beasley, and Ryan Hastings for being an extra set of hands to cut, drill, lift, and move things.

Finally, thank you to my amazing family for loving me through the ups and downs of this crazy past year. Mom, Dad, Erin, Lexi, and Jordan – if we can make it through 2020/2021 together, we can make it through anything!

CONTENTS

ABSTRACT ii

LIST OF ABREVIATIONS AND SYMBOLS iii

ACKOWLEDGEMENTS vii

LIST OF EQUATIONS xii

LIST OF FIGURES xiii

INTRODUCTION 1

Tornados and Their Deadliness 1

Current Tornado Shelter Options 5

Ultra-High-Performance Concrete 14

Research Objectives 18

LITERATURE REVIEW 20

Experimental Studies 20

Numerical and Analytical Models 52

EXPERIMENTAL PROGRAM 64

Specimen Design 64

Panel dimensions 64

UHPC type 70

Fiber type and content 73

Steel reinforcement 75

Summary of panel parameters 76
Experimental Test Setup 77
Debris cannon 78
Projectiles and impact velocity 78
Steel frame and panel attachment 81
Witness frame 83
Instrumentation and measurements 84
Summary of experimental setup 88
Material Properties Testing 90
Compressive strength 90
Flexural strength 92
RESULTS AND DISCUSSION 95
Impact Testing of UHPFRC Panels 95
Preliminary panel results 95
Displacement-time response and dynamic modeling 95
Profile of maximum deflection 104
Punching shear failure 109
Pass/fail analysis 112
Material Properties Testing Results 113
Compressive testing results 113
Four-point-bending results 114
CONCLUSIONS 118
Experimental Conclusions 118

Applications and Discussion 120

Further Studies 122

REFERENCES 123

APPENDIX: LOAD CALCULATIONS 129

Wind Load 129

Flood Load 131

Load Combinations 131

RISA 2D Diagrams 132

Moment Capacity of Panel 135

Shear Capacity of Panel 136

Comparison 136

APPENDIX: IMPACT TESTING PHOTOS 137

LIST OF EQUATIONS

1. Kinetic Energy of Projectile 80

2. Impulse-Momentum Relationship 97

3. Force-Impulse Relationship 97

4. Fix-Pin Column Stiffness 99

5. Fix-Fix Column Stiffness 99

6. Damping Ratio 100

7. Displacement Response due to Unit Impulse Load 100

8. Displacement Response due to Rectangular Pulse Load 100

9. Damped Frequency and Natural Frequency 104

10. Beam-Point-Load Deflection 105

11. ACI 318 Punching Shear 112

12. Tensile-Based Punching Shear 112

13. Modified ACE 318 Punching Shear 112

14. ASCE 7-10 Velocity Pressure 130

15. ASCE 7-10 Design Wind Pressure 130

16. ASCE 7-10 Equivalent Surcharge Depth 131

17. ASCE 7-10 Design Flood Elevation 131

18. ASCE 7-10 Hydrostatic Pressure 131

19. ACI 318 Shear Capacity 136

LIST OF FIGURES

1. Tornado Deaths by Year in the United States (NOAA, 2020) 2

2. Map of Tornado and Dixie Alley 3

3. Formation of Tornados 4

4. Tornado Deaths by Year in the United States, by Amount in Homes (NOAA, 2020) 5

5. Map of Tornado Design Wind Speeds and Associated Debris Impact Speeds (Julian, 2014) 6

6. Survive-a-Storm Shelters 7

7. Atlas Safe Rooms 8

8. Vortex Vaults 9

9. Safe Sheds 10

10. Protection Shelters 11

11. USDA/FPL Dimension Lumber Shelter 12

12. Price versus Occupancy of Tornado Shelters 13

13. Map of UHPC Bridges in the United States and Canada 16

14. Institutional-Scale Architectural Applications of UHPC 17

15. Residential and Light Commercial Architectural Applications of UHPC 17

16. Decorative Interior Residential Applications of UHPC 18

17. Deformable Steel Missile, Assembled and Segmented (Riedel et al., 2010) 21

18. Geometry of UHPC Panels and Reinforcement (Riedel et al., 2010) 21

19. Missile and Panel Details for Experimental Configuration (Riedel et al., 2010) 21

20. Experimental Configuration (Riedel et al., 2010) 22

21. Summary of Test Results (Riedel et al., 2010) 23

22. Comparison of UHPC and Normal Concrete #1 After Impact (Riedel et al., 2010) 23

23. Comparison of UHPC and Normal Concrete #2 After Impact (Riedel et al., 2010) 24

24. Stress versus Crack Opening Width (Riedel et al., 2010) 25

25. Mechanical Properties of UHPC Panels (Verma et al., 2016) 26

26. Experimental Setup of Drop Weight ImpactTests (Verma et al., 2016) 27

27. Table of Experimental Results (Verma et al., 2016) 27

28. Impact-Force-Time History of UHPC Panels (Verma et al., 2016) 28

29. Comparison of Strain Model and Experimental Crack Pattern (Verma et al., 2016) 30

30. Energy Balance of Impact (Verma et al., 2016) 31

31. Experimental versus SDOF and TDOF Force-Time Histories (Verma et al., 2016) 32

32. Flow Chart for Designing UHPC Panels Subject to Impact Load (Verma et al., 2016) 33

33. 8 ft by 8 ft and 5.5 ft by 5.5 ft CLT Shelters (Falk et al., 2019) 38

34. Assembly Hardware (Falk et al., 2019) 38

35. Debris Impact Cannon (Falk et al., 2019) 39

36. 3-Ply CLT Results (Falk et al., 2019) 40

37. 4-Ply CLT Results (Falk et al., 2019) 41

38. Wind Pressure Testing Setup (Falk et al., 2019) 42

39. Displacements from Wind Pressure and Uplift Testing (Falk et al., 2019) 43

40. Specimen Dimensions (Beppu et al., 2020) 46

41. Launching Test Machine and Steel Projectile (Beppu et al., 2020) 47

42. Failure State of 60 mm (2.36 inch) UHPFRC Panels (Beppu et al., 2020) 48

43. Failure State of 90 mm (3.54 inch) UHPFRC Panels (Beppu et al., 2020) 49

44. Failure State of 120 mm (4.72 inch) UHPFRC Panels (Beppu et al., 2020) 50

45. Measured Data from 90 mm Panels (Beppu et al., 2020) 51

46. Three- and Four-Point-Bending Test Setups (Habel and Gauvreau, 2008) 53

47. Drop Weight Test Setup (Habel and Gauvreau, 2008) 53

48. Definition of Model Parameters (Habel and Gauvreau, 2008) 54

49. Mass-Spring Model and Equations of Motion (Habel and Gauvreau, 2008) 54

50. Results of Three- and Four-Point-Bending Tests (Habel and Gauvreau, 2008) 55

51. Time Evolution of Deflected Shape and Strain (Habel and Gauvreau, 2008) 51

52. Model versus Experimental Results (Habel and Gauvreau, 2008) 57

53. Finite Element Models of Panel, Rebar Cage, and Steel Impactor (Thai and Kim, 2016) 59

54. Winfrith Model Factors and Stress-Strain Curves (Thai and Kim, 2016) 60

55. Comparison of Model and Experimental Results (Thai and Kim, 2016) 61

56. Minimum Thickness to Prevent Scabbing (Thai and Kim, 2016) 62

57. Minimum Thickness to Prevent Perforation (Thai and Kim, 2016) 63

58. Formworks of Each Panel Size 70

59. Bags of UHPC Types 71

60. Mixing Procedure of UHPC 72

61. Fiber Types 74

62. Steel Reinforcement Types 76

63. Summary of UHPFRC Panel Specifications 76

64. Debris Cannon 77

65. Air Compressor Control Board 78

66. 2x4 Projectile 79

67. Speed Gates and Free Flight Velocity versus Pressure Graph....81

68. Steel Frame....82

69. Panels Clamped to Steel Frame....83

70. Witness Frame....84

71. Strain Gauge Configuration Map....85

72. Strain Gauges....86

73. Colored Markers on Side of Panel....87

74. Experimental Setup of Debris Cannon Laboratory....88

75. Summary of Impact Testing Parameters for Each Panel....89

76. Compression Cubes and Testing Machine....91

77. Loading Frame for Four-Point-Bending....93

78. Experimental Setup of Four-Point-Bending Tests....94

79. Kinovea Analysis of Projectile Motion....96

80. Displacement-Time Response of Panel....98

81. SDOF Stiffness Models....99

82. Comparison of Dynamic Models....102

83. Experimental Displacement-Time Histories versus Dynamic Model....103

84. Kinovea Analysis of Maximum Deflection Profile....106

85. Experimental Deflection Profile versus Beam-Point-Load Models....108

86. Punching Shear Failure Mechanism....110

87. Punching Shear Failure of Panel....111

88. Comparison of Punching Shear Capacity Equations....112

89. Pass/Fail Analysis of Each Panel....113

90. Compression Testing Results 114

91. Four-Point-Bending Results for AS1 and AS2 115

92. Four-Point-Bending Results for SS1, SS2, and SS3 116

93. Four-Point-Bending Results for SB1 and SB2 117

94. Price versus Occupancy of Tornado Shelters, Including Proposed UHPFRC Shelter 121

95. Summary of Wind Load Parameters 130

96. Summary of Flood Load Parameters 131

97. Loading and Response of Windward Wall Panel 133

98. Loading and Response of Rood Panel 134

99. Stress Distribution through UHPC Cross-Section 135

100. AG_2x12 Impact Testing Photos 137

101. AS_2x12 Impact Testing Photos 138

102. AS_1.25x12 Impact Testing Photos 139

103. AS_1.625x12 Impact Testing Photos 140

104. AS_1.25x24 Impact Testing Photos 141

105. AS_1.625x24 Impact Testing Photos 142

106. SS_1.25x12 Impact Testing Photos 143

107. SB_1.25x12 Impact Testing Photos 144

INTRODUCTION

Tornados and Their Deadliness

On April 27th, 2011, Tuscaloosa, Birmingham, and their surrounding towns suffered incredible loss of life and destruction of property in the wake of an EF-4 tornado. Traveling for over 80 miles with maximum wind speeds estimated at 190 mph, the tornado leveled homes, businesses, and schools. Sixty-five fatalities were attributed to the storm (NOAA, 2016). Ten years later, the memory of the destruction still haunts students, faculty, and town residents that lived through the event, and affects the behaviors of Tuscaloosa natives and newcomer alike. As of the writing of this thesis, the University of Alabama has already experienced one major weather event in the Spring of 2021: EF-1 tornado damage was observed in Moundville, AL, just 20 miles south of campus, with promises of severe weather in the city of Tuscaloosa sending near-capacity amounts of people to community and campus storm shelters (WBRC Staff, 2021 and CW Staff, 2021).

Although the 2011 Tuscaloosa-Birmingham storm is widely known in the Tuscaloosa and University of Alabama community, it was, tragically, not the most lethal tornado in Alabama or in the nation that year. An EF-5 tornado ravaged the Huntsville area just hours before on that same day, killing 72 people; later that spring, Jasper County, Missouri lost 158 lives in an EF-5 tornado on May 22nd (NOAA, 2020). **Figure 1** shows tornado fatality data collected by the National Ocean and Atmospheric Administration (NOAA) and the National Weather Service (NWS) from 1991, the year that they began publishing this data, to 2020, the most current completed year (NOAA, 2020). Tornados were responsible for 2072 deaths in the 30-year span

presented. These deaths, though concentrated in areas with well-known tornadic activity such as Tornado Alley and Dixie Alley (shown in **Figure 2**, courtesy of Gagan et al., 2010), include people from all over the United States, reaching as far as North Dakota, New Mexico, Florida, and Massachusetts (NOAA, 2020). Tornados, although of critical concern to the University of Alabama and South Eastern Conference communities, bring loss of life and property throughout our nation and deserve to be studied knowing that any new knowledge will be useful nationwide.

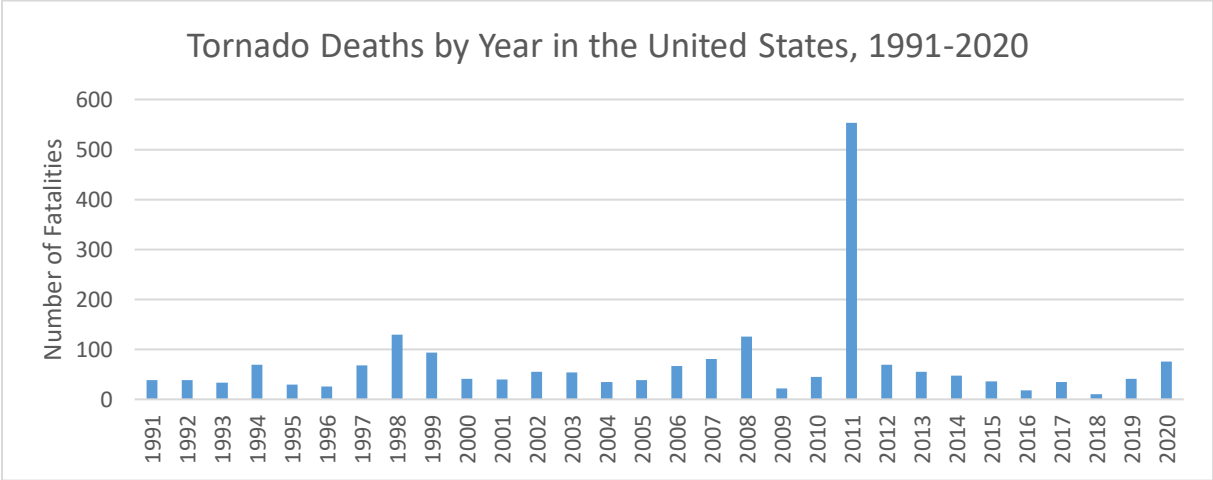

Figure 1: Tornado deaths by year in the United States (NOAA, 2020).

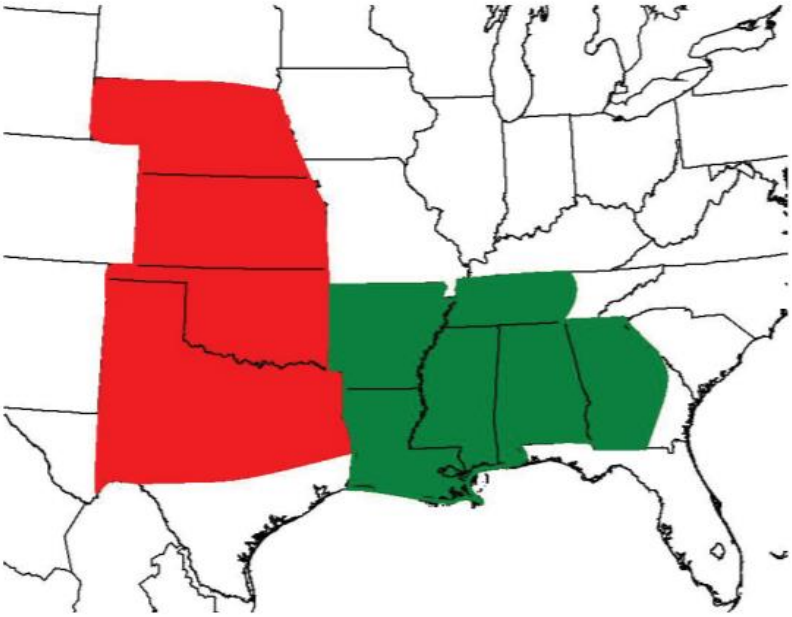

Figure 2: Map of Tornado and Dixie Alley. Tornado Alley, shown in red, and Dixie Alley, shown in green (Gagan et al., 2010).

In their series "Severe Weather 101," the National Severe Storms Laboratory (NSSL) explain the basics on tornado formation, detection, and forecasting, among other topics. The most severe tornados often form from supercell thunderstorms, though powerful tornados can also form from non-supercell storms. Wind shear caused by winds moving at different speeds at and above the ground eventually form a rotating column of horizontal air, that tilts vertically as air rises within the thunderstorm (NOAA, "Types of Tornados"). This process is shown in **Figure 3**, courtesy of the University of Corporate Atmospheric Research (UCAR). According to the NSSL, meteorologists rely on radar signatures that identify large rotating updrafts and other conditions favorable to tornados to predict where a tornado may touchdown; the meteorologists also use debris detecting radar to say with a "high degree of confidence" that a tornado has formed (NOAA, "Tornado Detection"). Tornado forecasting utilizes large computer models of the atmosphere to predict tornado-favorable conditions. Although these models are powerful,

predictions can often only be made a few hours to days before the tornadic activity is expected and tornado scientists are hindered by the fact that many questions still exist about the mechanisms of tornado formation (NOAA, “Tornado Forecasting” and “Types of Tornados”). The overall unpredictability of tornados makes it challenging for public officials to direct people who may be in danger. With only a few hours’ notice of severe conditions, evacuation is almost always impossible. People instead must rely on shelters that are accessible within that time frame, including community storm shelters and personal residential storm shelters. Of course, a few hours’ notice cannot be given for an actual tornado, but only for the promise that a tornado is likely; the current average lead time for an actual tornado strike is 13 minutes (USDOC, 2011). Within 13 minutes, people are narrowed to mostly one option: a tornado shelter on or within a short walk of their property (such as a neighbor’s home).

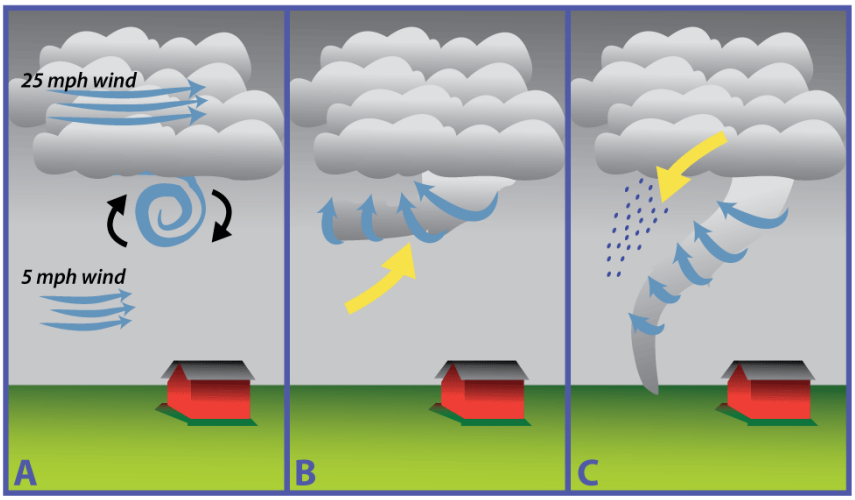

Figure 3: Formation of tornados. Scientists believe tornados may form when (A) wind shear produces a rotating column of horizontal air, (B) rising air from the storm begins to tilt the column vertically, and (C) the column of air contacts the ground (UCAR, n.d.).

The limited reaction time does a lot to explain the deadliness of tornados in the United States. The data from **Figure 1** is re-presented below in **Figure 4**, now with the fatalities

separated by those that happened within a person's home (including site-built homes and mobile homes) and those that happened elsewhere (outside, in vehicles, etc.). Since the NOAA began formally collecting data in 1991, only two years have seen a larger share of deaths outside of homes than in homes (1991 and 2018); and, over the 30-year period, nearly 75% of total deaths occurred in a home. Clearly people in tornado-prone regions are at high risk when they choose to stay in their homes during extreme weather events.

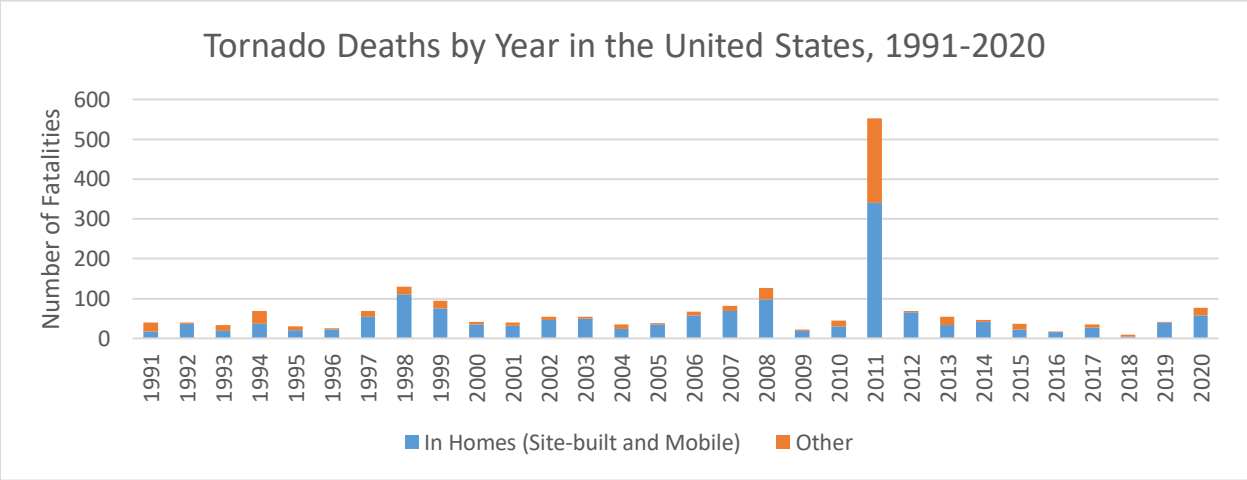

Figure 4: Tornado deaths by year in the United States, by amount in homes (NOAA, 2020).

Current Tornado Shelter Options

For those that choose to stay in their homes during a severe weather event, there is plenty of advice on where to shelter. The Centers for Disease Control and Prevention (CDC) recommend sheltering in a basement or interior room on the lowest level of the home, preferably without windows and under a sturdy piece of furniture, as "falling and flying debris cause most deaths and injuries during a tornado" (CDC, 2021). Typical residential construction, however, does not come close to meeting tornado shelter design criteria, especially regarding impact resistance. In ICC 500-2014: Standard for the Design and Construction of Storm Shelters, the International Code Council (ICC) and the National Storm Shelter Association (NSSA) define the

required impact resistance in the most tornado-prone areas (shown in **Figure 5**) as being hit by a 15-pound 2x4 lumber at 100 mph without showing perforation or ejecting debris from the interior surface (Julian, 2014). The most interior place in a typical wood-frame house, such as a closet or bathroom, may have two or three walls between those sheltering and any flying debris: as will be discussed later, two or three 5-inch walls consisting of drywall, plywood, insulation, and paint will not stop a 100-mph wood projectile.

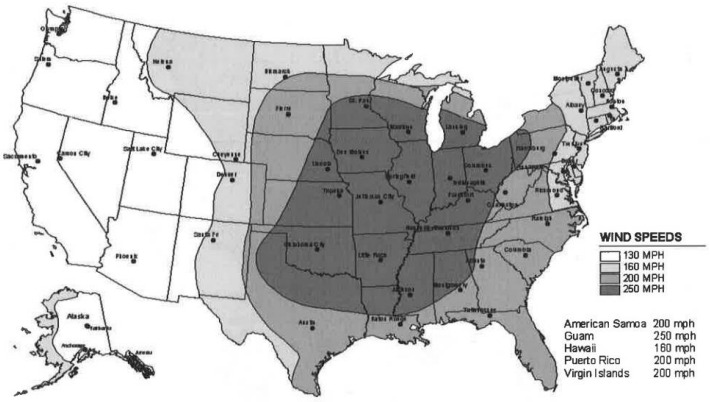

DESIGN WIND SPEED	MISSILE SPEED AND SHELTER IMPACT SURFACE
130 mph	80 mph Vertical Surfaces 53 mph Horizontal Surfaces
160 mph	84 mph Vertical Surfaces 56 mph Horizontal Surfaces
200 mph	90 mph Vertical Surfaces 60 mph Horizontal Surfaces
250 mph	100 mph Vertical Surfaces 67 mph Horizontal Surfaces

Figure 5: Map of tornado design wind speed and associated debris impact speeds (Julian, 2014).

Investing in a residential tornado shelter offers significantly more protection than other in-home "hideouts." Countless companies in the United States offer custom tornado shelters that adhere to the ICC 500-2014 standards and can therefore be marketed as life-saving structures. These shelters come in a wide variety of materials, sizes, and features: just a small sampling of common options is presented here.

Steel plate shelters are one popular type of storm shelter. Companies such as Survive-a-Storm Shelters, based in Georgia but with offices in 35 other states, offer traditional prefabricated ¼" steel plate shelters in a variety of sizes and installation options. Above ground options, installed on an existed concrete pad such as a patio or garage floor, fit between 4 and 16

people: the smallest shelter weighs 980 lbs and costs $3,695 while the largest weights 2,900 lbs and costs $7,295. One benefit of the above ground shelters is the ability to uninstall and move the shelter to a new location when the family moves, but one con is that the shelter is a permanent fixture that takes up floor space even when there is no active storm. Below ground options hold between 10 and 32 people, with the smallest shelter weighing 3,000 lbs for $6,995 and the largest weighing 7,800 lbs for $24,995. The pros and cons of the below ground shelters are the reverse of the above ground shelters: being below ground, the shelters are unobtrusive on a daily basis, but cannot be easily moved if the family moves to a new house (Harbor Enterprises, 2021).

Figure 6: Survive-a-Storm Sheltters. Two above ground (top) and below ground (bottom) steel shelter options offered by Survive-a-Storm Shelters (Harbor Enterprises, 2021).

Another steel plate shelter manufacturer is Atlas Safe Rooms, based in Missouri, which also offers above ground shelters that fit between 2 and 14 people for $4,295 to $7,295, respectively. Like Survive-a-Storm Shelters, Atlas Safe Rooms shelters can be installed on any suitable existing concrete pad in a home. Atlas's defining feature is its modular design where most of the panels can be removed from inside the shelter, allowing for multiple emergency exits in case of debris blockage and flexible installation in existing structures (Atlas Safe Rooms, n.d.).

Figure 7: Atlas Safe Rooms. The smallest (left) and largest (right) shelter options, highlighting the modular panel design (Atlas Safe Rooms, n.d.).

A final steel storm shelter option places daily usability and convenience at the center of its design. Vortex Vaults offers telescoping steel plate shelters than double as workstations and bed frames to maximize the functionality of the shelter during non-tornado days and to significantly reduce travel time to the shelter in case of a severe weather event. Like the other two steel shelters discussed, Vortex Vaults can anchor to an existing concrete slab. The "Project Station" fits five occupants for $6,000; the "3-Tier Bed" model fits seven occupants under a king-sized mattress while the "Slope Top Bed Shelter" fits four – no price information is given for these models (Life Lift Systems, n.d.).

Figure 8: Vortex Vaults. The "Project Station" model in the shelter (top left) and day-to-day (top right) positions; and the "3-Tier Bed" model in the shelter (bottom left) and day-to-day (bottom right) positions (Life Lift Systems, n.d.).

The other most common material for storm shelter design is reinforced normal strength concrete. Concrete shelters tend to be stand-alone structures that can be constructed outside of the actual residence. A classic example of a dedicated concrete tornado shelter is constructed by Safe Sheds, a company based in Illinois. Safe Sheds offers prefabricated reinforced concrete shelters with 4-inch-thick walls and a 6-inch-thick integrated floor. By including a thicker floor and casting the shelter as one piece, the shelter can be installed on "any level surface" on the property even without an existing concrete pad and anchored into the ground with 4 ft steel rods. Two sizes are offered – a 6 ft by 6 ft shelter that fits 9 people for $4,150 or an 8 ft by 10 ft shelter that fits 16 people for $5,750 (Safe Sheds, n.d.).

Figure 9: Safe Sheds. A concrete tornado shelter installed by Safe Sheds, anchored into a gravel yard (Safe Sheds, n.d.).

Another concrete tornado shelter option comes from Protection Shelters in Kansas, who offers both above and quasi-below ground options. The above ground options are very similar to those offered by Safe Sheds, featuring 4-inch-thick reinforced concrete walls in a stand-alone shelter building. One main difference is that Protection Shelters structures require a concrete pad to anchor to, whether existing or poured by the company during installation. Available sizes include 4 ft by 8 ft and 6 ft 8 inch by 6 ft 8 inch, which would hold approximately 6 and 8 people, respectively, based on the ICC 500-2014 occupancy density requirement of 5 square feet per person. The below ground options are also separate from the main residential structure and feature above ground entrances, meaning that the top half of the shelter is still above ground. The below ground options feature 4-inch-thick walls and a staircase, but Protection Shelters does not provide sizing options as these shelters are often custom built. No price information is included for any of the shelter options (Protection Shelters, 2020).

Figure 10: Protection Shelters. Left, above ground and right, quasi-below ground options (Protection Shelters, 2020).

For the more adventurous homeowner, a do-it-yourself wooden tornado shelter was developed by the United States Department of Agriculture (USDA) and Forest Products Laboratory (FPL) to be constructed from materials found at most home improvement stores. The design involves an interlocking beam system, plywood sheathing, standard nails and construction adhesive, as well as the tie-downs necessary to anchor to a concrete slab. The 8 ft by 8 ft shelter is expected to cost between $3,000 and $4,000 depending on local market prices and could hold approximately eight people following occupant density requirements set in ICC 500-2014. Although potentially very cost-effective, this option does require some skill in construction (NAHB, 2019).

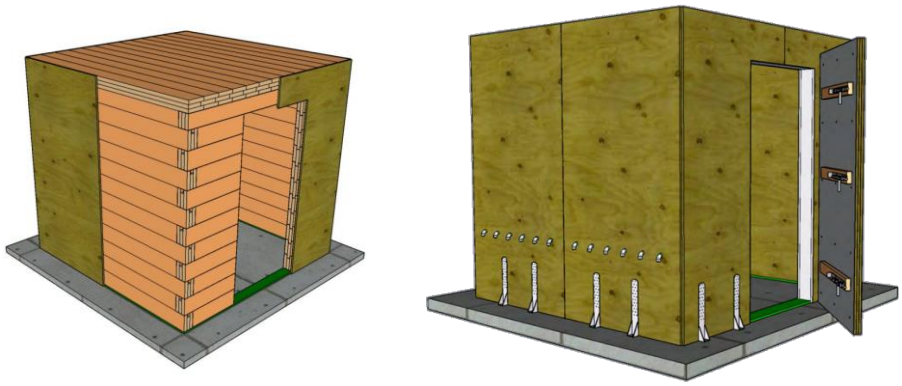

Figure 11: USDA/FPL dimension lumber shelter. Renderings of the interlocking beam system, plywood sheathing, door hinges and locks, concrete slab tie-downs, and air ducts included in the USDA/FPL shelter design (NAHB, 2019).

To understand the current market value of tornado shelters, a comparison of price versus occupancy is presented for the products discussed when cost data was available. Overall, steel shelter options are more costly than their concrete counterparts. The blue and orange markers, representing steel shelters, trend higher than the red markers, representing concrete shelters. The wood option is comparable or slightly lower than the concrete option but should be treated as more costly as the estimated price does not include installation and labor costs. Market value of a shelter also clearly increases when special features are included: comparing the three steel options that fit four people, Survive-a-Storm Shelters is the cheapest and also the most basic option, while Atlas Safe Rooms (which includes a special modular panel design) is more expensive and Vortex Vaults (the telescoping, multi-purpose shelter) is more expensive still.

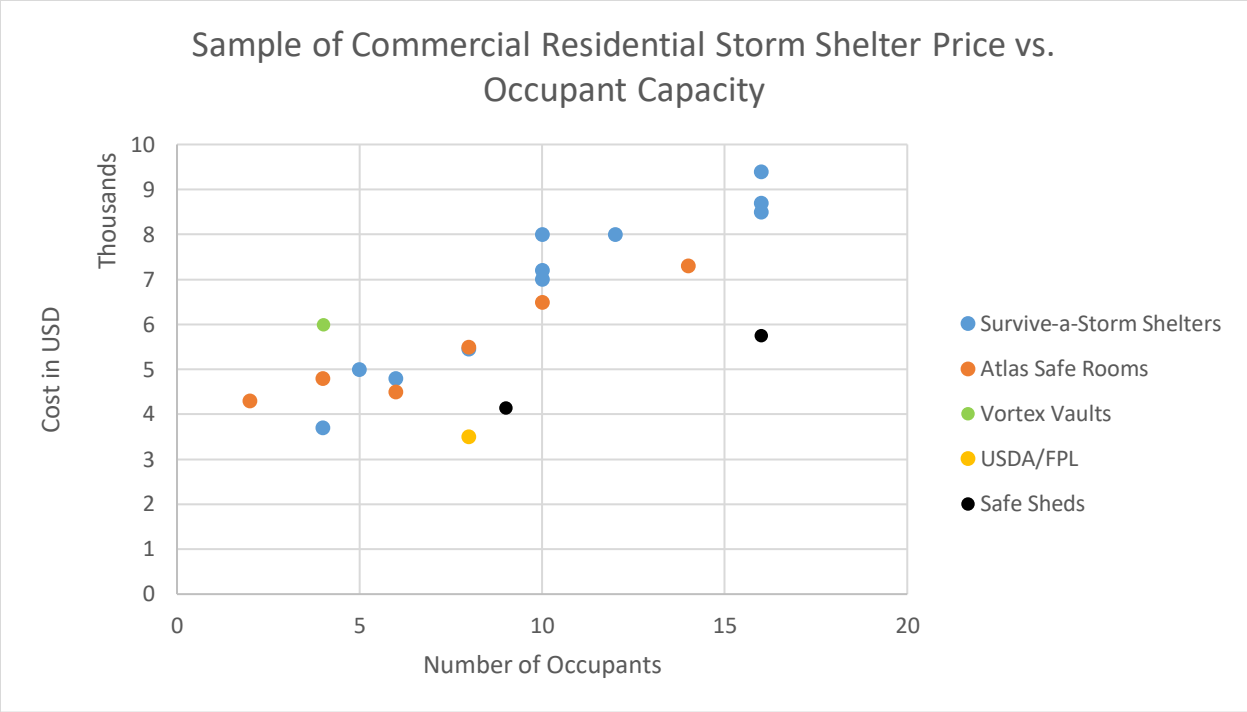

Figure 12: Price versus occupancy of tornado shelters. A graph comparing various commercially available tornado shelters, including steel, concrete, and wood options.

Besides existing products such as those reviewed above, there is current research focusing on new materials that may be useful in the tornado shelter industry. Cross-laminated-timber (CLT), for example, has been highlighted in several recent research projects as a potential tornado-shelter-friendly material. CLT was first introduced by a German PhD student named Gerhard Schickhofer in 1994 and has gained wider acceptance throughout Europe and North America in the following decades (Schickhofer, G., & Guggenberger, W., 1994 and Environment Analyst, 2018). In 2019, Falk et al. with the USDA and FPL tested CLT as an impact resistance material and Raymond with Clemson University designed a residential structure that was itself entirely tornado resistant (Falk et al., 2018 and Raymond, 2019). Although research on CLT structures as tornado shelters will be reviewed more in-depth in the literature review, it is briefly presented here to acknowledge that there is a desire for new debris-impact-resistant materials and

designs beyond currently marketed technology. As new engineering materials continue to be developed, the chance of designing a stronger, lighter, cheaper, easier-to-install, or more aesthetically pleasing shelter increases.

Ultra-High-Performance Concrete

When speaking of new engineering materials, ultra-high-performance concrete (UHPC) is a current and relevant example. The invention of UHPC is credited to Richard and Cheyrezy, a pair of French researchers that published a paper in 1995 on the "development of an ultra-high strength ductile concrete," which was "made possible by the application of a certain number of basic principles relating to the composition, mixing, and post-set heat curing of the concrete" (Richard & Cheyrezy, 1995). Their innovative curing process, along with the elimination of course aggregates and addition of steel fibers, was the inception of UHPC as it is used today and shall be reviewed more thoroughly in the literature review.

Ultra-high-performance concrete that includes fiber reinforcement is generally referred to as UHPFRC in current research. The high-density, self-compacting nature of UHPC and the addition of steel reinforcing fibers lead to fantastic mechanical properties, which are previewed here and discussed further in the literature review. UHPFRC is known to have superior compressive and tensile strength when compared to traditional concrete: compressive strength from the high density of cement and fine aggregate particles, and tensile strength from the continuous reinforcement provided by reinforcing fibers (Yoo & Banthia, 2017 and Riedel et al., 2010). UHPFRC also demonstrates high energy dissipation capabilities due to micro-crack spanning of the fibers, which makes it ideal for working with impact applications (Riedel et al.,

2010 and Beppu et al., 2020). Because tornado shelters must be able to resist mid-range impacts from wind-borne debris, UHPFRC is a promising material for a new tornado shelter design.

UHPC is currently used in a wide variety of ways throughout the world, and is gaining popularity for structural, architectural, and other more unconventional projects. One of the most common applications of UHPC to date are infrastructure projects. Azmee and Shafiq (2018) present an overview of several infrastructure projects, including the first prestressed UHPC hybrid pedestrian bridge built in Canada in 1997; nuclear cooling tower repair using UHPC to replace corroded beams in France in 2001; the 120 meter longest-span footbridge made of UHPC constructed in South Korea; and the first UHPC road bridge constructed in the United States in 2005 (Azmee and Shafiq, 2018). According to the Federal Highway Administration, there were 55 bridges built with UHPC in the United States and Canada as of 2013; as of 2019, there were 199 bridges in the United States and 97 bridges in Canada that incorporated UHPC in their design, showing rapid growth in the 16 years since the first UHPC bridge in the region was built (FHWA, 2019).

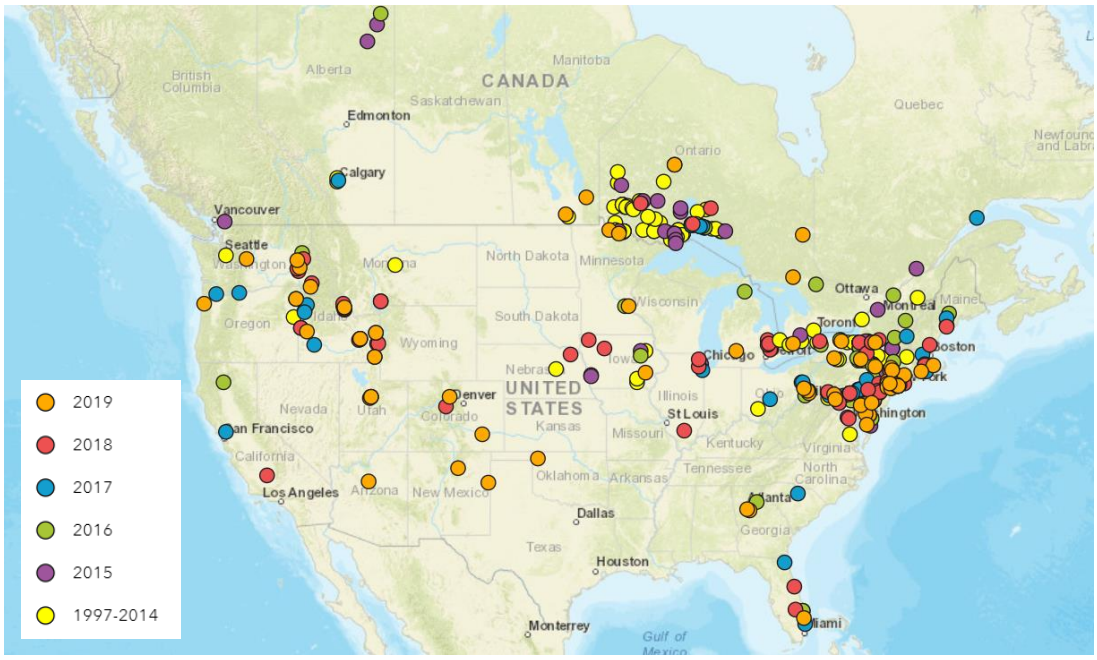

Figure 13: Map of UHPC bridges in the United States and Canada. Dots representing bridges are colored by year of completion (FHWA, 2019).

UHPC is also gaining more attention in building and architectural applications because of its ability to be cast into slender, unique shapes. Stunning examples can be seen in the slender exterior cladding of the Louis Vuitton Foundation, the "see-through" façade of the Museum of European and Mediterranean Civilizations, and the intricate roof structure of the Jean Bouin Stadium, all in France and pictured in **Figure 14** (Azmee and Shafiq, 2018). TAKTL, a company based in Pennsylvania, has developed a proprietary "architectural ultra-high-performance concrete" (AUHPC) to bring the use of UHPC in buildings to the residential and light commercial scale, as featured in **Figure 15**. TAKTL's AUHPC is marketed as having all the extraordinary structural properties of any other UHPC, but with a focus on aesthetically pleasing coloring and reduced chemicals for occupant safety (TAKTL, 2021).

Figure 14: Institutional-scale architectural applications of UHPC. From left to right, the Louis Vuitton Foundation, Museum of European and Mediterranean Civilizations, and Jean Bouin Stadium in France (Aguilar, 2014; Lomholt & Welch, 2021; and Architizer, 2014).

Figure 15: Residential and light commercial architectural applications of UHPC. Left, the Lululemon Flagship Store in Canada with swirling textures cast into the UHPC panels and right, the Consolidated Rental Car Facility at Kahului Airport in Hawaii with intricately cast window panels (TAKTL, 2021).

Finally, less conventional uses for UHPC are discovered often as the material increases in popularity and availability. Azmee and Shariq (2018) suggest the UHPC could be used in highly corrosive environments, such as over-sea bridges and energy producing windmills in oceans, because UHPC's high density make it highly resistant to chloride intrusion. Alternatively, structures in seismically prone areas could benefit from UHPC's high capacity for energy dissipation (Azmee and Shariq, 2018). On the less structural side, companies such as Nuance Studio in India and RTA Outdoor Living in Indiana are using UHPC to create the decorative wall panels and luxury outdoor grill sets shown in **Figure 16**, respectively (Nuance Studio, 2020 and

RTA, 2021). HHBC Consulting, based in Germany, is also utilizing UHPC to construct thin, lightweight bank vault doors to improve chemical and fire resistance (HHBC Consulting, n.d.).

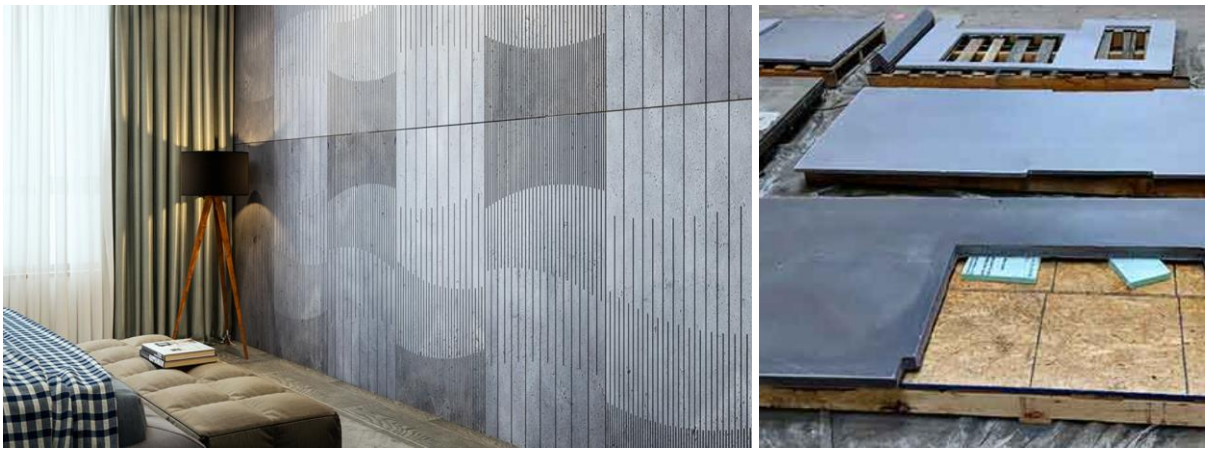

Figure 16: Decorative interior residential applications of UHPC. Left, a decorative UHPC wall and right, unfinished UHPC countertops (Nuance Studio, 2020 and RTA, 2021).

The demand for a material with high strength but small volume or thickness requirements has led companies and researchers to choose UHPC for innovative projects. Combining its incredible material properties, growing availability throughout the world, and unique fabrication options, it is easy to see why UHPC would be chosen for such a wide variety of applications as reviewed here. It is also clear that UHPC has the potential to be a game-changing material for tornado shelters if its strength and versatility can be appropriately applied.

Research Objectives

Ultra-high-performance concrete's engineering properties, versatile casting options, and unique aesthetic abilities make it an ideal material to study for potential tornado shelter designs. The goal of this research project is to evaluate UHPC's resistance to tornado-debris-like impacts and assess its future implementation in a tornado shelter.

Several objectives are proposed to support the research goal.

- Review existing knowledge of UHPC's performance under impact and other dynamic loading to design an appropriate test specimen.
- Utilize a full-scale debris cannon to accurately simulate the impact of high velocity 2x4s and analyze the response of UHPC panels via dynamic modeling, maximum deflection profiles, and controlling failure mechanisms.
- Evaluate the performance of UHPC panels when subjected to impact loads recommended by ICC/NSSA 500 and judged by their criteria of "passing" or "failing" as a tornado shelter.
- Propose design concepts for UHPC shelters to improve integration into homes, making the shelters more useable and therefore more likely to save lives.
- Discuss how UHPC compares to existing commercial tornado shelter options in terms of price, weight, and aesthetics.

LITERATURE REVIEW

This chapter provides a summary of experimental and analytical studies available in the research literature relevant to the objectives of this research.

Experimental Studies

Local damage to ultra-high-performance concrete structures caused by an impact of aircraft engine missiles (Riedel et al., 2010)

Riedel et al. (2010) extends an investigation of deformable aircraft engine missiles impacting reinforced concrete panels, published by Sugano et al. in 1993, by considering a similar experimental setup with ultra-high-performance fiber reinforced concrete (UHPFRC). Riedel et al. (2010) cites the development of UHPFRC technology in the 20-year gap between the two studies as well as UHPFRC's incredible capacity for energy dissipation as the motivation for the study. The researchers also point to the superior dynamic material properties of UHPFRC when compared to reinforced concrete (RC) applications as confirmation that repeating the experimental study by Sugano et al. (1993) with UHPRFC is justified.

As stated previously, Riedel et al. (2010) closely followed the experimental setup of Sugano et al. (1993), such that their UHPFRC results will be directly comparable to Sugano's RC results. Riedel et al. (2010) used a deformable steel missile with shape and dimensions shown in **Figure 17**, with weights and velocities shown in **Figure 19**. The UHPFRC panels are designed as approximately 1.02-inch thick, with other dimensions and rebar configuration shown

in **Figure 18**. Only flexural rebar reinforcement was included, as small amounts of shear reinforcement were shown to have no impact on the performance of the panels in previous research. Each panel is mixed with 1% steel fibers by volume, with the steel fibers having dimensions of 0.006 inches in diameter and 0.354 inches in length. Compressive strengths of each panel are also given in **Figure 19**, which varied from 25.0 ksi to 28.4 ksi.

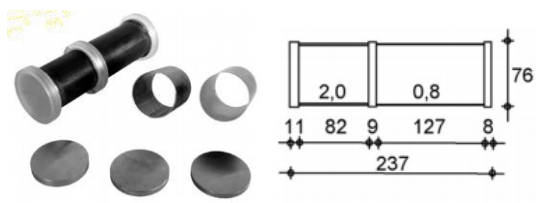

Figure 17: Deformable steel missile, assembled and segmented (Riedel et al., 2010). Missile dimensions shown in mm.

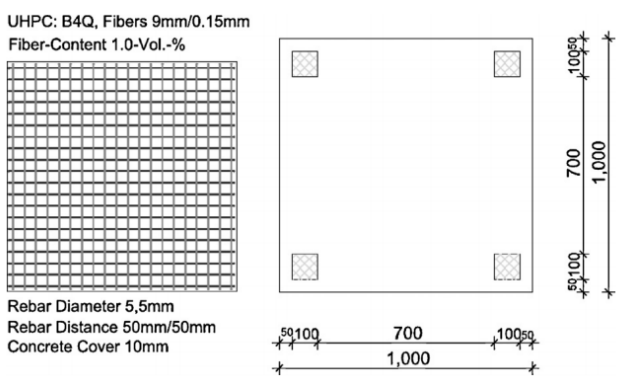

Figure 18: Geometry of UHPC panels and reinforcement (Riedel et al., 2010).

Experiment no.	Missile weight (g)	Impact velocity (m/s)	Compr. strength (MPa)	Young's mod. (MPa)	Reinforcement (cm^2/m)	Fiber content (vol.%)
1	1564	194.7	182.8	56,242	4.75	1.0
2	1569	258.7	172.1	55,577	4.75	1.0
3	1570	320.0	186.0	55,085	4.75	1.0
4	1570	332.0	174.5	54,922	4.75	1.0
5	1575	248.9	193.2	55,139	4.75	1.0
6	1575	368.6	196.0	54,579	4.75	1.0

Figure 19: Missile and panel details for experimental configuration (Riedel et al., 2010).

Riedel et al. (2010) accelerated their missiles using a gas gun. They measured the impact velocity with a laser senor at the exit of the gun barrel, the deformation of the panel with a combination of a high-speed camera and laser-interferometers, and any residual exit velocity with a second high-speed camera. The experimental setup is shown in **Figure 20**.

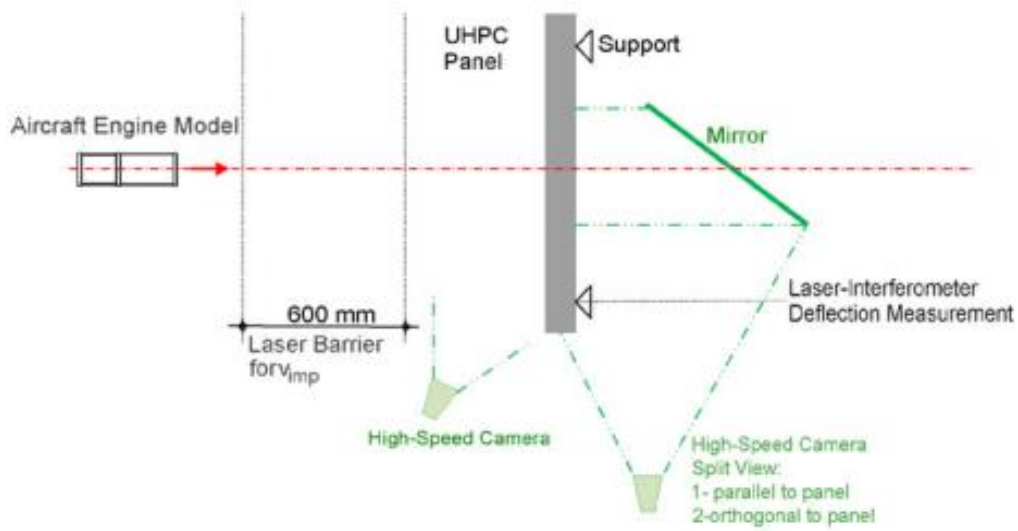

Figure 20: Experimental configuration (Riedel et al., 2010).

Failure modes of the UHPFRC panel considered in the study (from least damage to most damage) include penetration (C), just scabbing (JS), scabbing (S), just perforation (JP), and perforation (P). The failure modes are abbreviated as noted in the parentheses () and summarized in **Figure 21**; the trials with the lower damage designations correlate with panels that successfully rebounded the missile, while more serious failure modes correlate with panels that allowed the missile to pass completely through the specimen. The researchers also discuss the deformation of the steel missile, which is a significant source of energy absorption during the collision. The missiles deformed similarly to those in Sugano et al.'s research, suggesting that missiles in both experiments absorbed similar amounts of energy; therefore, the following

comparison of the energy absorption capacity RC panels from Sugano et al. (1993) and UHPFRC panels from Riedel et al. (2010) is appropriate.

Exp. no.	Impact velocity (m/s)	Residual velocity (m/s)	Mode	Front depth (mm)	Damage rear side			Deformation of missile	
					Width (mm)	Height (mm)	Remark	Mode	Length (mm)
1	194.7	−8.6 (rebound)	C	<0.2	220	220	Hairline cracks	Buckled	83
2	258.7	−7.3 (rebound)	JS	7–12	260	260	Hairline cracks	Buckled	56
3	320.0	0.0	JP	55	310	270	Concrete debris	Crushed	28
4	332.0	11.1	P	–	250	310	Perforation	Crushed	28
5	248.9	−9.42 (rebound)	JS	0.7	240	240	Hairline cracks	Buckled	58
6	368.6	16.1	P	–	280	290	Perforation	Crushed	28

Note. C: penetration mode, JS: just scabbing mode, S: scabbing mode, JP: just perforation mode, P: perforation mode.

Figure 21: Summary of test results (Riedel et al., 2010).

The UHPFRC panels showed significantly less front side damage when compared to RC panels in the penetration and just scabbing mode, leaving only a "footprint" mark on the front surface where the missile impacted the panel. This is due to the significantly higher compressive strength of UHPC, which exceeds the maximum stress induced on the panel during impact. For the just perforation and perforation modes, the damage in UHPFRC panels is very similar to RC panels as the missile goes completely through the panel. An example of improved front side performance is show in **Figure 22**.

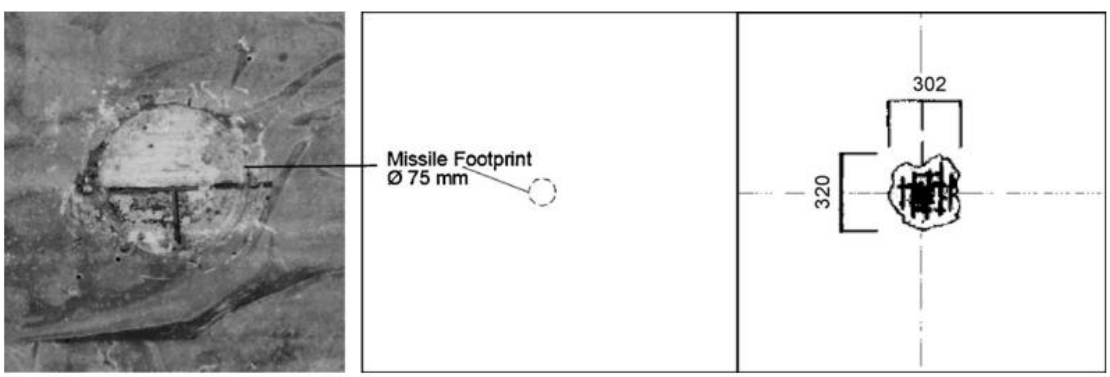

Figure 22: Comparison of UHPC and normal concrete #1 after impact (Riedel et al., 2010). Left and middle, damage of UHPC panel front side in experiment No. 1 (Riedel et al., 2010); right, damage of RC panel front side from Sugano et al. (1993).

Another significant improvement in UHPFRC panels is seen in the back-side damage of the panels, where the steel reinforcing fibers span cracks and suppress concrete debris from flying off the back of the panel. Improved back side performance is show in **Figure 23**. Riedel et al. (2010) attributed the success of the panels that failed by penetration and just scabbing modes to the fiber pull out mechanism that increases the UHPFRC's fracture energy by two orders of magnitude, demonstrated by a series of Hopkinson-Bar tests and illustrated in **Figure 24**. The researchers conclude that complete fiber pull out, and therefore the just perforation failure mode, occurs at an impact speed of 716 mph, which is much higher than conventional concrete's shear failure impact speed of 490 mph.

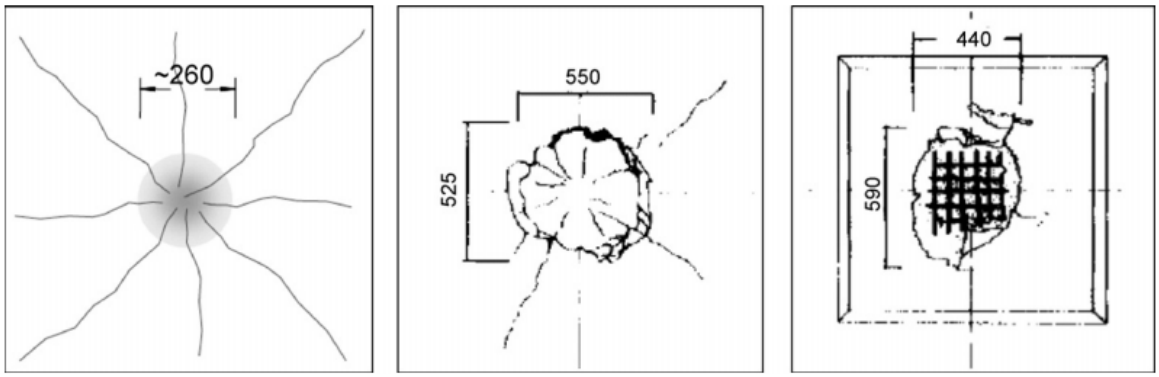

Figure 23: Comparison of UHPC and normal concrete #2 after impact (Riedel et al., 2010). Left, damage of UHPC panel rear side in experiment No. 2 (Riedel et al., 2010); middle and right, damage of RC panels rear sides in just scabbing and scabbing modes, respectively, from Sugano et al. (1993).

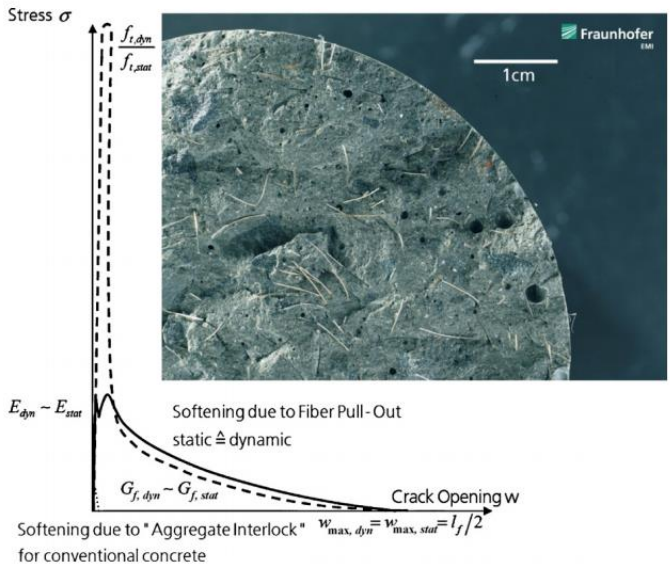

Figure 24: Stress versus crack opening width (Riedel et al., 2010). Stress-crack-opening function for UHPC under static (continuous line) and dynamic (dashed line) conditions, with magnified view of specimen after fiber pull out from Noldgen et al. (2009).

Riedel et al. (2010) makes a point to further discuss this "just perforation" failure mode at 716 mph impact velocity as the ballistic limit of the UHPFRC panel. Using a collection of equations formulated by Lambert and Jonas in 1976, the researchers predict a ballistic limit velocity of 717 mph. The experimental value of 716 mph confirms this prediction very accurately. Comparing conventional concrete's apparent ballistic velocity of 490 mph from the "just perforation" failure specimen from Sugano et al. (1993), Riedel et al. (2010) concluded that UHPFRC can absorb up to 110% more kinetic energy than similarly constructed panels of conventional concrete.

On low-energy impact response of ultra-high-performance concrete (UHPC) panels (Verma et al., 2016)

Verma et al. (2016) investigated the response of UHPC to low-velocity, low-energy impacts from a non-deformable drop weight. The researchers justify the scope of their paper by citing a plethora of high-velocity impact UHPC response studies, but a lack of studies on the arguably more common phenomena of low-velocity impact. To fully investigate contributing parameters, panels with varying fiber content, thickness, and impact energy were tested. Analytical models and a design flowchart based on the results are proposed.

Phase 1 of the research focused on mix design and material property testing. Three levels of fiber content were used: 0%, 2%, and 2.5% by volume of 0.512-inch long, 0.0063-inch diameter steel fibers. Results from unconfined uniaxial compression tests, split tensile strength tests, and 3-point-bending tests are shown in **Figure 25**. The results confirm the accepted theory that adding fibers significantly improves the tensile strength, energy dissipation capacity, and crack resistance of UHPC.

Mix	Compressive strength	Split tensile strength	Fracture energy
	MPa	MPa	N/*m*
R1	132.0	11.3	422
R2	170.3	22.6	14,323
R3	180.3	23.8	17,512

Figure 25: Mechanical properties of UHPC panels (Verma et al., 2016). Results for 0% (R1), 2% (R2), and 2.5% (R3) fibers by volume mixes.

Phase 2 focused on impact testing of the UHPC panels with every combination of fiber content, panel thickness, and impact energy. Experimental set up of the drop weight is shown in **Figure 26**, and results for a 11.9 lb missile are shown in **Figures 27** and **28**. Some of the key observations made by the researchers are that peak impact load increases with a greater panel

thickness because flexural stiffness of the panel increases; and that impact duration decreases with a greater panel thickness because impulse imparted during impact must be conserved as the peak force increases.

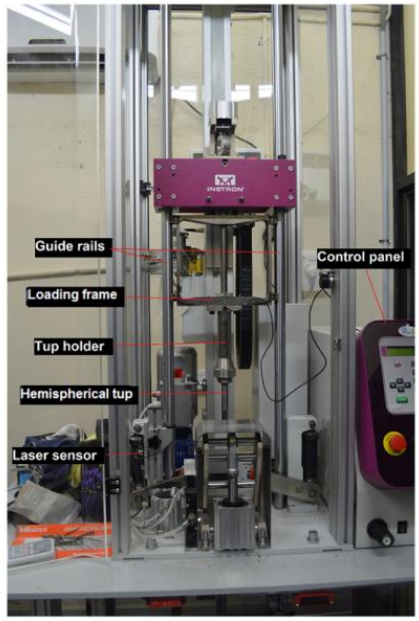

Fig. 2. Impact test setup.

Figure 26: Experimental setup of drop weight impact tests (Verma et al., 2016).

S.no	Thickness	Fiber	Energy	Impact velocity	Peak impact force
	mm	%	J	m/s	kN
1	10	0	10	1.92	4.40
2	10	0	15	2.35	5.15
3	10	2	10	1.92	4.26
4	10	2	15	2.35	5.79
5	10	2	20	2.71	6.39
6	10	2.5	10	1.92	3.95
7	10	2.5	15	2.35	5.12
8	10	2.5	20	2.71	3.47
9	15	0	10	1.92	5.94
10	15	0	15	2.35	6.67
11	15	2	10	1.92	6.64
12	15	2	15	2.35	8.23
13	15	2	20	2.71	10.40
14	15	2.5	10	1.92	7.08
15	15	2.5	15	2.35	8.86
16	15	2.5	20	2.71	9.27

Figure 27: Table of experimental results (Verma et al., 2016).

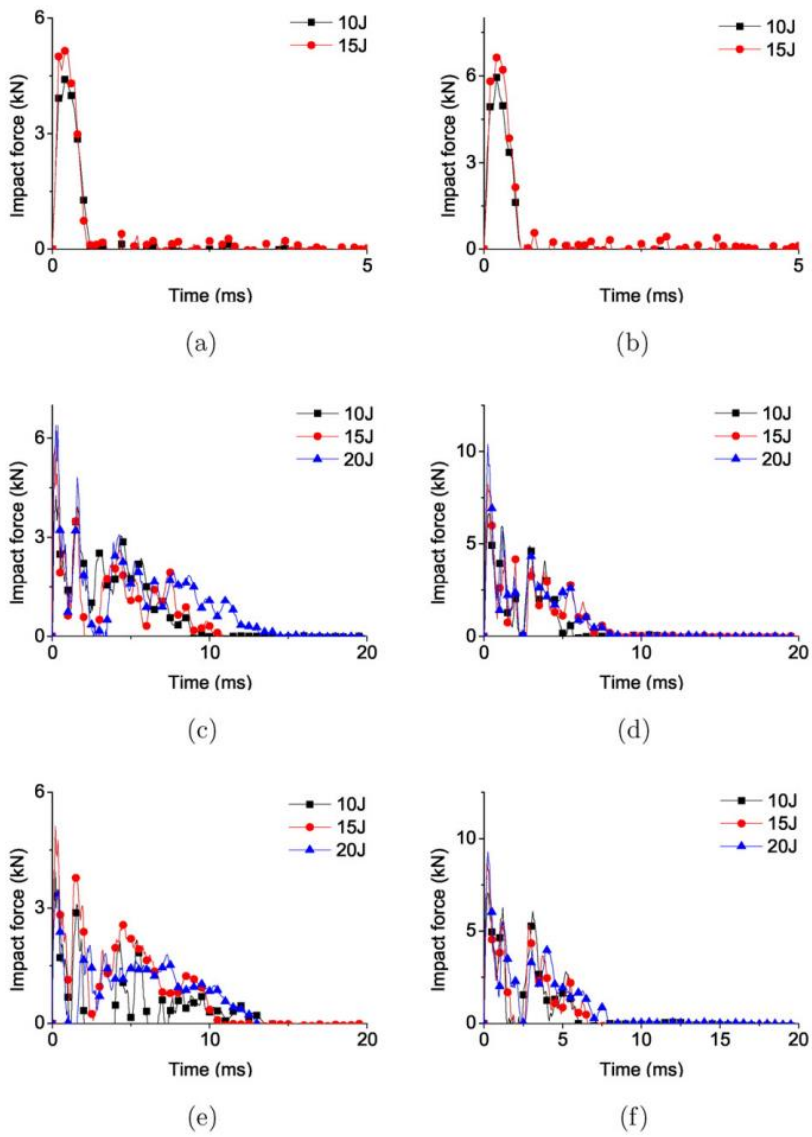

Figure 28: Impact-force-time history of UHPC panels (Verma et al., 2016). (a) 0.394-inch thickness and 0% fibers, (b) 0.591-inch thickness and 0% fibers, (c) 0.394-inch thickness and 2% fibers, (d) 0.591-inch thickness and 2% fibers, (e) 0.394-inch thickness and 2.5% fibers, (f) 0.591-inch thickness and 2.5% fibers.

Verma et al. (2016) also modeled the behavior of the UHPC panels using a finite element method. Simply supported boundary conditions were applied to the outside edges of the plate and the UHPC was assumed to fail by either tensile cracking or compressive crushing. The models show good fit for peak impact force and impact duration (R^2 values of 0.82 and 0.88,

respectively) and confirmed that an increase in panel stiffness increases peak force while decreasing impact duration. Maximum principal stress models, shown in **Figure 29**, predict that full panel cracking will occur when the strain values reach a minimum of 5.009 x 10^{-3} in/in throughout the height of the panel. **Figure 29** compares the model strain values with photos of the experimental specimens to show the resemblance between modeled and actual cracking patterns. The researchers also modeled the flow of energy throughout the impact, showing that initial kinetic energy of the impactor is mostly conserved as internal strain energy and viscous dissipation energy due to the change in shape of the UHPC panel. Based on the data shown in **Figure 30**, the case with the worst conservation was the 7.38 lbf-ft (10 J) case, with an energy loss of just less than 10%.

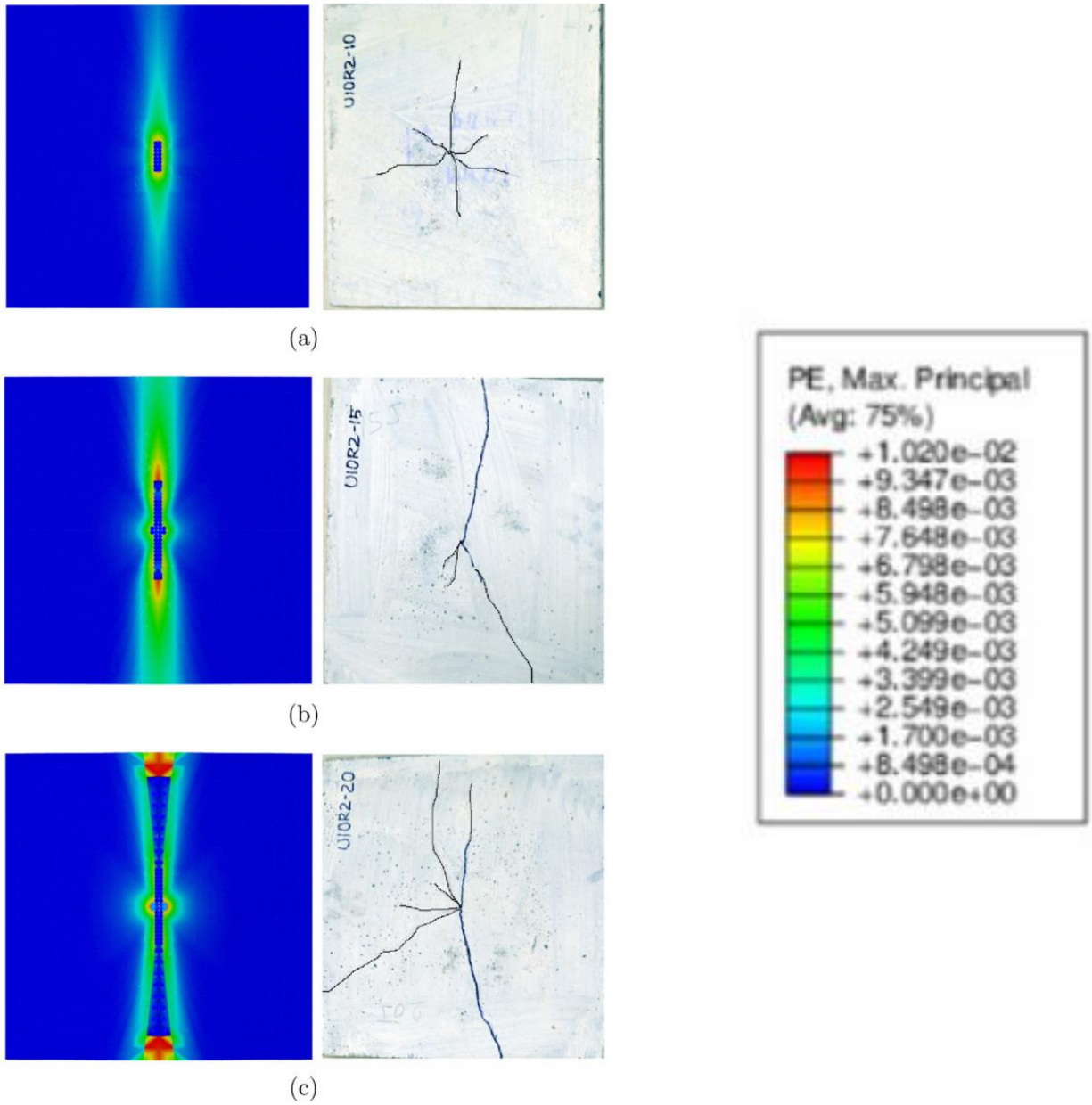

Figure 29: Comparison of strain model and experimental crack pattern (Verma et al., 2016). Images of maximum principal strain model with experimental crack pattern for 10 mm thick and 2% fiber panels – (a) 7.38 lbf-ft (10 J), (b) 11.1 lbf-ft (15 J), (c) 14.8 lbf-ft (20 J).

Time	KE	IE	VDE	KE + IE + VDE
ms	J	J	J	J
Impact energy = 10 J				
0	9.99	0.00	0.00	9.99
4	1.84	6.69	0.86	9.39
8	0.46	7.77	1.08	9.31
12	1.44	6.55	1.10	9.10
16	1.43	6.47	1.10	9.01
20	1.30	6.61	1.10	9.01
Impact energy = 15 J				
0	15.00	0.00	0.00	15.00
4	2.79	9.62	0.60	13.01
8	0.03	12.54	0.87	13.44
12	0.90	11.56	0.87	13.33
16	0.80	11.66	0.87	13.34
20	0.84	11.52	0.88	13.24
Impact energy = 20 J				
0	20.00	0.00	0.00	20.00
4	4.56	12.21	0.57	17.34
8	0.57	17.60	0.64	18.81
12	0.01	19.15	0.66	19.82
16	0.40	18.82	0.67	19.89
20	0.55	18.78	0.67	19.99

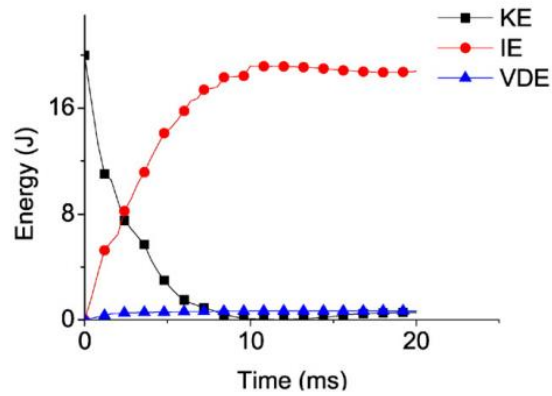

Figure 30: Energy balance of impact (Verma et al., 2016). Left, distribution of energy during impact; right, graphed data for 0.394-inch thickness, 2% fiber content, 14.8 lbf-ft (20 J) case.

To compare to their finite element model, the researchers also consider an analytical spring-mass model. A single degree of freedom (SDOF) system and a two degrees of freedom (TDOF) system are proposed: the SDOF system uses only the mass of the impactor and the bending stiffness of the panel; the TDOF system uses the masses of both the impactor and the panel as well as the panel bending stiffness and the contact stiffness during impact. The researchers concluded that there was little difference in the two models' abilities to predict peak force or impact duration. Verma et al. also concluded that while the models can accurately predict peak impact force, they do not capture the oscillations of force experienced in the experimental trials. The comparison for two trails is shown in **Figure 31**.

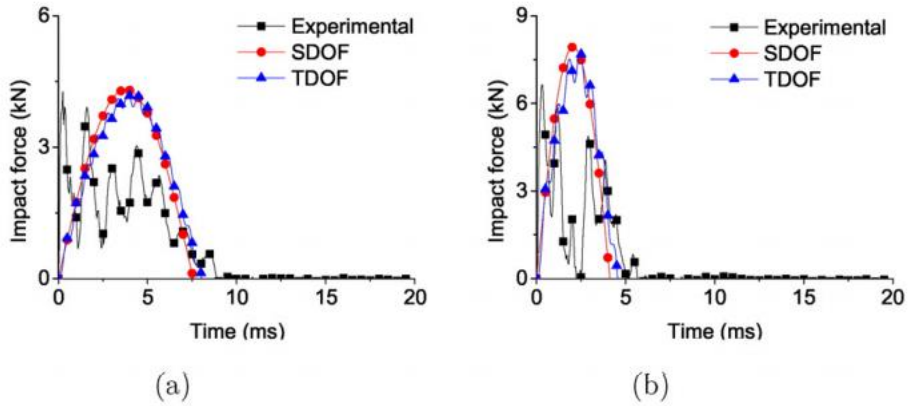

Figure 31: Experimental versus SDOF and TDOF force-time histories (Verma et al., 2016). Comparison of (a) 0.392-inch thick, 7.38 lbf-ft (10 J) panel and (b) 0.591-inch thick, 7.38 lbf-ft (10 J) panel.

Finally, Verma et al. analyzes the parameters that affect the UHPC's response and proposes as design procedure to choose an appropriate panel thickness. The parametric study suggests that increasing the impactor velocity will increase the peak impact load felt by the panel; increasing the panel thickness will increase bending stiffness and therefore increase the peak impact load felt by the panel; increasing the panel dimensions will decrease bending stiffness and therefore decrease the peak impact load felt by the panel; and increasing the amount of fibers will not change the peak impact load felt by the panel as the fibers do not engage until the panel is cracked, which happens after the peak impact load was observed. The proposed design flow chart is shown in **Figure 32**. The chart suggests using the analytical mass-spring model to predict the maximum load imparted by the impactor, then using the finite element model to predict the load capacity of the panel.

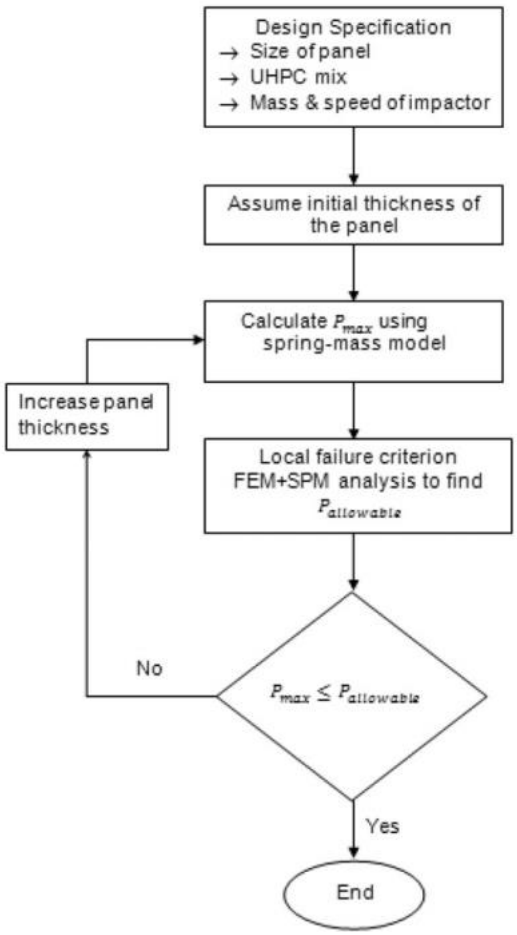

Figure 32: Flow chart for designing UHPC panels subject to impact load (Verma et al., 2016).

Mechanical and structural behaviors of ultra-high-performance fiber-reinforced concrete subjected to impact and blast (Yoo and Banthia, 2017)

Yoo and Banthia (2017) present a comprehensive review of current knowledge regarding the impact and blast resistance of ultra-high-performance fiber-reinforced concrete, citing the need to fully understand the effects of loading rate, fiber properties, fiber orientation, specimen size, and aggregate properties on the mechanical response of the UHPFRC. The superior strength and energy dissipation of UHPC is well documented.

Yoo and Banthia (2017) summarized several research studies that investigated different fiber shapes (straight, hooked, and twisted) under various loading rates (quasi-static, seismic, and impact). The compiled evidence suggests that twisted fibers improve energy dissipation at lower loading rates (quasi-static and seismic, less than 0.984 inch/s) because of their high bond strength; however, twisted fibers exhibit poor performance at higher loading rates as their shape decays quickly. Straight fibers are best for higher loading rates (impact, around 70.9 inch/s) as their pullout mechanism is non-destructive and does not depend on shape as with the twisted fibers.

Dynamic compressive strength is shown to increase with increasing fiber content up to 4% by volume. Alternatively, loading rate does not have a large effect on dynamic compressive strength for two reasons: the fibers bridge cracks, reducing the lateral cracks that appear as loading rate increases, and the high density of UHPC makes it less sensitive to high strain rates. In contrast, loading rate affects dynamic tensile and flexural behaviors significantly. At higher loading rates, cracks do not have time to find the weakest path through the material matrix, resulting in cracks through stronger aggregates and a higher material strength.

The effect of fiber type on dynamic tensile strength follows the same argument as the fiber pullout discussion above, with twisted fiber performing best under quasi-static loads and

straight fibers performing better under high-strain-rate impact loads. The length of the straight fibers can also determine the impact resistance of the specimen: Yoo and Banthia (2017) review several papers that conclude long fibers (1.18-inch long) are best for static flexural resistance, while a mixture of long and medium fibers (0.748-inch long) worked best for impact resistance as the varying lengths of fibers can engage different sized cracks. A mixture of fiber materials, such as steel and basalt, PVA, or PET has also been shown to increase impact and post-cracking strength, as the polymeric fibers are less likely to fail by slipping and fiber pullout. The polymeric fibers, however, rarely achieve their maximum pullout capacity because they fail in tension first. The development of higher tensile strength polyethylene fibers may make a hybrid fiber composition more beneficial in the future.

Increasing fiber content improved tensile behavior and impact resistance of UHPFRC, regardless of fiber type or strain rate. Data from several papers suggests that local response to projectile impact can be improved by adding up to 2% of fibers by volume, whereas global response is improved up to 6% of fibers by volume. Investigators noticed a plateau in local impact resistance at the 2% by volume threshold; however, the 6% by volume value does not necessarily correspond with the maximum possible increase in global performance, but was the largest percentage investigated in the study. Six percent of fibers by volume may indeed be the optimum level though, as Yoo and Banthia (2017) point out several drawbacks to higher fiber content such as low flowability, high porosity, and poor fiber disbursement. Thus, increasing the fiber content without bound is an unreasonable way to achieve higher strength, especially when the high cost of steel fibers is considered.

Fiber orientation's effect on dynamic tensile and flexural performance has not been widely studied; but an intuitive result has been obtained by some researchers whereby a "good"

fiber orientation, with fibers mostly oriented in the direction of tensile stress, outperforms an intentionally poured “bad” orientation, with fibers randomly aligned or mostly unaligned with the direction of tensile stress. As UHPFRC’s main draw for impact applications lies in its ability to improve tensile strength by bridging microcracks and increasing energy dissipation capacity, this result correlates with previous knowledge.

The effect of specimen size is well known for materials such as normal strength concrete and rock but is less obvious for UHPC specimens. Researchers that found a noticeable difference in strength when the size of the specimen was changed may have been observing the effect of varying fiber orientation properties: using the same placement methods does not guarantee similar fiber orientation when the specimen size is changed, as the flow rate of the UHPFRC changes and results in a different fiber disbursement. Further research confirmed that the size of the UHPFRC specimen does not affect the strength when similar fiber distribution is achieved among specimens, because UHPFRC’s dynamic strength depends mostly on its crack bridging matrices as opposed to the initial cracking strength characteristic of concrete and rock.

Yoo and Banthia (2017) compare four equations for predicting dynamic increase factors for tensile strength of UHPFRC: formulations from Fujikake (2006) and Park (2016) based on high-strain direct tension tests and Malvar (1998) and Mao (2014) formulations based on blast behavior. The authors suggest Fujikake (2006) and Park (2016) predict impact response reasonably well, but that they could improve the models with more precise data that control for inertial effects of larger specimens.

Development of a ready-to-assemble tornado shelter from cross-laminated timber (Falk et al., 2019)

Falk et al. (2019) propose a tornado shelter made of cross-laminated timber (CLT) as an alternative to traditional steel and concrete storm shelters. As the CLT industry becomes more established in North America, the researchers suggest that a viable CLT shelter design would save lives and increase market opportunities for CLT manufacturers. The shelter is designed with ICC/NSSA-500 standards in mind and consists of single-panel walls and roof; while convenient to assemble, the researchers concede that their design is best suited for residential applications that can accommodate lifting equipment as a single panel can weight over 1000 lb.

The study looks at two shelter dimensions: 8 ft by 8 ft plan with a height of 8 ft, and 5.5 ft by 5.5 ft plan with a height of 7.67 ft, which can serve nine and five people per FEMA guidelines, respectively. The assembled shelters are shown in **Figure 33**. Each shelter size was tested with 3-ply and 4-ply panels manufactured from V1 Douglas Fir. The panels were prefabricated and assembled on site using 4-inch by 4-inch 14-gauge sheet steel angles bolted to the CLT along each interior edge with 3/8-inch by 3-inch lag bolts. A CLT door was also included in the design, attached with 5/8-inch gate hinges and secured from the inside with three cane bolts. Finally, the foundation hold downs were 13-inch by 2-inch by ¼-inch A36 steel “L” shape bars bolted to the CLT panel and laboratory floor beams with 3/8-inch by 3-inch lag bolts. All the connection hardware can be seen in **Figure 34**.

Figure 33: 8 ft by 8 ft and 5.5 ft by 5.5 ft CLT shelters (Falk et al., 2019). Both include a CLT door.

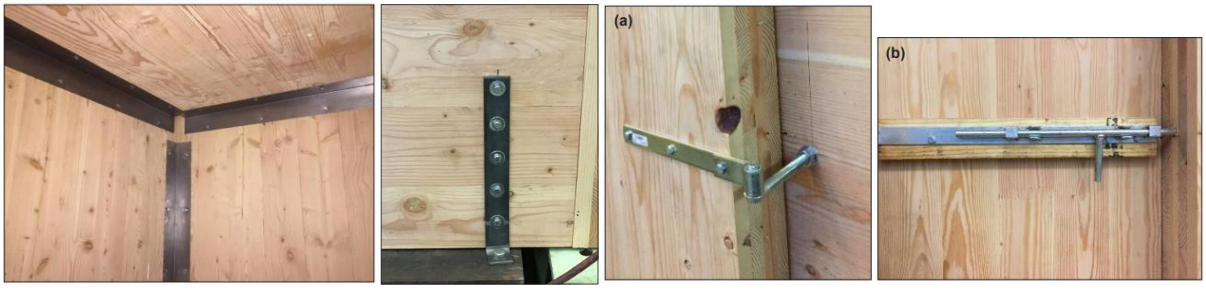

Figure 34: Assembly hardware (Falk et al., 2019). From left to right: 4-inch by 4-inch steel angles, 13-inch by 2-inch by ¼-inch foundation hold downs, cane bolts, and 5/8-inch gate hinges.

Falk et al. (2019) details the requirements for impact testing laid out in ICC/NSSA-500 Chapter 8. The researchers had trouble satisfying the length and weight requirement for the 2x4 missiles at the same time; therefore, they opted to prioritize the weight of the studs instead of the length of the studs, as length has no direct effect on the impact force imparted by the missile. The average length of the studs was therefore 12.75 ft (outside the 13.5 ft ± 0.5 ft ICC/NSSA-500 tolerance) and the average weight was 15.25 lb (within the 15 lb ± 0.25 lb ICC/NSSA-500

tolerance). The missiles were launched using a compressed air cannon, shown in **Figure 35**, and the velocity of the missiles was calculated using two photoelectric time gates spaced 12 inches apart in the muzzle of the cannon.

Figure 35: Debris impact cannon (Falk et al., 2019).

Shooting at 100 mph, the 3-ply wall panel failed for both the 5.5 ft by 5.5 ft and 8 ft by 8 ft shelters; however, the 3-ply door passed impact testing criteria. The 3-ply roof panels were tested at speeds in excess of the 67-mph requirement and passed the ICC/NSSA 500 testing criteria. Falk et al. (2019) concluded that a 3-ply CLT panel would be appropriate for a door or roof component but is not strong enough for a wall component. The 4-ply panels were tested with a 5.5 ft by 5.5 ft shelter, an 8 ft by 8 ft shelter, and a door. All three successfully resisted the missile impacts at speeds greater than 100 mph, leading the researchers to conclude that a 4-ply

CLT panel could be used for any shelter component. Examples of damage to 3-ply and 4-ply panels can be seen in **Figures 36** and **37**.

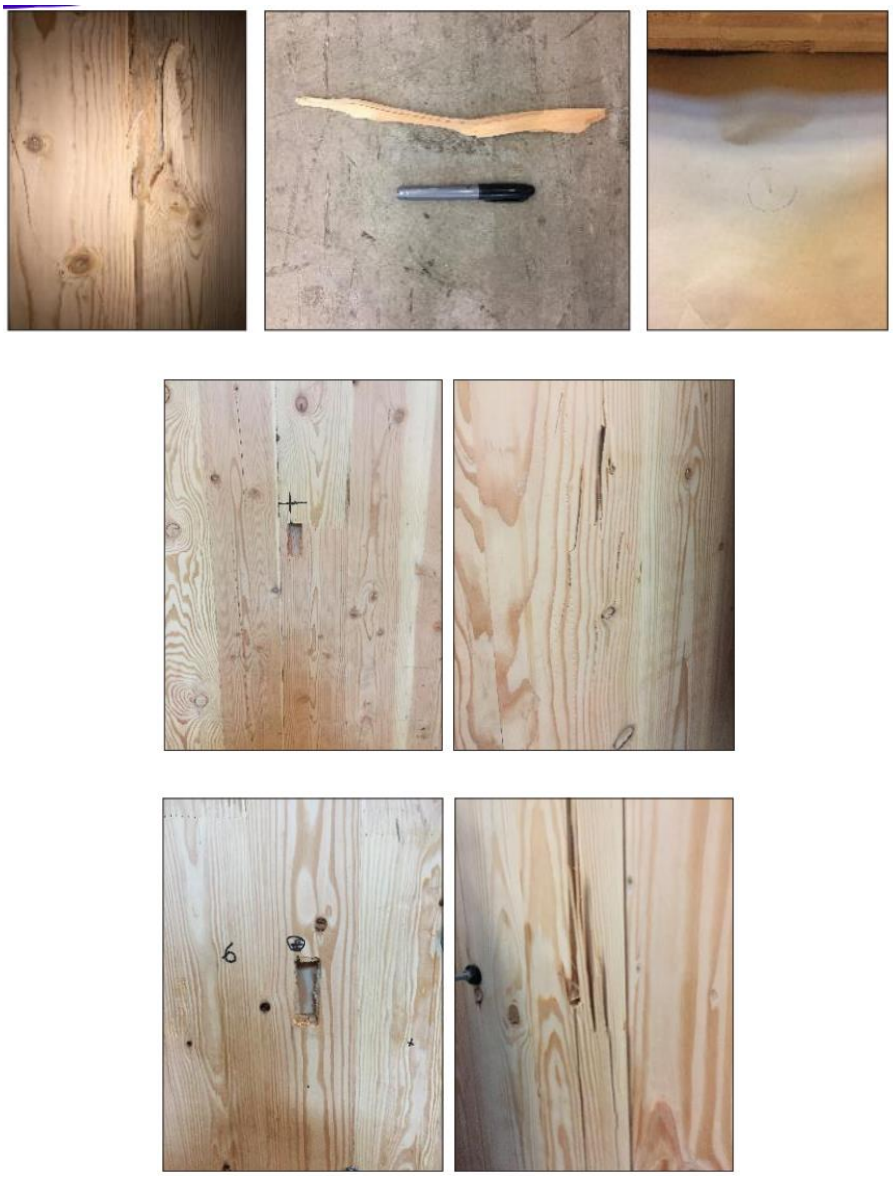

Figure 36: 3-ply CLT results (Falk et al., 2019). First row, interior damage to 3-ply wall panel, debris ejected from back of panel, and perforation of witness screen at 107 mph (Fail). Second row, exterior penetration and slight interior cracking of 3-ply roof panel at 86 mph (Pass). Bottom row, exterior penetration and slight interior cracking of 3-ply door at 103 mph (Pass).

Figure 37: 4-ply CLT results (Falk et al., 2019). Top row, exterior penetration of 4-ply wall panel in 8 ft by 8 ft shelter at 110 mph (Pass). Bottom left, exterior penetration of 4-ply wall panel in 5.5 ft by 5.5 ft shelter at 102 mph (Pass). Bottom right, multiple exterior penetrations with no interior damage of 4-ply door at 103 mph (Pass).

The other aspect of the research focused on pressure testing to simulate wind loads from tornadic events. The study states the 250-mph basic wind speed required by ICC/NSSA-500 and calculated according to the ASCE 7-10 Main Wind Force Resistance System (MWFRS) method. For their 8 ft by 8 ft shelter, the lateral pressure is 167 psf and the suction (uplift) pressure is 224

psf. To test the CLT panels for wind load, Falk et al. (2019) considered three different applications of the load. The first tested the strength of the panels themselves using a pressurized airbag sandwiched between the panel and the floor. The second setup tested the lateral shear load on the entire structure by installing the airbag between the shelter wall and a reinforced concrete strong wall in the laboratory. Finally, the third setup tested the uplift resistance of the entire shelter using a steel actuator to push up on the inside of the shelter. All three experimental setups are shown in **Figure 38**.

Figure 38: Wind pressure testing setup (Falk et al., 2019). From left to right: panel pressure test setup, lateral shear load test setup, and uplift force test setup.

The 3-ply panel successfully resisted a load of 300 psf, or 1.8 times the design load of 167 psf. The researchers therefore did not test a 4-ply panel, as the 3-ply panel was adequate. The entire 8 ft by 8 ft shelter and its foundation tie downs resisted 395 psf, or 2.3 times the design load, of lateral shear load from the second test. When loaded on the wall opposite the door opening, a maximum deflection of 1.0 inch was recorded. When loaded on a wall adjacent to the door opening, a maximum deflection of 1.5 inches was recorded for the same load. Entire shelter deflections were greater and slightly unsymmetric when the airbag was applied on a wall panel adjacent to the door opening as opposed to opposite the opening, leading to the conclusion

that the stiffness of the panel with the door cut out was significantly impacted by that loss of material. Deflections from each case are shown in **Figure 39**. Finally, the uplift tests recorded a maximum deflection of 1.38 inches and a permanent deflection of 0.54 inches from 14,300 lb, or 1.0 times design load, of uplift force. A second test on the same panel recorded a maximum deflection of 2.19 inches and a permanent deflection of 1.22 inches after reaching 21,500 lb, or 1.5 times design load. The values from the second test include the permanent deflection from the first test, and both displacement graphs are show in in **Figure 39**.

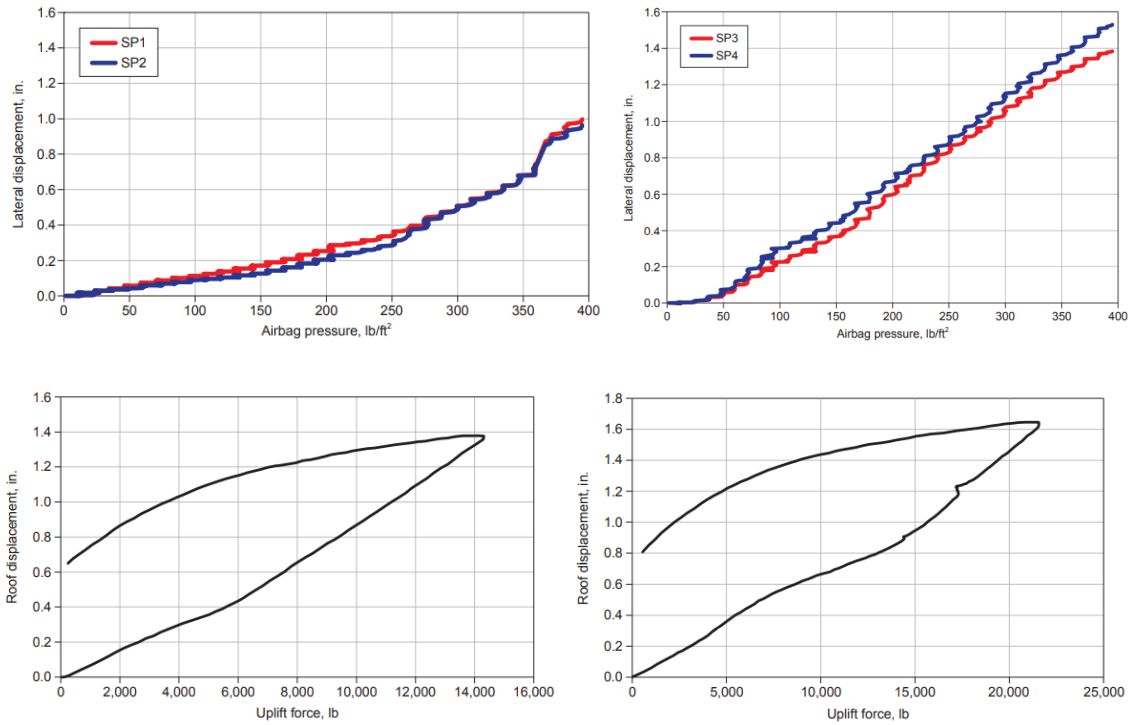

Figure 39: Displacements from wind pressure and uplift testing (Falk et al., 2019). Top left, displacement of shelter when loaded laterally on wall opposite door opening; top right, displacement of shelter when loaded laterally on wall adjacent to opening. Bottom left, displacement of roof panel during first uplift test; bottom right, displacement of panel during second uplift test.

Falk et al. (2019) concluded that tornado shelters constructed from CLT panels are a viable alternative for future use, as the shelters met or exceeded the ICC/NSSA-500 and ASCE7-

10 specifications for impact and wind loads. The study suggests that further research is needed for shelters that are fabricated from multiple panels or contain joints or splices, as they may perform differently than the full-size panels tested here.

Failure characteristics of UHPFRC panels subjected to projectile impact (Beppu et al. 2020)

Beppu et al. (2020) investigates projectile impact loading on Ultra-High-Performance Fiber-Reinforced concrete (UHPFRC) panels, specifically focusing on pre-stressed panels subject to mid-range projectile speeds of 112 to 336 mph. The researchers justify the decision to prestress the panels by citing the improved performance of pre-stressed UHPFRC panels under static loads. The researchers also justify their study by presenting previous studies on UHPFRC as a highly impact-resistant material when subjected to high-speed, low mass projectiles (1570 mph, 0.0176 lb); when subjected to low-speed, high mass projectiles (22.4 mph, 1050 lb); and citing a lack of data on mid-speed, medium mass projectiles. Beppu et al. (2020) suggested that these mid-speed, medium mass projectiles could originate from tornados, volcanic eruptions, or other similar wind-storm events.

The experimental design included three different panel thicknesses: all panels were 45.3-inch wide and 45.3-inch tall, with thicknesses of 2.36 inches, 3.54 inches, and 4.72 inches. All panels include 0.5-inch pre-stressing wires spaced at 3.54 inches in both directions throughout the panel, and pre-stressed to 176 kips, as shown in **Figure 40**. Steel reinforcing fibers of 406 ksi tensile strength, 0.00787-inch diameter, and 0.591-inch length are mixed at 2% by volume into the UHPC which has an average compressive strength of 31.3 ksi and an average tensile strength of 1.78 ksi after heat curing. For each panel thickness, a specimen was tested with either no pre-stressing steel reinforcement; pre-stressing steel reinforcement without induced pre-stress; or pre-stressing steel with induced pre-stress. All panels included steel fiber reinforcement.

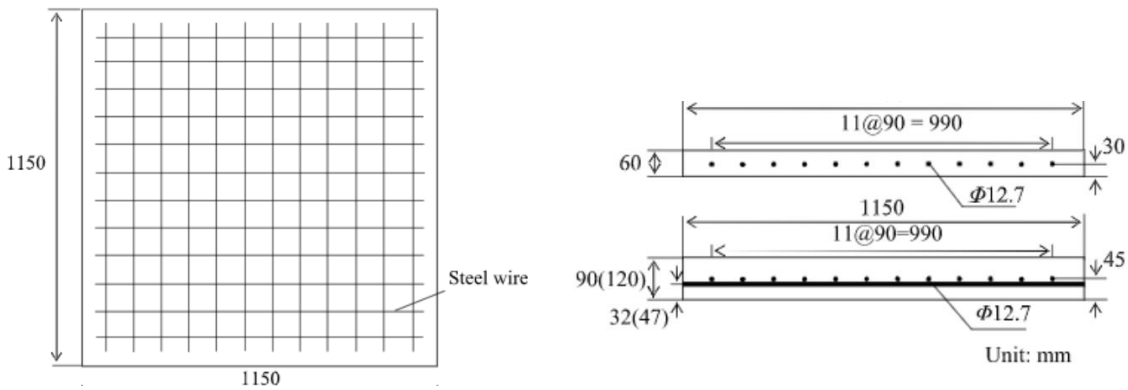

Figure 40: Specimen dimensions (Beppu et al. 2020).

The test setup used a projectile launching machine with a laser velocity sensor, shown in **Figure 41**, to accelerate an 18.3 lb steel nosed projectile at the center of each panel. The target speed for each test was 94.0 mph. Load cells fixed between the panel and the reaction frame measure the reaction force, while strain gauges placed on the back of the panel measure the displacement history of the panel, as shown in **Figure 41**. A high-speed camera recording the event allowed the researchers to create a displacement-time history later used to estimate the initial impact force of the projectile.

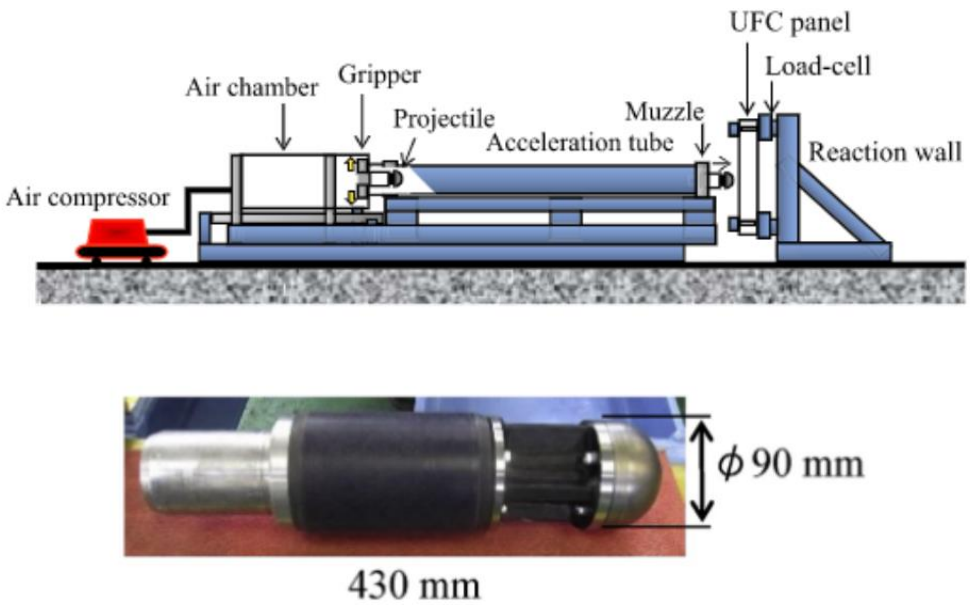

Figure 41: Launching test machine and steel projectile (Beppu et al. 2020).

Failure modes considered in this study (from least damage to most damage) include spalling, scabbing limit, scabbing, and scabbing with a hole. The thinnest panels, with thickness of 2.36 inches, all failed by scabbing with a hole, as shown in **Figure 42**. The failure mode of the 2.36-inch panels was not affected by the presence of steel reinforcement or pre-stressing; all 2.36-inch panels exhibited similar front face spalling, back face scabbing, and back face hole diameters. Beppu et al. (2020) therefore suggests that the failure is due to shear stress, as no shear reinforcement was included in any panel and would cause all 2.36-inch panels to fail in the same manner.

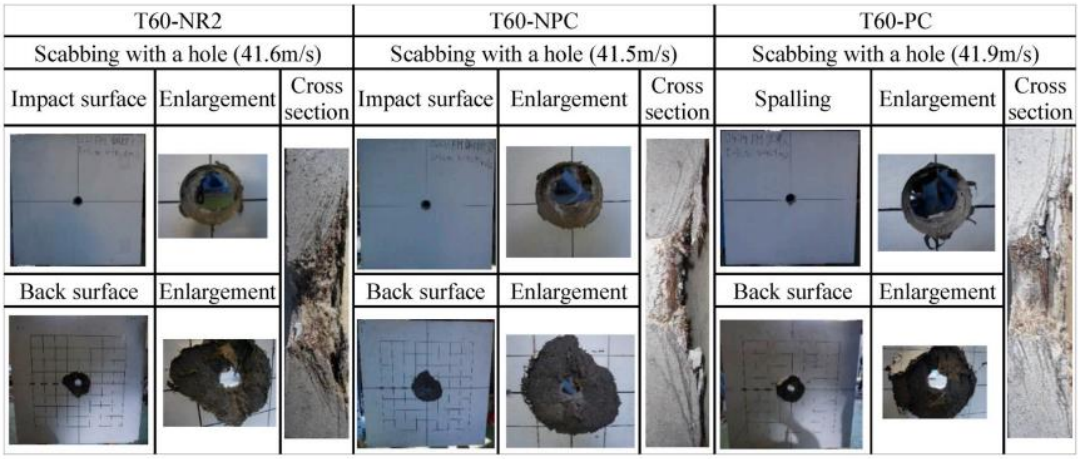

Figure 42: Failure state of 60 mm (2.36 inch) UHPFRC panels (Beppu et al. 2020).

The 3.54-inch panels all failed by scabbing, with one of the unreinforced panels failing at the scabbing limit. Photos of the failed specimens are shown in **Figure 43**. The researchers explained that approximately 94.0 mph is therefore the scabbing limit velocity of the unreinforced 3.54-inch panels. However, the reinforced 3.54-inch panels showed nearly 35% smaller scabbing diameters compared to the unreinforced panels. They suggest that the presence of the steel wires better confined the UHPC panel and therefore better resisted the projectile impact, although pre-stressing had little effect on the scabbing diameter of the reinforced 3.54-inch panels.

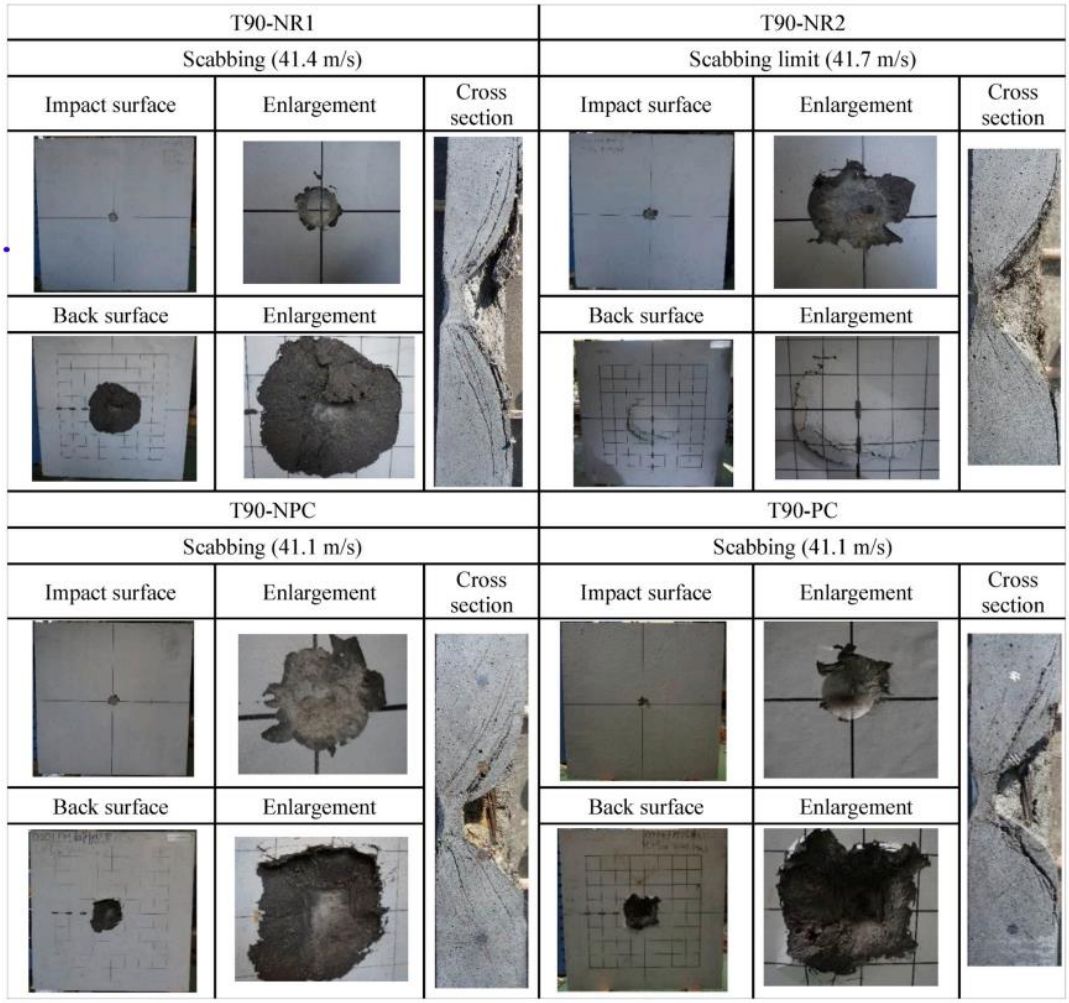

Figure 43: Failure state of 90 mm (3.54 inch) UHPFRC panels (Beppu et al. 2020).

Finally, the 4.72-inch panels failed by spalling, as seen in **Figure 44**, with few cracks showing on the back of the panels. Similar conclusions are drawn about the 4.72-inch panels as the 3.54-inch panels: the confining effect of the steel reinforcement helped deter flexural failure and back face scabbing, while the pre-stress in the strands did not significantly change the failure mode of the panel.

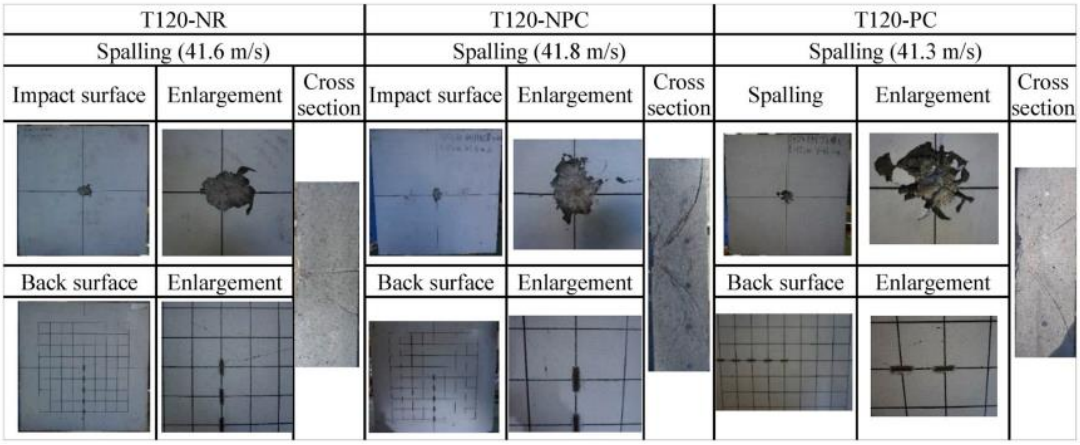

Figure 44: Failure state of 120 mm (4.72 inch) UHPFRC panels (Beppu et al. 2020).

Beppu at al. (2020) concluded that conservation of momentum was upheld by comparing the initial momentum of the projectile with the area under a time-force curve captured by the load cells. By comparing the displacement-force curve with the initial kinetic energy of the projectile, it was shown that kinetic energy was also mostly conserved; the researchers suggest that local deformation was responsible for absorbing most of the energy. **Figure 45** charts the change in these values throughout the course of the impact for one of the 3.54-inch panels. Similar analysis was done for all other panels as well.

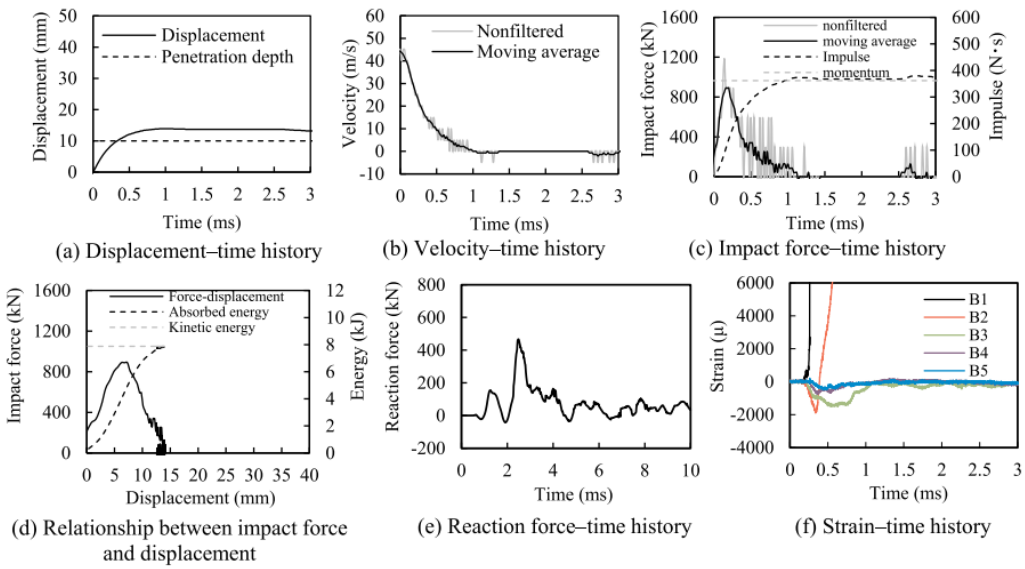

Figure 45: Measured data from 90 mm panels (Beppu et al. 2020).

To predict scabbing and perforation limits, Beppu at al. (2020) compared the Chang and Degen (1981) formulae to the CRIEPI (NEI, 2011) formulae, concluding that the former better predict UHPFRC response while the latter better predict RC response. However, CRIEPI can be modified to improve its predictions of UHPFRC by adjusting the reduction coefficients. It is noted that the perforation limit thickness of UHPFRC is approximately 20% lower than RC panels, while the scabbing limit thickness is approximately 40% lower. Additionally, Beppu at al. (2020) considered formulae to predict a critical impact energy as a function of the panel thickness, which is based on the modified CRIEPI equations. The formulae agree well with the experimental results and predict a 400% increase in absorption capacity between RC panels and UHPFRC panels.

Numerical and Analytical Models

Response of ultra-high-performance fiber reinforced concrete (UHPFRC) to impact and static loading (Habel and Gauvreau, 2008)

Habel and Gauvreau (2008) investigated the experimental response of UHPFRC under static and high strain rate (impact) loading to validate a proposed two mass-spring dynamic response model. UHPFRC has been shown to have higher strength gain under higher strain rates without reducing maximum strain capacity; reduced spalling and scabbing under impact loads; and high energy dissipation capacities due to fiber bridging across the matrix. These characteristics make UHPFRC an ideal candidate for further impact study. The researchers also argue that a two mass-spring model, although less refined as a detailed finite element analysis, will be appropriate if nonlinear behavior for the springs is included in the model.

The specimens for static and impact bending tests were 23.6 inches long, 5.71 inches wide, and 1.97 inches deep. The UHPFRC mix had an average compressive strength of 19.2 ksi at the time of testing. Three- and four-point bending tests were conducted to analyze the static response, with an associated strain rate of 5.7×10^{-6} in/in s^{-1} and an experimental set up shown in **Figure 46**. Drop weights tests were performed on the panels to assess response to high strain rates. Impactors with weights of 22.7 lb at 9.40 mph and 45.4 lb at 9.62 mph were used. **Figure 47** shows the experimental set up, including instrumentation to measure impact force, reaction force, and panel deflections.

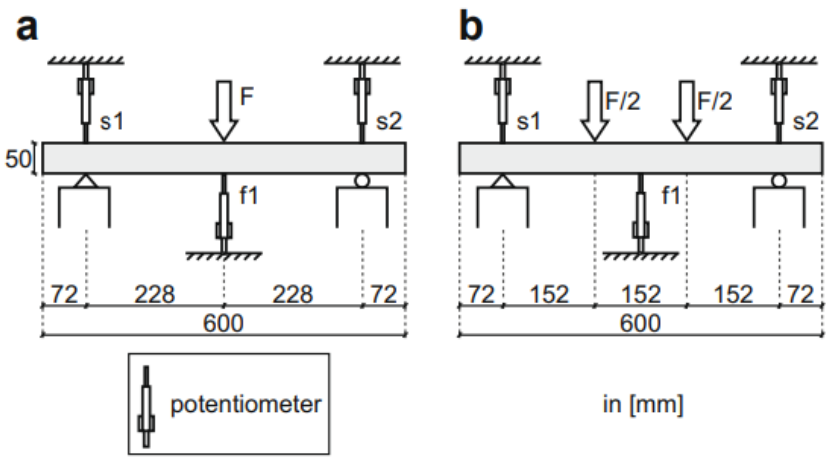

Figure 46: Three- and four-point bending test setups (Habel and Gauvreau, 2008).

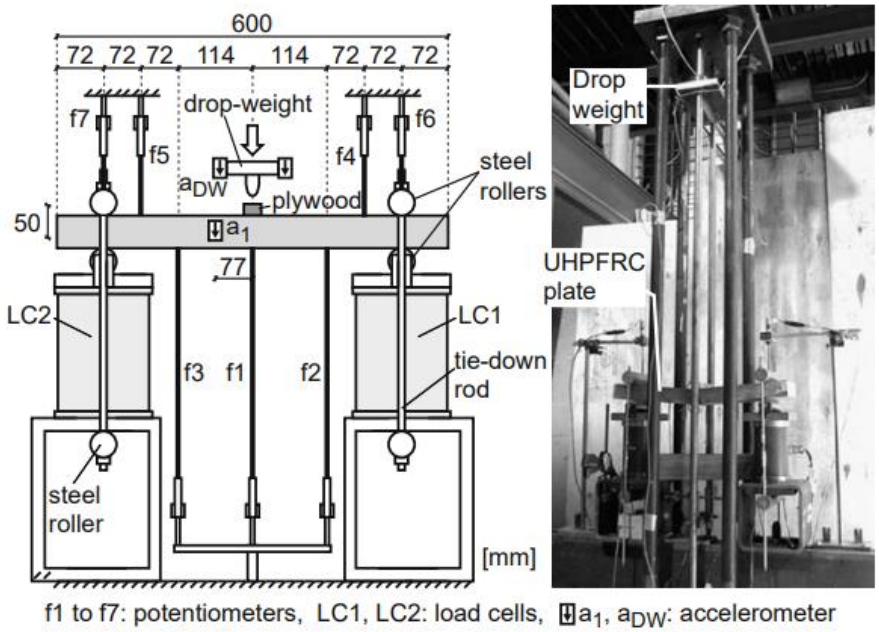

Figure 47: Drop weight test setup (Habel and Gauvreau, 2008).

To model the static response, a cross-section-based model was used to determine the moment-curvature relationship of the panels. The parameters of the assumed behavior are shown in **Figure 48**. The two mass-spring model, shown in **Figure 49**, considers nonlinear springs that yield two classic equations of motion. The term $R_P(u_P)$ describes the static response of the plate

under equivalent static loading, while the term $R_D(u_{DW}-u_P)$ describes the resistance of the plywood placed between the drop weight and the UHPFRC panel.

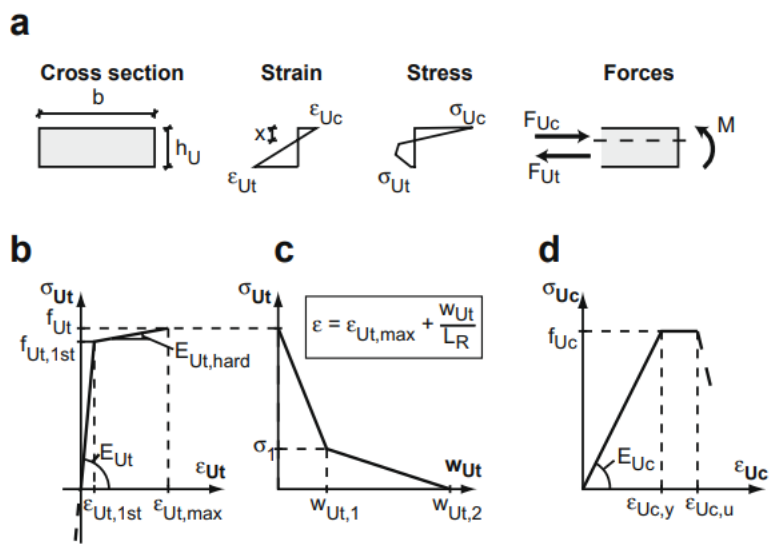

Figure 48: Definition of model parameters (Habel and Gauvreau, 2008). (a) Stress distribution through cross section; (b) linear-elastic and strain hardening behavior in tension; (c) softening behavior in tension; and (d) compressive behavior.

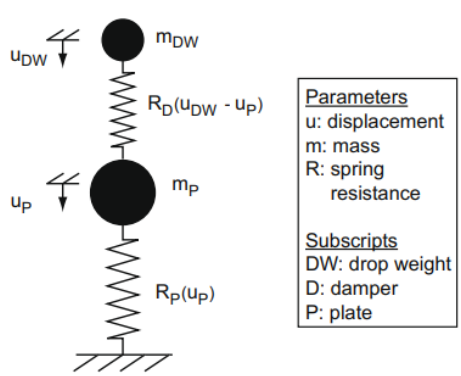

$$m_{DW} \cdot \left(\frac{d^2 u_{DW}}{dt^2} - \frac{d^2 u_p}{dt^2} \right) + R_D(u_{DW} - u_p) = 0$$

$$m_p \cdot \frac{d^2 u_p}{dt^2} + R_p(u_p) - R_D(u_{DW} - u_p) = 0$$

Figure 49: Mass-spring model and equations of motion (Habel and Gauvreau, 2008). Two mass-spring model with nonlinear springs and associated equations of motion.

Results from the three- and four-point static bending tests are shown in **Figure 50**, including experimental and calculated curves. Although the data has a high scatter, explained by

the researchers as due to inconsistent mixing and pouring methods, the average experimental curve and the cross-section-based analytical curve show a good agreement.

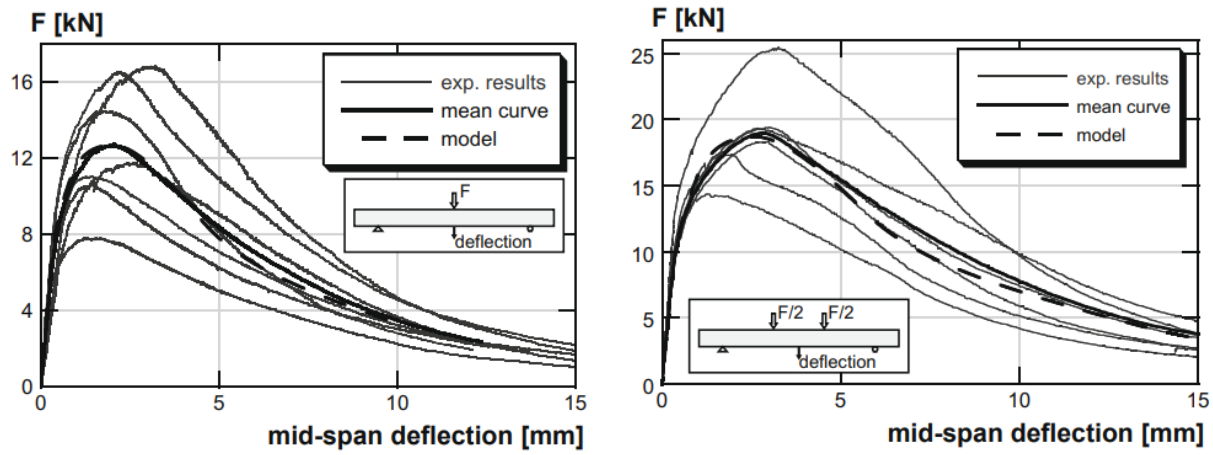

Figure 50: Results of three- and four-point bending tests (Habel and Gauvreau, 2008). Left, results of three-point-bending tests; right, results of four-point-bending tests. Drop weight tests showed a maximum strain rate of approximately 2 in/in s^{-1}.

Panel failure was attributed to cracks on the lower surface, which are typical for strain hardening materials, with final fracture of the panel occurring after fiber pullout. The specimens failed in bending, similarly to the static bending tests. Time evolution of deflected shape and strains in one of the test specimens are shown in **Figure 51**. The peak impact force of 5,260 lb occurred at approximately 1.6 ms, corresponding to the downward facing white triangle markers. The deflection and maximum strain rates clearly lag the peak impact force as they continue to grow until 3.33 ms after impact. The researchers observe that the deflected panel maintains an elastic shape until 2.08 ms (black circle markers), after which the sharper shape at midspan indicates inelastic behavior due to strain hardening and cracking.

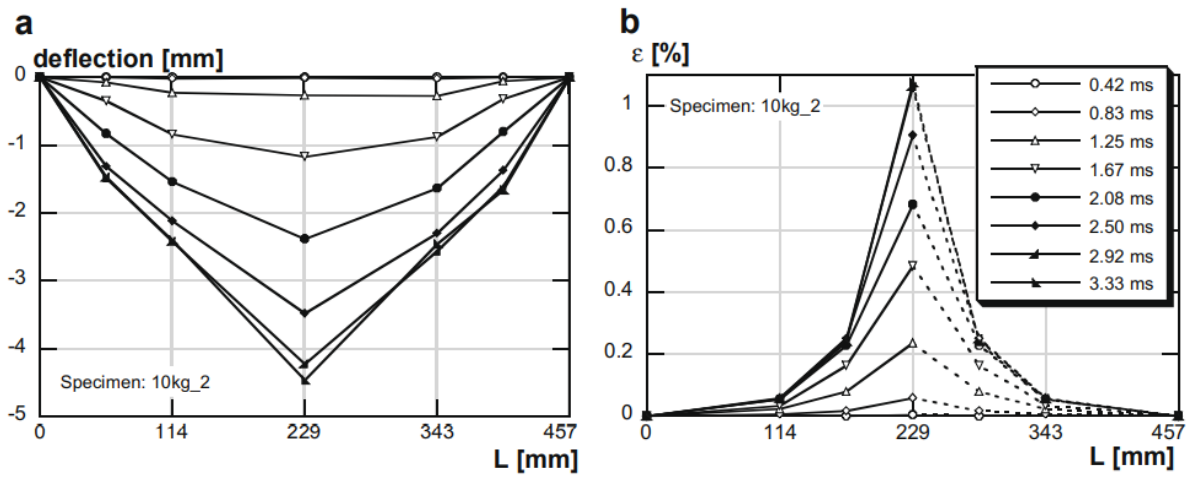

Figure 51: Time evolution of deflected shape and strain (Habel and Gauvreau, 2008). Measurements taken at bottom midspan of specimen.

When building the analytical models, the researchers began by defining an equivalent panel mass and the nonlinear spring values. An equivalent mass of 40% of the panel's weight was used in the models because it corresponded to a linear-elastic response with a hinge at midspan representing the ultimate inelastic failure. R_P, the spring force representing the panel's equivalent static response, was defined using the drop weight force and panel deflection histories. R_D, the spring force representing the plywood's response, was determined from a set of static bending tests on plywood samples multiplied by 1.3 to account for dynamic loading as suggested by Bischoff et al. (1990). Using the experimental drop weight force as R_D and midspan deflection as u_P, the model could successfully predict impact duration, peak impact force, shape of the force-time response, and number of impacts until failure. Comparison of the experimental data and modeled curves are shown in **Figure 52**.

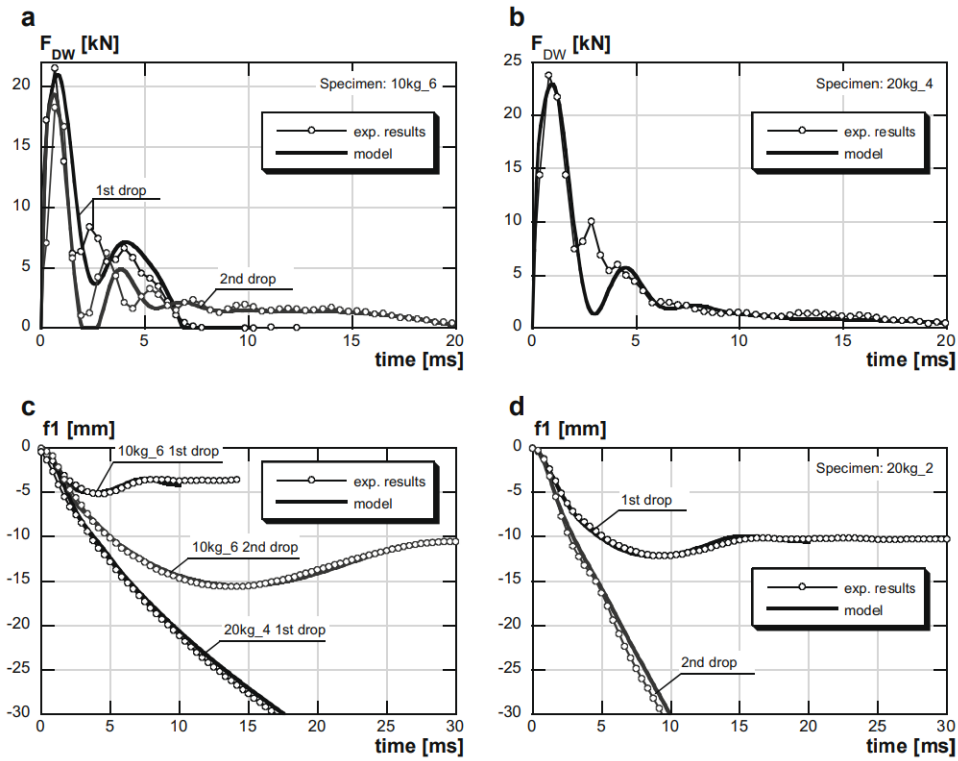

Figure 52: Model versus experimental results (Habel and Gauvreau, 2008). Results shown for (a/b) impact force vs. time and (c/d) midspan deflection vs. time.

Habel and Gauvreau (2008) conclude that the UHPFRC panels failed in bending under static and impact loading conditions, and that the desirable strain-hardening behaviors of UHPFRC continue under high strain rates. The researchers also confirm the appropriateness of a two mass-spring analytical model for the drop tests, as it showed good agreement with the experimental results.

Prediction of UHPFRC panels subjected to aircraft engine impact (Thai and Kim, 2016)

Thai and Kim (2016) investigated the development of a detailed finite element model to predict the impact response of UHPC panels subjected to impact loads from aircraft engine missiles. The lack of empirical formulae to predict the UHPC impact response was the motivation for their study. Current formulae derived from data on RC structures have limitations in predicting UHPC performance because of the differences in the impact energy dissipation capacities of the two materials; this study addresses these limitations through a numerical analysis verified using experimental results from Riedel et al. (2010). Using the numerical analysis, this study provides equations that will better predict a minimum UHPFRC panel thickness to prevent scabbing and perforation after impact.

The geometry of the modeled panels and the impact missile followed the specifications of the experimental study by Riedel et al. (2010) presented earlier in this literature review. The finite element model renderings by Thai and Kim (2016) are shown in **Figure 53**. The rebar cage was embedded in the UHPFRC panel and the missile was placed at an initial location at the geometric center of the face of the panel with its front head directly touching the panel to model the instant before impact occurs.

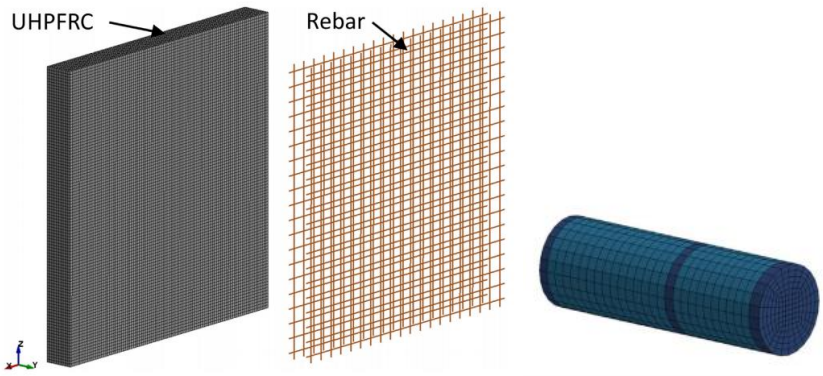

Figure 53: Finite element models of panel, rebar cage, and steel impactor (Thai and Kim, 2016).

The material properties of the model are described for the concrete (UHPC), steel rebar, and steel aircraft missile. For the concrete, the researchers chose the Winfrith model as it best predicted the punching behavior of UHPFRC. The Winfrith model also accounts for differences in strain-rate by multiplying compressive strength, tensile strength, and Young's modulus values with the factors shown in **Figure 54**; the corresponding concrete stress-strain curves are also shown in **Figure 54**. For the steel rebar, an elastic-plastic with kinematic hardening mode was chosen for the model; however, for the steel aircraft missile, a linear isotropic material model with no hardening was chosen. The researchers make this distinction because the steel yield strength in both cases is highly dependent on the strain rate but considering the variation in stress due to strain rate for the missile is outside the scope of the paper. The stress-strain curves for both steel elements are shown in **Figure 54**.

Factor type	0	0.01/s	10/s	300/s
E_T	1.00	1.20	1.39	3.05
E_C	1.00	1.11	1.25	2.74
E_E	1.00	1.15	1.33	1.43

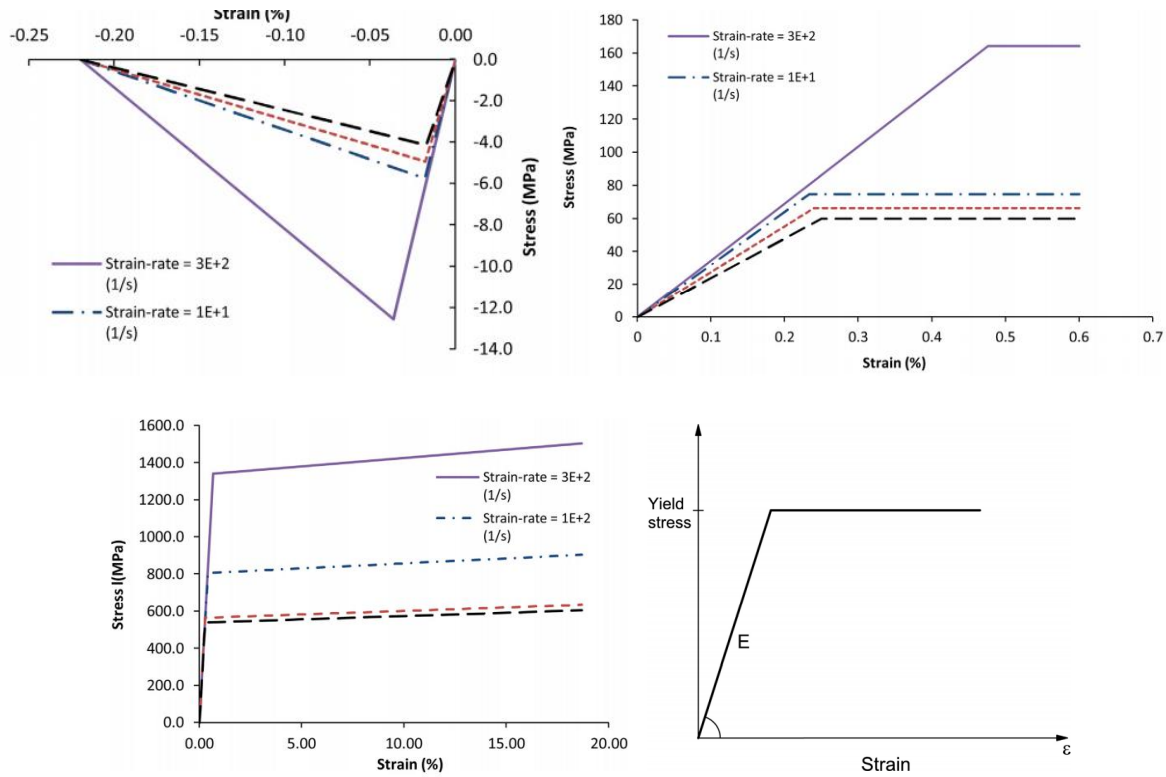

Figure 54: Winfrith model factors and stress-strain curves (Thai and Kim, 2016). Top, Winfrith model modification factors. Middle left, tensile stress-strain curves of concrete; middle right, compressive stress-strain curves of concrete. Bottom left, stress-strain curves of steel rebar; bottom right, generic stress-strain curve of steel missile.

To verify their model, Thai and Kim (2016) simulated four experiments from Riedel et al. (2010) and compared the model results with the measured experimental results. As seen in **Figure 55**, the model was reliable with most predictions within 10% of the actual value.

Exp. No.	Method	Initial velocity (m/s)	Panel failure mode[a]	Residual velocity (m/s)	Scabbing Area (m^2)	Deflection (mm)	Missile failure mode
1	Exp.	194.7	C	−0.86	–	2.00	Bucked
	FEM	194.7	C	−0.82	–	2.21	Bucked
	Difference	*0*	–	*4.7%*	–	*10.5%*	–
2	Exp.	258.7	JS	−0.73	–	12.00	Bucked
	FEM	258.7	JS	−0.69	–	13.12	Bucked
	Difference	*0*	–	*5.5%*	–	*9.33%*	–
3	Exp.	320.0	JP	0.00	0.0837	–	Crushed
	FEM	320.0	JP	0.00	0.0789	–	Crushed
	Difference	*0*	–	*0.0%*	*5.7%*	–	–
4	Exp.	332.0	P	11.00	0.0775	–	Crushed
	FEM	332.0	P	12.00	0.0650	–	Crushed
	Difference	*0*	–	*9.10%*	*16.1%*	–	–

[a] C = Penetration Mode, JS = Just Scabbing Mode, JP = Just Perforation Mode, P = Perforation Mode.

Figure 55: Comparison of model and experimental results (Thai and Kim, 2016). Finite element model results generated by Thai and Kim (2016); experimental results taken from Riedel et al. (2010).

The researchers then conducted a parametric study to examine the effects of missile velocity, fiber type, fiber content, and panel thickness on damage due to impact. Using a cracking strength suggested by Naaman (1972), a fiber coefficient suggested by Suwannakarn (2009), and the modified formulas of Chang and Degen (1981) in the NEI 07-13 standard for scabbing/perforation of reinforced concrete walls, the authors propose the relationships shown in **Figure 56** for scabbing thickness and **Figure 57** for perforation thickness. Multiple curves are shown for different values of β_S and β_P, factors that adjust the Chang and Degen (1981) formulas for UHPC; the authors specify the best value for each graph as described in the figure captions.

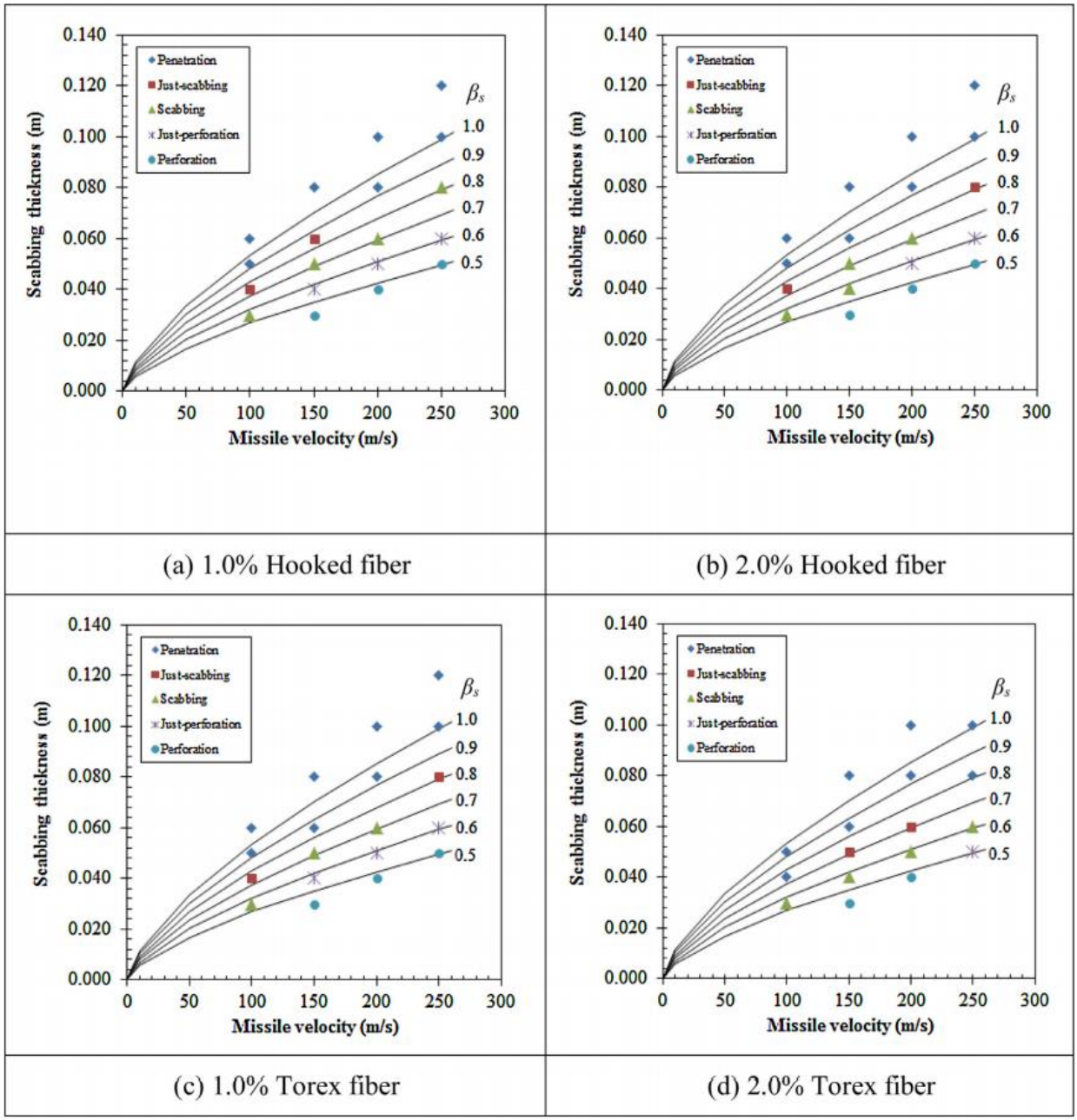

Figure 56: Minimum thickness to prevent scabbing (Thai and Kim, 2016). Graphs presented for various fiber types and contents. For (a) use $\beta_S = 0.85$; for (b) use $\beta_S = 0.82$; for (c) use $\beta_S = 0.82$; and for (d) use $\beta_S = 0.75$.

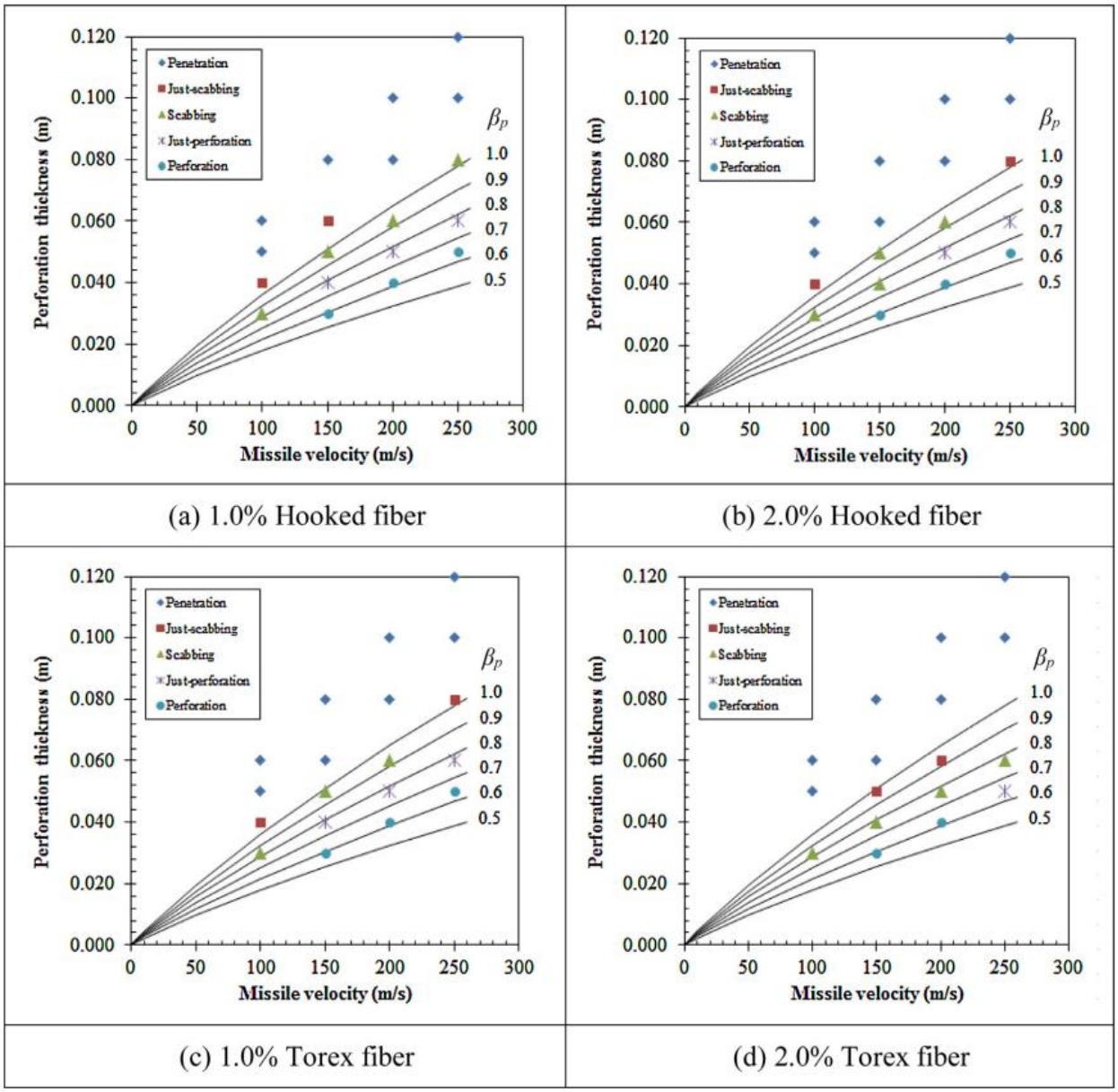

Figure 57: Minimum thickness to prevent perforation (Thai and Kim, 2016). Graphs presented for various fiber types and contents. For (a) use $\beta_P = 0.80$; for (b) use $\beta_P = 0.77$; for (c) use $\beta_P = 0.80$; and for (d) use $\beta_P = 0.70$.

Thai and Kim (2016) concluded that UHPFRC shows much better punching resistance than RC; fiber type and amount significantly impact the panel performance; and the Chang and Degen (1981) formulae can be used to predict scabbing and perforation thickness if used with the recommended β_S and β_P values.

EXPERIMENTAL PROGRAM

Specimen Design

A series of UHPFRC panels were cast to study their resistance to tornado-borne debris, following the guidelines of ICC/NSSA 500. To meet the objectives outlines the introduction, a total of eight panels were cast and tested under impact loading. The panels varied in size, UHPC material, fiber type, fiber content, and reinforcement type. The following sections discuss the reasoning behind each choice as the panels were designed. A final summary of the panel specifications can be found in summary of panel parameters section.

Panel dimensions

The choice of panel dimensions comes from a combination of previous research, engineering judgement, and resource limitations. The basic "full-size" shelter panel will be 4 ft wide by 6 ft tall, which was chosen to accommodate 5 occupants following shelter density requirements of ICC/NSSA 500.

As the main document governing tornado shelter performance, ICC/NSSA 500's criteria for a "passing" or "failed" test was used to assess the performance of each panel. Therefore, a "passing" panel would need to meet the following three requirements: no perforation of the interior surface of the panel (meaning the projectile could not go through the panel); no debris ejected from the interior surface of the panel would damage the kraft paper on the witness screen; and any permanent deformation should be less than 3 inches. This "passing" grade would be earned from resisting a missile weighing 15 lbm at 100 mph, which is equivalent to 5010 lbf-

ft of impact energy. These requirements are imposed on a “full-size” shelter element, which is taken as 4 ft by 6 ft for this study.

There are many examples of UHPFRC panels under impact presented in the literature review, so any previous test that would constitute a “passing” grade under the ICC/NSSA 500 criteria was noted to find a relationship between impact energy, thickness, and mass of the panel. The closest comparison came from Beppu et al. (2020) which used a 18.3 lbm missile at 94 mph, equivalent to 5401 lbf-ft of impact energy, to impact a 45-inch by 45-inch, 680 lbm, 3.54-inch thick and a 45-inch by 45-inch, 907 lbm, 4.72-inch thick UHPFRC panel with 2% steel fibers by volume (used in this study and discussed in the fiber type and content section). The 3.54-inch panels would not pass the ICC/NSSA 500 standards because of the excessive scabbing on the interior surface due to punching shear, shown in **Figure 43**; but, one panel did exhibit a scabbing limit failure, suggested a slightly thicker panel would prevent back face scabbing. The 4.72-inch thick panels pass the ICC/NSSA 500 standard because they do not exhibit any interior surface scabbing, only slight cracking as shown in **Figure 44**. Because the impact specifications are nearly identical, the panels from Beppu et al. (2020) are a good starting point for choosing the dimensions of the panels in this study. One major difference, however, is that Beppu et al. (2020) used a steel nosed missile, which would absorb much less energy during impact than the wood 2x4 projectile prescribed by ICC/NSSA 500. Therefore, a slimmer panel would likely perform just as well when hit by a wood 2x4 projectile. Combining the scabbing limit performance of the 3.54-inch panel with the expectation that a wooden projectile would damage the UHPFRC panel less, a 3-inch thickness was set as the maximum thickness to be considered when designing the panels.

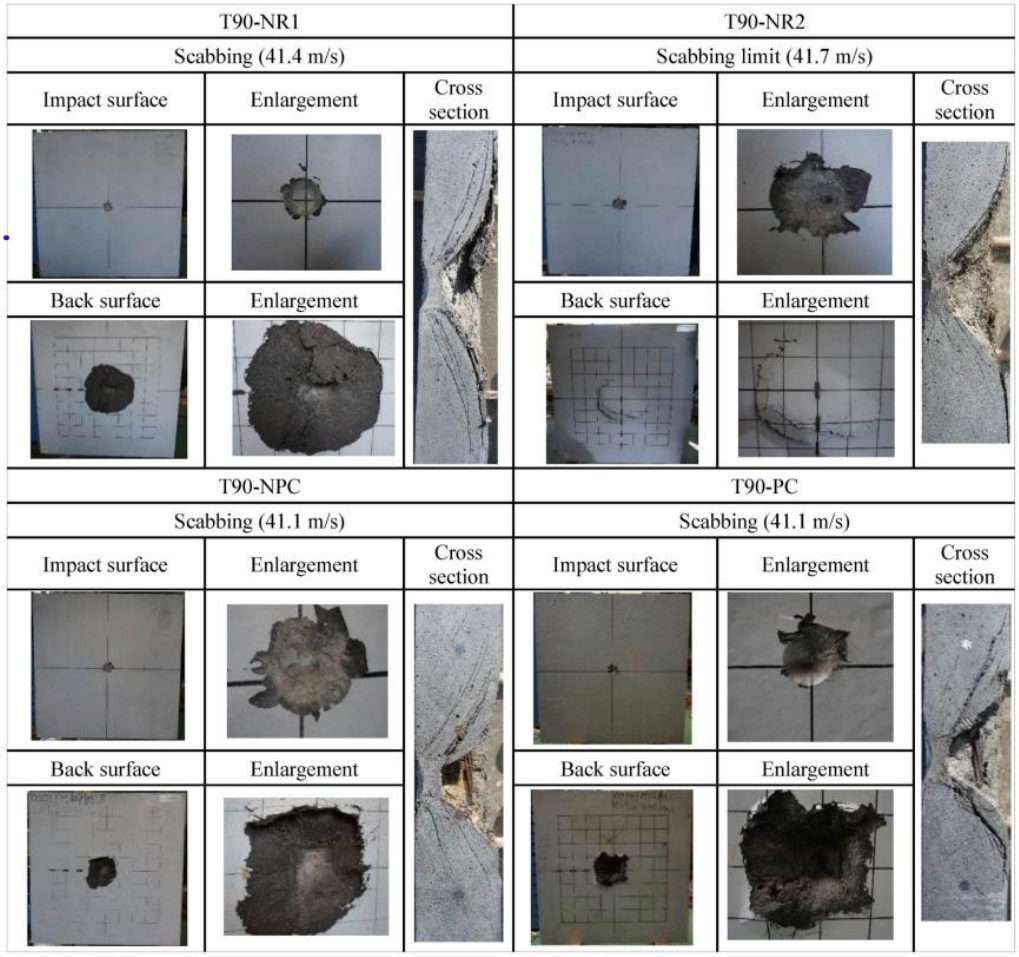

Figure 43: Failure state of 90 mm (3.54 inch) UHPFRC panels (Beppu et al., 2020). Panels fail by punching shear and back face scabbing. The top right photo shows failure by scabbing limit, suggesting a slightly thicker panel would have prevented scabbing.

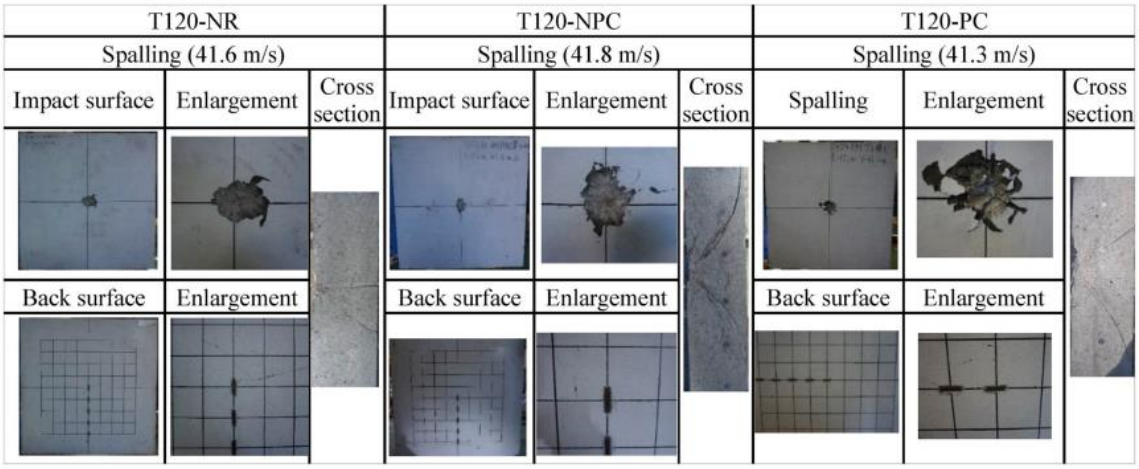

Figure 44: Failure state of 120 mm (4.72 inch) UHPFRC panels (Beppu et al., 2020). Panels fail by front face spall, with no back-face scabbing.

Another approach to estimating the required thickness comes from comparing mass of the panel to impact energy. The mass of the panel is an indirect way of measuring the amount of steel fibers present because the amount of fiber reinforcement is based on the weight of the panel. As fibers are shown to be the main energy dissipation method of UHPFRC under impact loading, the correlation between impact energy and mass (i.e. fiber content) could prove a more accurate way to predict the performance of the panel and its required thickness. Comparing to the same 45-inch by 45-inch, 680 lbm, 3.54-inch thick panel from Beppu et al. (2020) discussed earlier, a 4 ft by 6 ft tornado shelter panel would require a 2.12-inch thickness to match the weight of the 680 lbm panel. Using the same logic when considering a steel missile impact versus a wood missile impact, a 2-inch thick UHPFRC panel was chosen as the new maximum panel thickness.

The effect of flexural stiffness on the panel performance was also considered. Conventional design usually focuses on increasing flexural stiffness to mitigate deflection; however, a “passing” tornado shelter panel by ICC/NSSA standards can actually tolerate a large peak deflection as long as debris is not ejected from the interior face and the final deflection is less than 3 inches. Therefore, decreasing the flexural stiffness to intentionally allow the panel to deflect more would force the panel to fail by excessive deflection rather than a weaker (and more dangerous) failure mode of punching shear, like the 3.54-inch panels from Beppu et al. (2020). The easiest way to decrease flexural stiffness is to decrease the thickness of the specimen, whose cube is proportional to moment of inertia. Two thicknesses, 1.25-inch and 1.625-inch, were thereby chosen for the experimental panel design.

Finally, the suggestions of the predictive analytical model presented in the literature review are compared with the previously discussed thickness guidelines. Thai and Kim (2016) graph minimum thicknesses to prevent scabbing for a 3.5 lbm missile at a given impact speed, shown in **Figure 56** for 2% steel fiber reinforcement by volume. ICC/NSSA 500 gives the missile impact speed as 100 mph, but for a 15 lbm missile. To adjust the overall impact energy to account for the higher weight, **Figure 56** should be used with a speed of approximately 656 mph (200 m/s) resulting in a minimum thickness of 0.6 m, or 2.36 inches. This is comparable to the 2.12-inch thickness to reach energy-mass equivalency discussed earlier. The work by Thai and Kim (2016) only gives guidance for hooked and torex fibers; following papers reviewed by Yoo and Banthia (2017), straight fibers may perform better under impact loads and the overall thickness of the panel could be reduced because of the improved energy dissipation performance of the straight fibers.

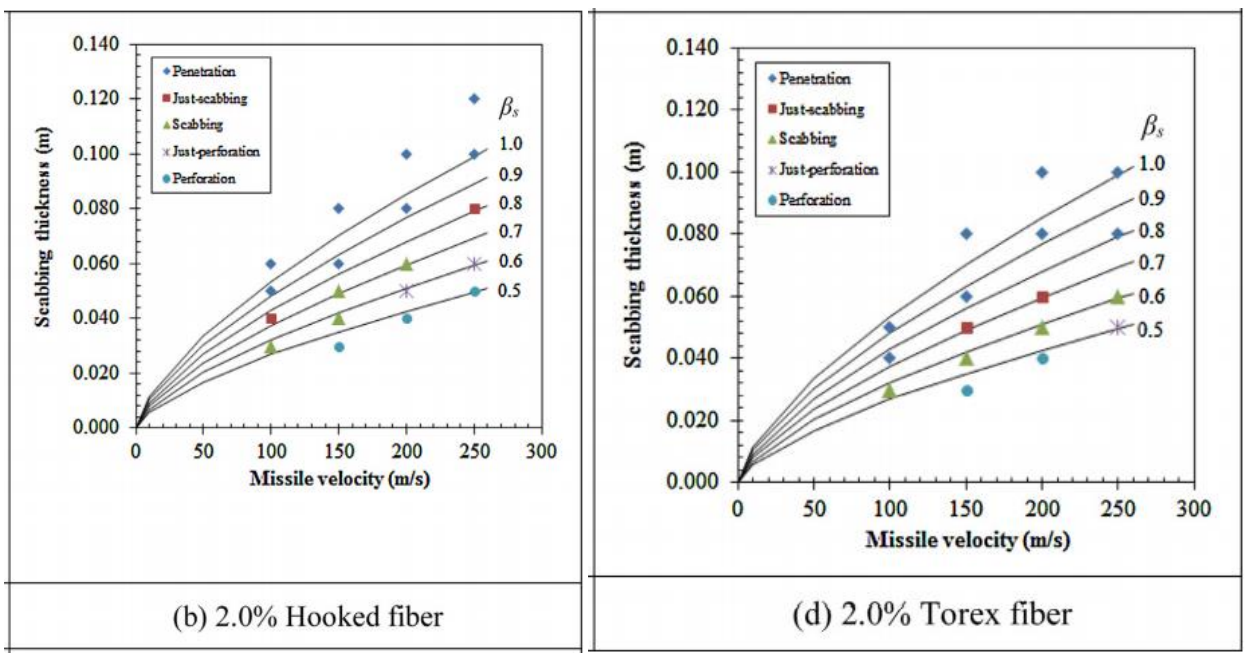

Figure 56: Minimum thickness to prevent scabbing (Thai and Kim, 2016). Graphs presented for various fiber types and contents. For (b) use $\beta_S = 0.82$ and for (d) use $\beta_S = 0.75$.

After settling on two panel sizes (1.25-inch by 4 ft by 6 ft and 1.625-inch by 4 ft by 6 ft), the limited availability of UHPC in the laboratory affected the approach taken by the researchers. The panel thicknesses, although based on sound engineering judgement, was not guaranteed to work. To prevent wasting material on full size panels that did not work, smaller dimensioned panels were cast first. After evaluating their performance, adjustments could be made, and larger panels could be cast. The preliminary panels (AG_2x12 and AS_2x12) were only 4 ft tall, 1 ft wide, and a maximum of 2 inches thick to keep the UHPC volume minimum. After seeing the performance of those panels, the design was changed to 6 ft by 1 ft with each thickness, then 6 ft by 2 ft with each thickness to see if the results of a smaller panel could be scaled up to the larger dimensioned panels. A "full size" panel would have been 6 ft by 4 ft, but resources did not allow that much UHPC to be poured. For the panels investigating the effect of fiber type on panel performance, the panel size was changed back to 6 ft by 1 ft and 1.25-inch thick. **Figure 63** provides a detailed summary of each panel's dimensions. Examples of formworks built for each size are shown in **Figure 58**.

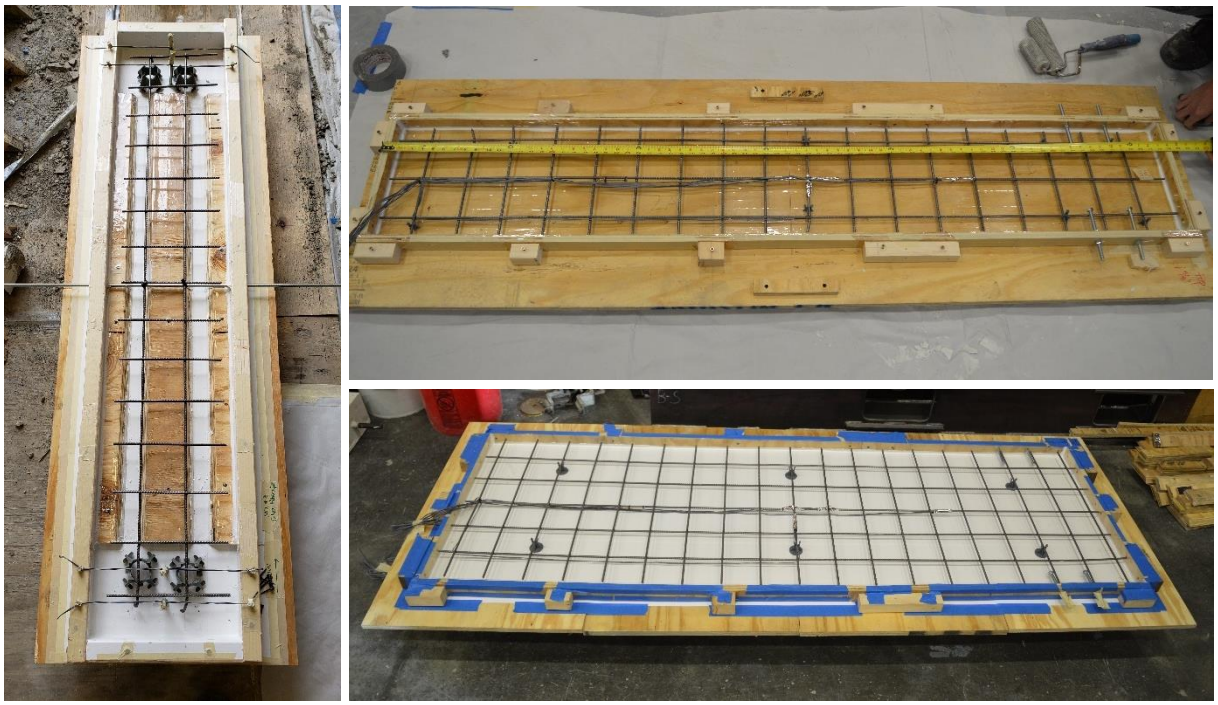

Figure 58: Formworks of each panel size. Left, formwork for 4 ft by 1 ft; top, 6 ft by 1 ft formwork; and bottom, 6 ft by 2 ft formwork.

UHPC type

As hinted at earlier, the research was limited to the type and amount of UHPC currently available in the laboratory. The materials in the lab were donated or purchased from commercial UHPC manufacturers around the world. Two brands were used in this study: Aalborg Extreme and Steelike, manufactured by Lehigh White Cement Company and Steelike, Inc., respectively (AALBORG EXTREME, n.d. and Steelike Concrete, 2021). A comparison of the material properties of each type will be presented later in the study in Material Property Testing Results section.

Figure 59: Bags of UHPC types. Aalborg Extreme (left) and Steelike (right) premix.

Aalborg Extreme was used to pour panels that were focused on understanding an acceptable panel thickness and the relationship between mass and energy absorption. Steelike was used to pour panels that examined the effect of fiber type on impact resistance. See **Figure 63** for details on which panels used each type of UHPC.

Both mixes rely on a similar procedure. Using a mid-sized mixer, the bags of dry premix are added first. Water and superplasticizer are added next, over a specified amount of time to allow for good dispersion among the cement particles, and the resulting blobs of UHPC are allowed to mix until the consistency turns to a smooth, cake-batter-like texture. Reinforcing fibers are then added, mixed for another five to six minutes to ensure even distribution throughout the mix, and finally the UHPFRC is poured. In the lab, the UHPFRC is generally

poured into buckets first, then transferred to the specimen molds because of space and sizing of the molds.

Aalborg Extreme was a much less flowable mix than Steelike during mixing and required extra superplasticizer to increase its workability.

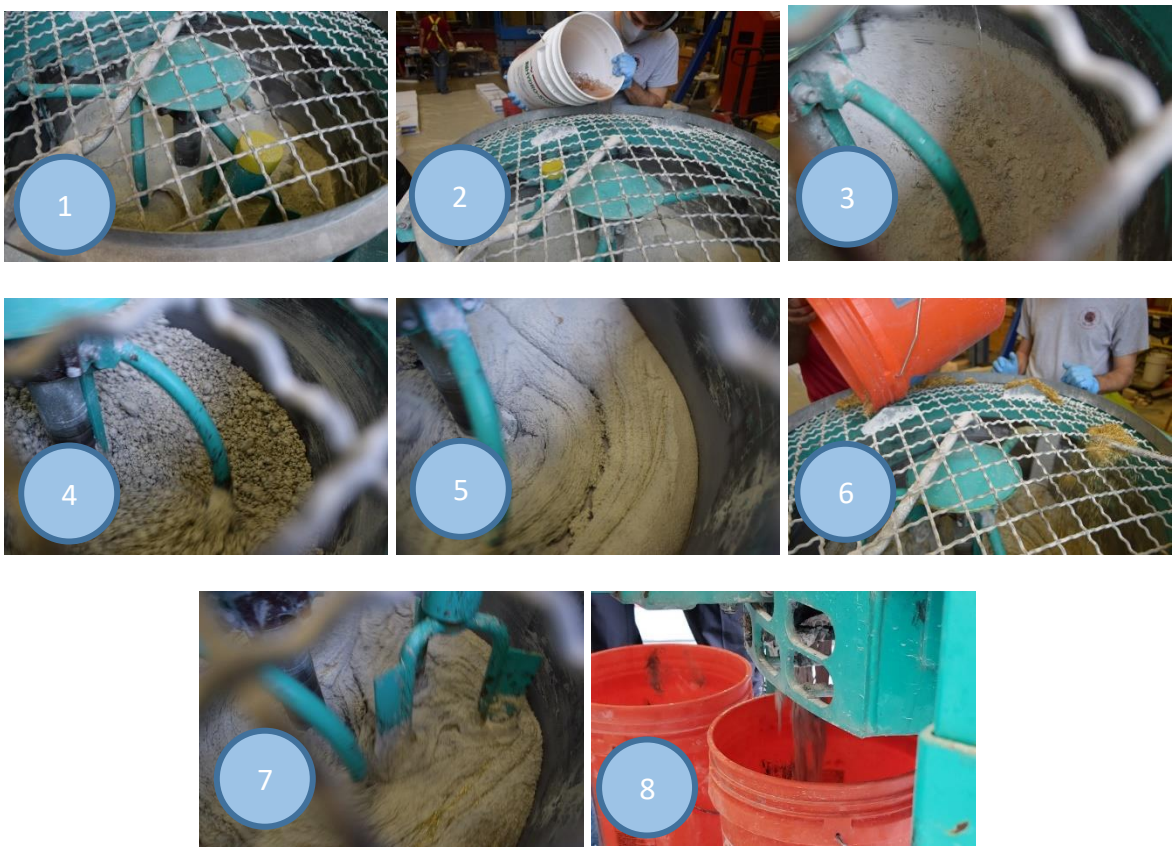

Figure 60: Mixing procedure of UHPC. 1) The dry premix in the mixer, 2) adding water and superplasticizer, 3) clumps of cement forming around water particles, 4) blobs of UHPC forming, 5) cake-batter consistency achieved, 6) steel fibers being added, 7) fibers mixing into the UHPC, and 8) UHPFRC poured into buckets for transfer to formwork.

Curing methods for both types of UHPC mix were the same. After being poured, the panels were covered with plastic and allowed to set in ambient laboratory conditions for 24 hours. They were then moved to an environmental chamber to cure in high temperature, high humidity conditions to encourage rapid strength gain. The environmental chamber was

maintained at 40 °C (104 °F) and 95% humidity. The panels stayed in the environmental chamber for six days before being removed and demolded.

Fiber type and content

The effect of fiber type and content on the material properties oh UHPC was well documented by Yoo and Banthia (2017). The compiled evidence suggests that straight fibers perform better than hooked or twisted fibers under the high strain rates of impact loading because the straight fibers' pullout mechanism is nondestructive to the surrounding UHPC and their shape is less likely to decay under extreme strains. Their research also discusses the benefits of polymeric fibers under impact loading, as they are less likely to fail by fiber pullout, and the limitations of polymeric fibers, as they are unlikely to reach full pullout capacity due to low tensile strength. Finally, increasing fiber content was shown to increase global performance when dosed up to 6% by volume; however, local response of the UHPFRC plateaued around 2% by volume.

Throughout all the specimens tested in this project, three different types of fibers were used. The first is a straight ½-inch-long, polymer glass fiber manufactured by Owens Corning (Owens Corning, n.d.). The other two are both steel fibers manufactured by Bekaert, one a straight ½-inch-long fiber and the other a bent 1 1/8-inch-long fiber (Bekaert, n.d.). All three are pictured in **Figure 61**.

Figure 61: Fiber types. From left to right, the polymer glass fibers, straight steel fibers, and bent steel fibers. The bent steel fibers are bound by water-dissolvable glue and break apart when mixed into the UHPC.

The first two panels (AG_2x12 and AS_2x12) were one of the first attempts to pour Aalborg Extreme by the researchers. To get a feel for the mix, the company's recommended type and amount of fibers were used without consideration for the effect they would have on the impact resistance of the panel. One panel used polymer glass fibers dosed at 1.5% by weight of dry mix, while the other used straight steel fibers at 5% by weight of dry mix.

Following the results of the impact testing discussed in the preliminary panel results section, several changes were made for subsequent Aalborg Extreme panels. The next four panels (AS_1.25x12, AS_1.625x12, AS_1.25x24, and AS_1.625x24) all used the straight steel fibers at 2% by volume of dry mix – equivalent to about 7.35% by weight of dry mix. The decision to use steel fibers instead of polymer glass fibers was supported by the performance of the first two panels as well as the research reviewed by Yoo and Banthia (2017). Additionally, because current research also suggests straight fibers perform better under impact loads than bent or twisted fibers, the straight steel fibers were chosen over the bent steel fibers. The amount of fibers was increased for similar reasons, but the dosage was capped at 2% by volume as local response would be more critical than global response for a hard-nosed projectile impact.

To add to the knowledge of fiber shape's effect on impact resistance in UHPC, the final two panels (SS_1.25x12 and SB_1.25x12) each used a different shape of steel fiber and the Steelike UHPC. The researchers had experience pouring Steelike, so both panels were immediately dosed with 2% by volume (7.35% by weight) of dry mix.

Steel reinforcement

When deciding whether to include additional steel reinforcement in the UHPFRC panels, results from Beppu et al. (2020) and Riedel et al. (2010) were informative on the benefits of including steel reinforcement. Both studies demonstrate that steel reinforcement helps confine the UHPC particles, thereby increasing strength and decreasing debris ejection when impacted. Additional steel reinforcement was included in all the panels because of its demonstrated benefits. The first two panels (AG_2x12 and AS_2x12) used #3 rebar as longitudinal flexural reinforcement as well as pieces bent into U-shapes for transverse shear reinforcement. After some issues with constructability and the questionable performance of the panels during testing, the remaining panels switched to a ¼-inch diameter, 4-inch grid wire mesh more like the type used in Beppu et al. (2020). Both reinforcement configurations are shown in **Figure 62**.

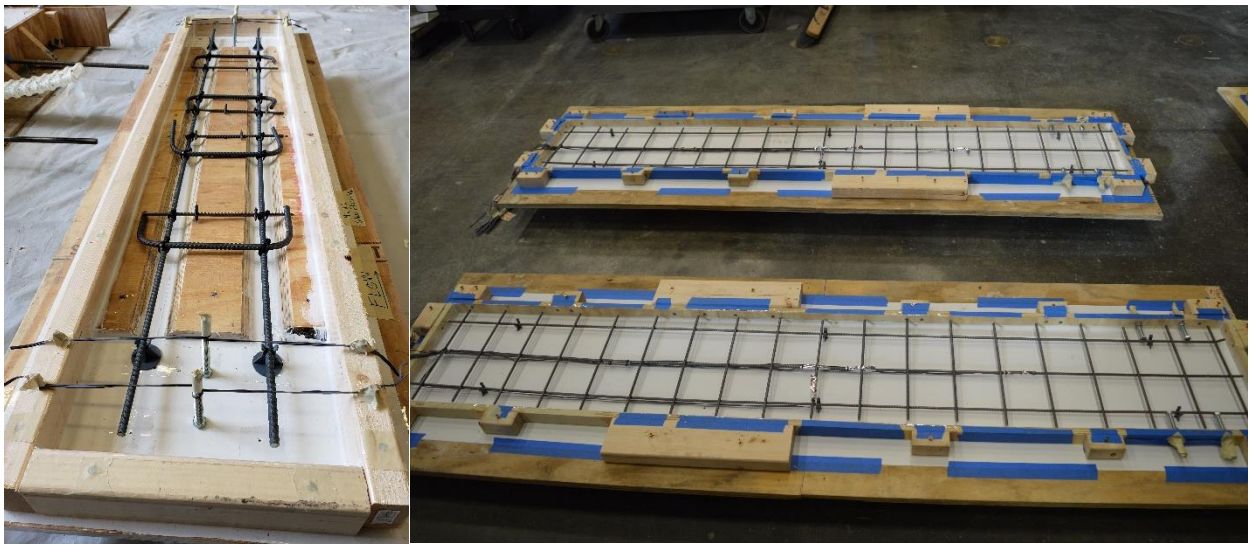

Figure 62: Steel reinforcement types. Left, #3 rebar and right, steel wire mesh used for reinforcement inside each UHPFRC panel.

Summary of panel parameters

The following chart summarizes the dimensions, UHPC type, fiber type, fiber content, and steel reinforcement of each panel as discussed previously.

Figure 63: Summary of UHPFRC panel specifications.

Specimen Name	***Thickness (in)***	***Width (in)***	***Height (in)***	***UHPC Type***	***Fiber Type***	***Fiber % by volume***	***Reinforcing Steel Type***
AG_2x12	2	12	48	Aalborg Extreme	Glass	1.4	Rebar
AS_2x12	2	12	48	Aalborg Extreme	Straight steel	1.4	Rebar
AS_1.25x12	1.25	12	72	Aalborg Extreme	Straight steel	2.0	Wire mesh
AS_1.625x12	1.625	12	72	Aalborg Extreme	Straight steel	2.0	Wire mesh
AS_1.25x24	1.25	24	72	Aalborg Extreme	Straight steel	2.0	Wire mesh
AS_1.625x24	1.625	24	72	Aalborg Extreme	Straight steel	2.0	Wire mesh
SS_1.25x12	1.25	12	72	Steelike	Straight steel	2.0	Wire mesh
SB_1.25x12	1.25	12	72	Steelike	Bent steel	2.0	Wire mesh

Experimental Test Setup

Debris cannon

There are four debris cannons available to the researchers, each with 8-foot-long, 8-inch diameter barrels. The four cannons are arranged in a two by two formation as shown in **Figure 64**. Multiple cannons can be used at the same time to simulate a debris cloud; however, only one cannon was used at a time during testing for multiple reasons. First, ICC/NSSA 500 standards call for 2x4s shot one at a time at the test specimen. Second, only one cannon was outfitted with an electric actuator such that the aim of the cannon could easily be adjusted between tests. Therefore, the bottom left cannon shown in **Figure 72** was used for every test.

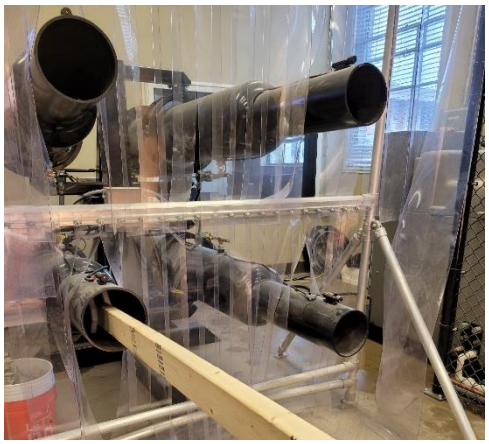

Figure 64: Debris cannon.The four debris cannons available in the laboratory, with a wooden projectile loaded in the bottom left cannon that was used for every test.

The cannons are powered by an air compressor that can charge to up to 150 psi per cannon and is controlled by an external programmable board shown in **Figure 65**. The cannons can be manually charged up and down or programmed to a firing sequence. As only one cannon was used at a time, the cannon was manually charged to the correct pressure for each test.

Figure 65: Air compressor control board. Buttons on the bottom right of the board control the cannon used for every test.

Projectiles and impact velocity

The projectiles, as specified by ICC/NSSA 500, were 2x4 dimension lumber weighing approximately 15 lb at the time of firing. The debris cannons rely on a seal forming between the back of the projectile and the back of the cannon to use the compressed air to accelerate the projectile. The cross-section of a 2x4 will obviously not form a seal with the 8-inch diameter cylindrical barrel of the cannons; therefore, a circular 8-inch plastic piece was attached to each 2x4 to create the required seal. Additionally, to ensure the 2x4 was accelerated parallel to the cannon's longitudinal axis, which was crucial to having the projectiles impact the panels at the correct location, plastic "wings" were attached to each side of the 2x4 to act as guides as the 2x4 exited the cannon barrel. A fully constructed projectile is shown in and out of the cannon barrel in **Figure 66**.

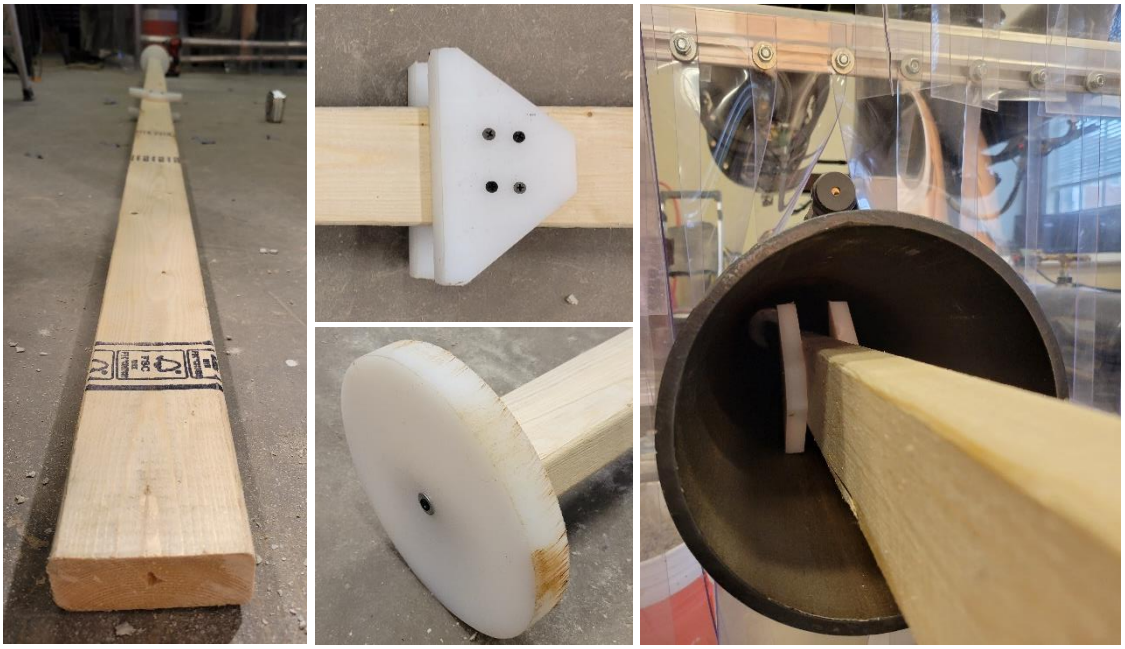

Figure 66: 2x4 projectile. Prepared for testing with a plastic disk on the back end and plastic "wings" attached to rest just inside the entrance of the cannon.

ICC/NSSA 500 also requires that the projectiles are between 13 and 14 feet long. This requirement was not met for any of the projectiles, as they were all 12 feet or less. However, the weight requirement was deemed the more important parameter, as it has a significant effect on impact energy while length of the projectile does not. The weight and length of each projectile is summarized in **Figure 75**.

Speed gates in the path of the projectile's flight, shown in **Figure 67**, were used to measure the velocity of the projectiles just before impact. Previous research conducted in the debris cannon laboratory had generated a relationship between the cannon's pressure in psi and the speed gates' measured impact velocity in mph. This relationship, graphed in **Figure 67**, was used to choose an appropriate pressure for the target impact velocity. ICC/NSSA 500 specifies a speed of 100 mph for testing vertical elements and a speed of 67 mph for horizontal elements; a

target speed of 100 mph was used for all specimens because a panel that could resist a higher impact speed could certainly resist a projectile at a lower speed. ICC/NSSA 500 also says that the 100-mph target speed is for a full-size shelter element. As explained earlier, the sizes of the specimens were limited by laboratory resources. Therefore, the target impact speed was adjusted to keep the ratio of impact energy to panel mass the same – the main impact resistance mechanism of UHPC is energy dissipation via cracking and fiber spanning, and the amount of available cement particles and fibers is directly proportional to the size (mass) of the panel. Assuming the impact energy would be equivalent to the kinetic energy of the projectile just before impact, calculated in **Equation 1** and supported by previous researchers such as Verma et al. (2016), a panel with 25% the size of the "full-size" 4 ft by 6 ft panel should resist 25% of the kinetic energy imparted by a 100-mph projectile. The 1 ft by 6 ft panels, therefore, should be tested with 50-mph projectiles, which would impact 25% of the energy of a 100-mph projectile. This correction was not utilized when testing the first two panels (AG_2x12 and AS_2x12) which is part of the reason they performed so poorly. When shot at a full 100 mph, the first two panels experienced nearly four times as much energy than they should have when scaled by mass of the panel. The velocity, impact energy, and impact energy normalized by mass are summarized in **Figure 75**.

$$KE = \frac{1}{2} m {v_2}^2 \tag{1}$$

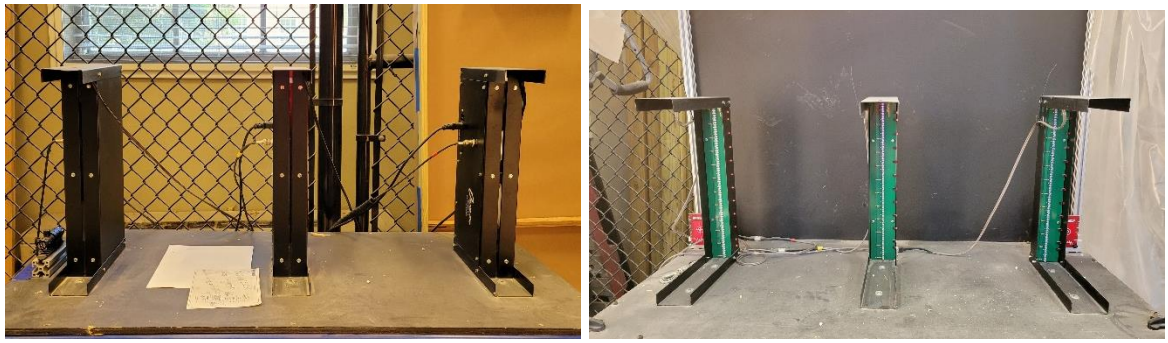

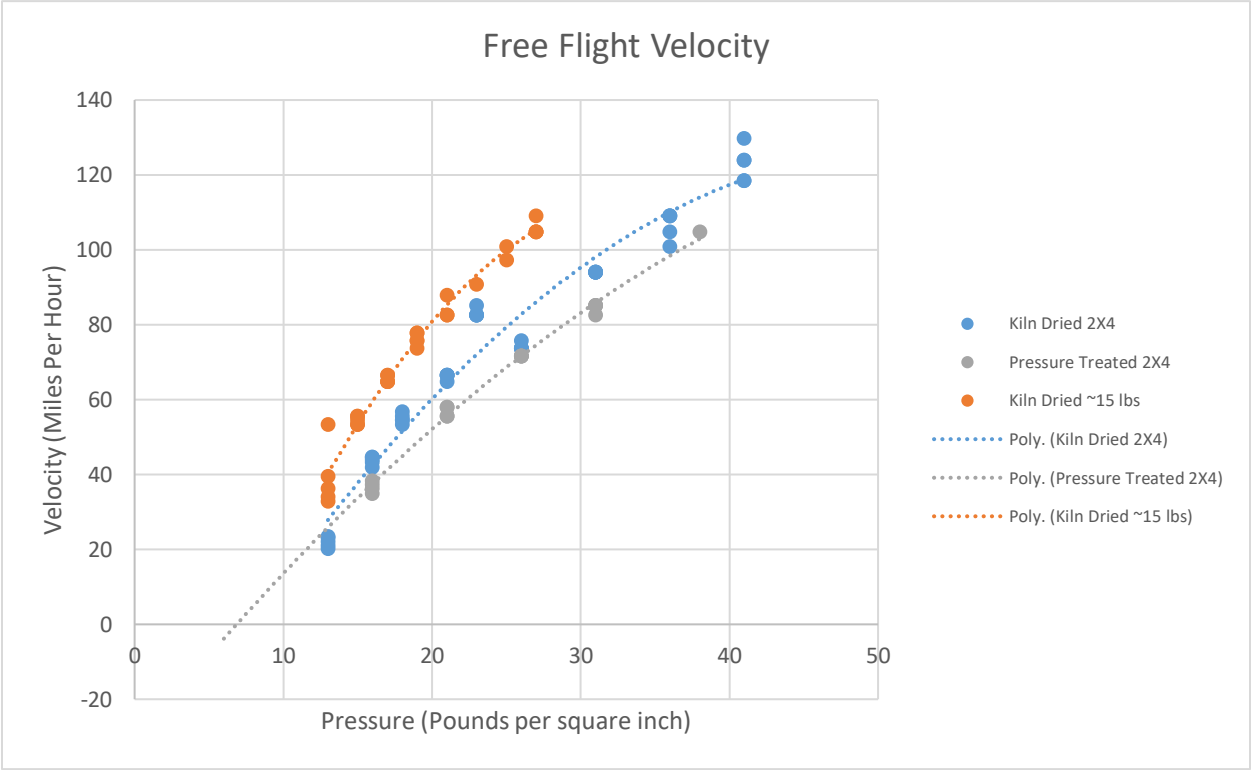

Figure 67: Speeds gates and free flight velocity versus pressure graph. Top, three speed gates, with one set on each side of the room, measured the impact speed of each projectile. Bottom, relationship between debris cannon pressure and resulting impact velocity of the 2x4 projectile. The orange curve is the most accurate for predicting the speed of the projectile.

Steel frame and panel attachment

During testing, the panels were attached to a steel frame that is bolted into the floor of the debris cannon lab, as shown in **Figure 68**. The steel frame consists of two W8x28 cross beams and two W10x112 columns. The columns have bolt holes every 6 inches along its height, allowing the cross beams to be raised or lowered to accommodate the height of each specimen.

Figure 68: Steel frame. The steel frame in the debris cannon lab features two columns and two cross beams attached with steel angles.

For the first two panels (AG_2x12 and AS_2x12), the panels were bolted between the steel cross beams and an additional steel channel on the top and bottom. This configuration was challenging to install, so subsequent tests used a simpler method of clamping the panel to the steel cross beams with four steel C-clamps, as shown in **Figure 69**. Bolting the UHPC panel between the steel cross beam and another steel channel also created a strong fixed-fixed connection type, which is not realistic of a tornado shelter that would probably be free standing and braced only by the edges of the panels surrounding it. Changing to the C-clamps attempted to create more of a pin-pin connection type, which is more accurate of a set of panels arranged in a tornado shelter.

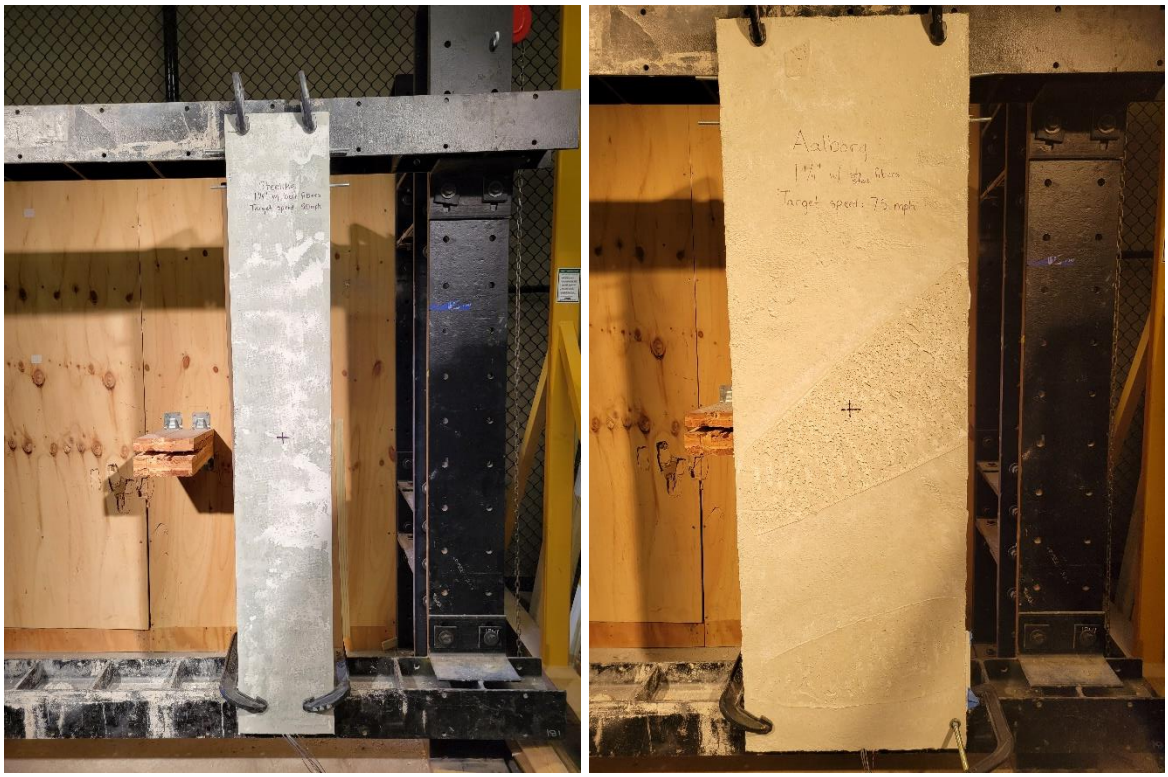

Figure 69: Panels clamped to steel frame. Clamps located on top and bottom crossbeams.

Witness frame

Several of the ICC/NSSA 500 pass/fail criteria are based on the presence of a "witness frame," consisting of kraft paper stretched over a stiff frame of wood or other material. The witness frame mimics the presence of occupants on the other side of the testing surface such that damage to the witness frame would constitute injury to an occupant. The witness frame for each test was constructed to cover the exposed area of the panel between the steel cross bars and was installed within 5 inches of the back surface of the panel, as specified in ICC/NSSA 500 and shown in **Figure 70**. A #70 kraft paper was stretched across the wooden frame to capture any damage from spall or ejected debris that might occur upon impact.

Figure 70: Witness frame. A 1ft wide wooden witness frame with #70 kraft paper stretched over the opening. The witness frame was installed on the steel cross beams within 5 inches of the back of each UHPFRC panel. For the 2 ft wide panels, a 2 ft wide witness frame was used.

Instrumentation and measurements

To capture the response of the panel after impact, two primary measurements were taken. First, a set of strain gauges was included in all but the two preliminary panels. They were excluded from the preliminary panels as the function of the preliminary panels was to qualitatively assess an appropriate thickness for future panels. The strain gauges were attached to the wire mesh in the configuration shown in **Figure 71** and would therefore capture the strains at the center of the panel, assuming that the bond between the UHPC and steel reinforcement would cause them to move the same amount. Two types of stain gauges from Tokyo Measuring

Instruments Lab were used: a 5 mm (0.197-inch) steel-measuring gauge named YFLA-5-3LJCT-F and a 50 mm (1.97-inch) concrete-measuring gauge named PMFL-50-2LJRTA. Both gauges and the method used to secure them to the wire mesh are shown in **Figure 72**. A Nation Instruments (NI) Data Acquisition System (DAQ) was used to measure the strains throughout the testing.

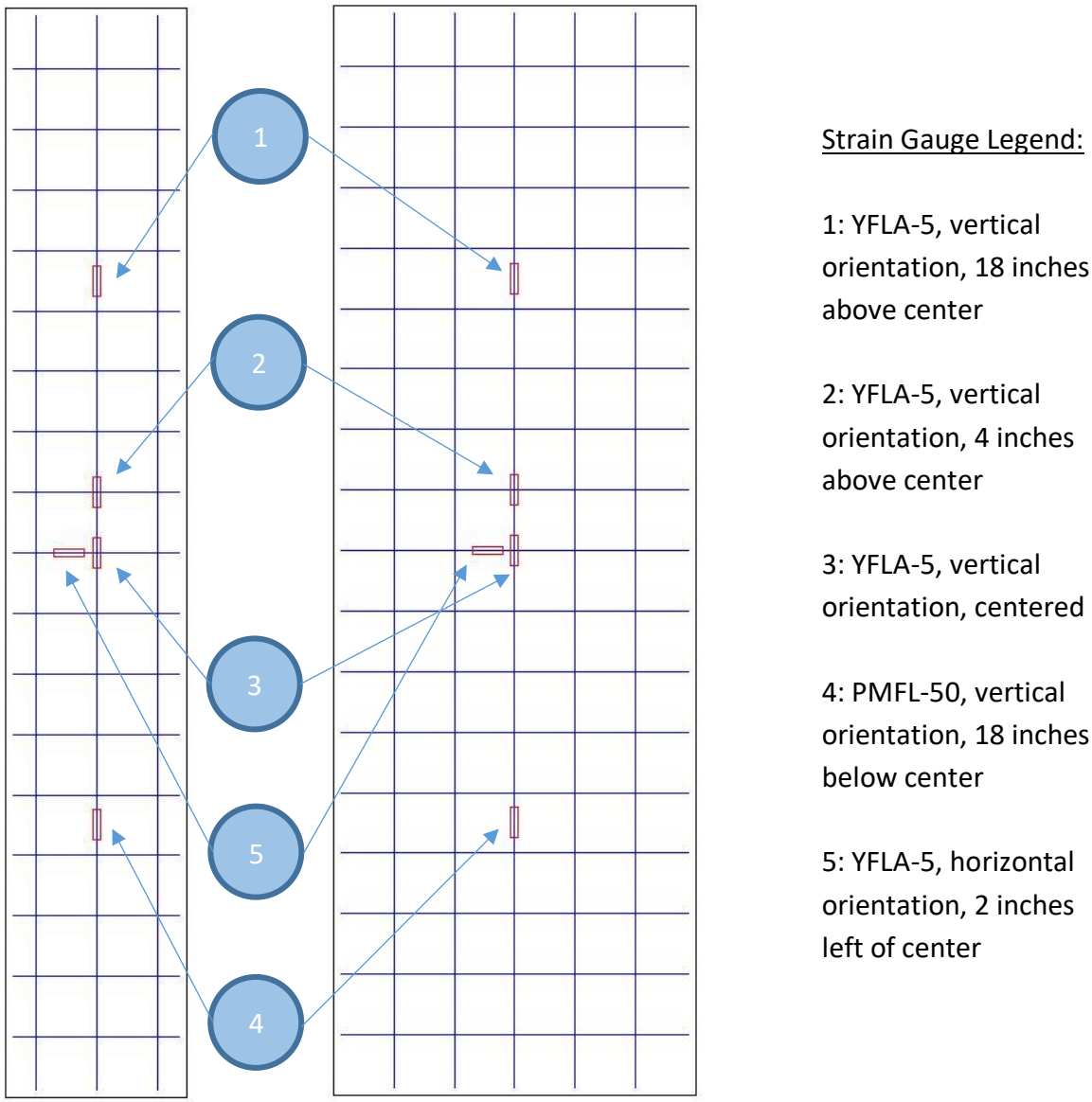

Figure 71: Strain gauge configuration map. Left, the 12-inch wide panel and right, the 24-inch wide panel. Vertical strain gauges were applied at the center of the panel regardless of the width of the panel, and the horizontal strain gauge was applied 2 inches from the center also regardless of the panel width.

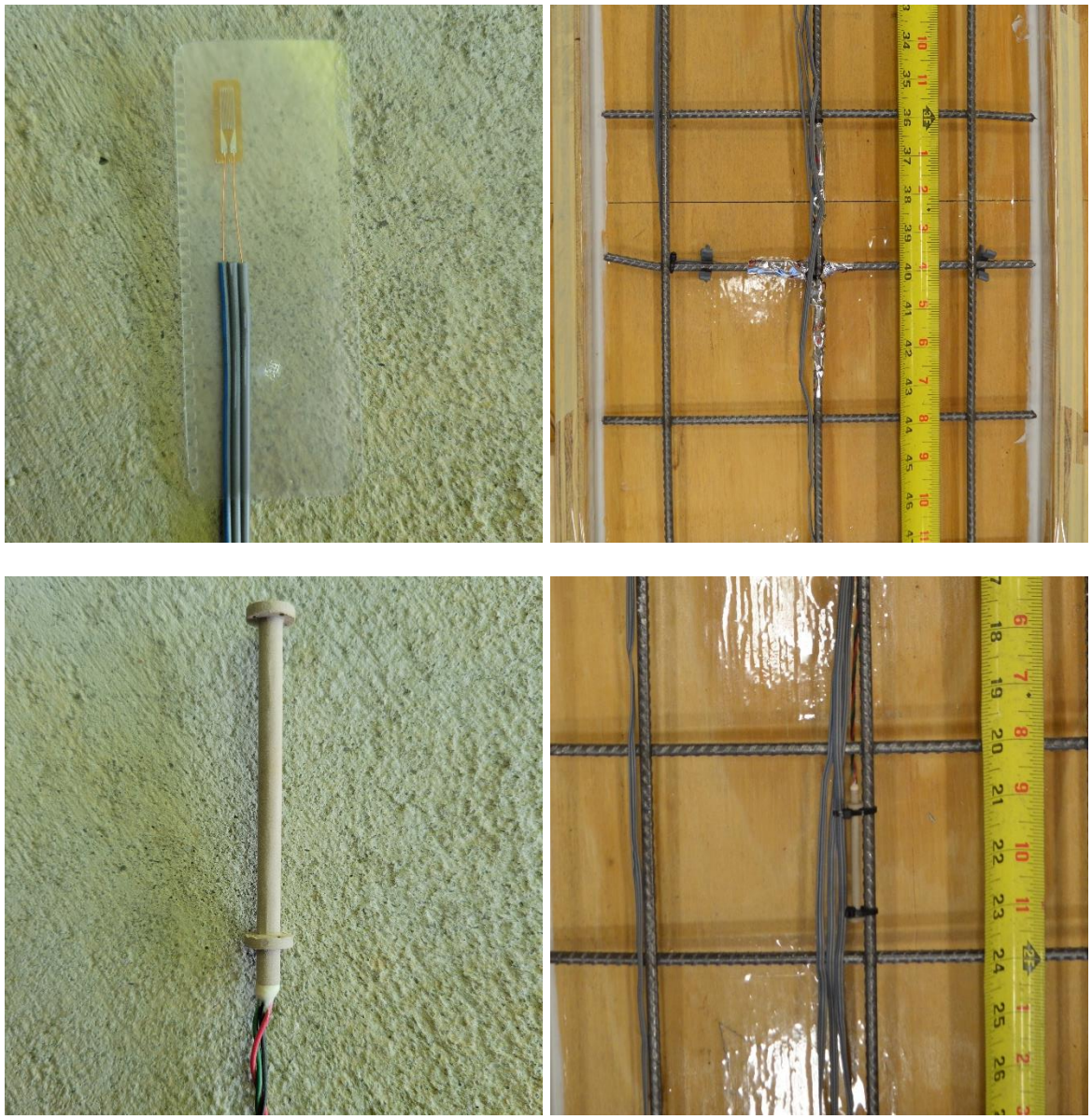

Figure 72: Strain gauges. Top left, a YFLA-5-3LJCT-F strain gauge; top right, YFLA-5-3LJCT strain gauges applied to the steel wire mesh and covered in aluminum tape to repel moisture; bottom left, a PMFL-50-2LJRTA strain gauge; and bottom right, a PMFL-50-2LJRTA strain gauge zip-tied to the steel wire mesh.

The displacement of the panel after impact was tracked with a series of colored markers, shown in **Figure 73**. Each panel had three sets of markers spaced 4 inches apart along its length: green markers for the front edge of the panel, red markers for the back edge of the panel, and blue markers along the centerline of the panel. Using a high-speed camera to record the impact

and a video analysis software called Kinovea to track the movement of each marker, the displacement of the panel at any moment during the impact and resulting oscillation could be measured (Charmant, n.d.). A maximum overall displacement and the final permanent displacement was also calculated using the same procedure.

Figure 73: Colored markers on side of panel. An example of the colored stickers on the side of each panel used to track the displacement of the panel.

Summary of experimental setup

A schematic of the overall laboratory setup during each test is included in **Figure 74**.

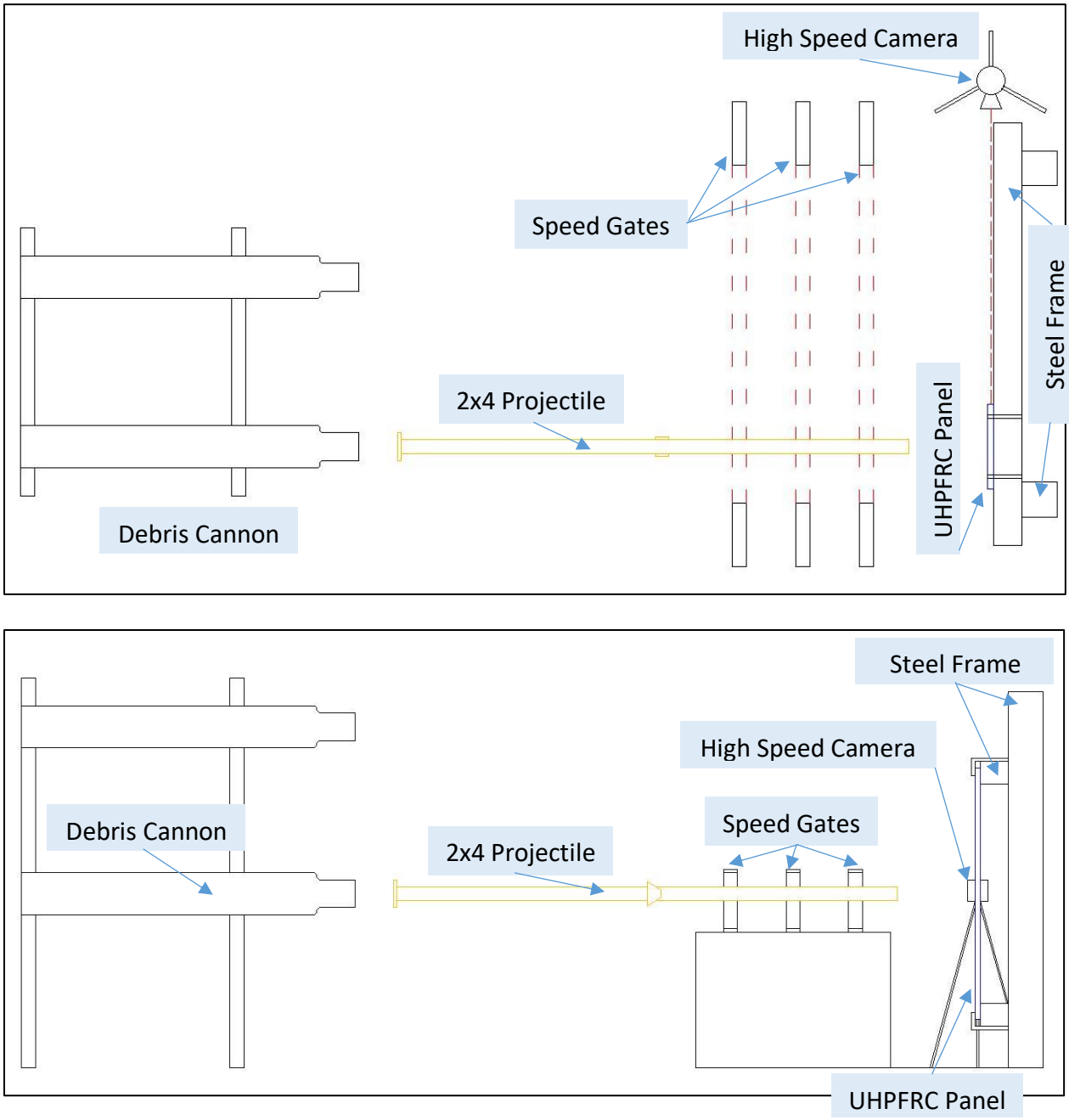

Figure 74: Experimental setup of debris cannon laboratory. Above, a top view and below, a side view of the laboratory setup.

The following chart summarizes the missile length, missile weight, missile speed, impact energy, and impact energy per mass of panel as discussed previously. The bottom two rows show the ideal conditions for a 4ft wide by 6 ft tall "full size" panel of each thickness for comparison. All panels were subjected to a greater energy-to-mass-of-panel ratio than the larger panels would have been.

Figure 75: Summary of impact testing parameters for each panel.

Specimen Name	***Missile Length (in)***	***Missile Weight (lbf)***	***Target/Actual Missile Speed (mph)***	***Impact Energy (lbf-ft)***	***Impact Energy per Mass of Panel (lbf-ft/lbm)***
AG_2x12	132	15.0	100 / 100	5010	64.2
AS_2x12	132	15.0	100 / 100	5010	64.2
AS_1.25x12	132	15.0	50 / 53	1407	14.1
AS_1.625x12	144	14.7	75 / 75	2762	21.2
AS_1.25x24	144	15.2	75 / 73	2706	13.5
AS_1.625x24	129	15.1	100 / 100	5044	19.4
SS_1.25x12	144	15.2	50 / 56	1592	15.9
SB_1.25x12	144	15.2	50 / 56	1592	15.9
Full_1.25	162	15.0	100	5010	12.5
Full_1.625	162	15.0	100	5010	9.6

Material Properties Testing

To understand the behavior of the panels, compression and flexural tests were conducted on UHPFRC samples matching the characteristics of each panel's composition. Aalborg Extreme with straight steel fibers, Steelike with straight steel fibers, and Steelike with bent steel fibers were the three different UHPC/reinforcement combinations used in the impact testing; therefore, flexural and compression tests were done for those same combinations.

Compression strength

Concrete material properties rely heavily on knowing the compressive strength of the concrete, and UHPC is no exception. UHPC is known for its impressive compressive strength, but compressive strength is also the gateway to other material properties such as shear strength, bending moment capacity, and modulus of elasticity. It is therefore crucial to know the compressive strength of each batch of UHPC.

To measure compressive strength, 2 in cubes were cast from the same mixture as each of the UHPFRC panels. Freshly poured cubes in their reusable steel molds are shown in **Figure 76**. The cubes were tested in the compressive testing machine shown in **Figure 76** following the procedure in ASTM C39.

Figure 76: Compression cubes and testing machine. Top, various sets of cubes being cast from UHPFRC for compression testing. Bottom left, the compressive testing machine and bottom right, a cube loaded in the compressive testing machine.

Flexural strength

The UHPFRC panels were expected to fail primarily in flexure due to excessive deformation, so the flexural behavior of each UHPC/fiber combination was also studies using the four-point-bending method detailed in ASTM C1609 and ASTM C1856. Beam size for a four-point-bending test depends on the length of the fibers used in the UHPFRC; therefore, 3-inch by 3-inch by 14-inch specimens were poured for the Aalborg Extreme and Steelike with straight steel fibers (fiber length of 0.5-inch) while 4-inch by 4-inch by 18-inch specimens were cast for the Steelike with bent steel fibers (fiber length of 1.125-inch).

A standard MTS loading frame was used to apply force to the beams via a set of four roller supports, creating a region of constant bending moment in the beam between the inner rollers. To analyze the moment-curvature relationship of the beam, a non-contact measurement system was used to capture deformations along the height of the beam. LEDs were attached to the front face of the beam and an NDI camera tracked their movement throughout the loading process. The change in position of the LEDs was used to calculate the average strain, which in turn was used to calculate curvature of the beam at a given load (and therefore moment). The measured moment-curvature curve was used to estimate the modulus of elasticity, tensile stress-strain curve, and compression stress-strain curve. The test setup is shown in **Figures 77** and **78**, featuring the loading frame, the test specimen with LEDs, and the NDI camera.

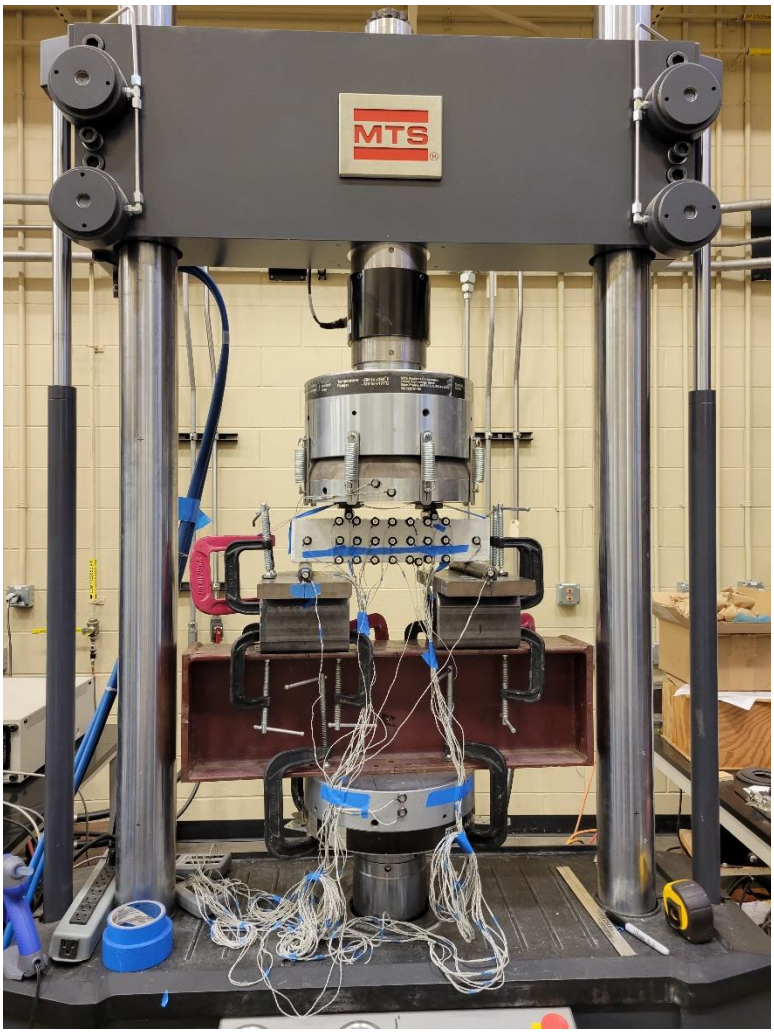

Figure 77: Loading frame for four-point-bending. Beam shown in the loading frame with LEDs attached at multiple locations along the beam.

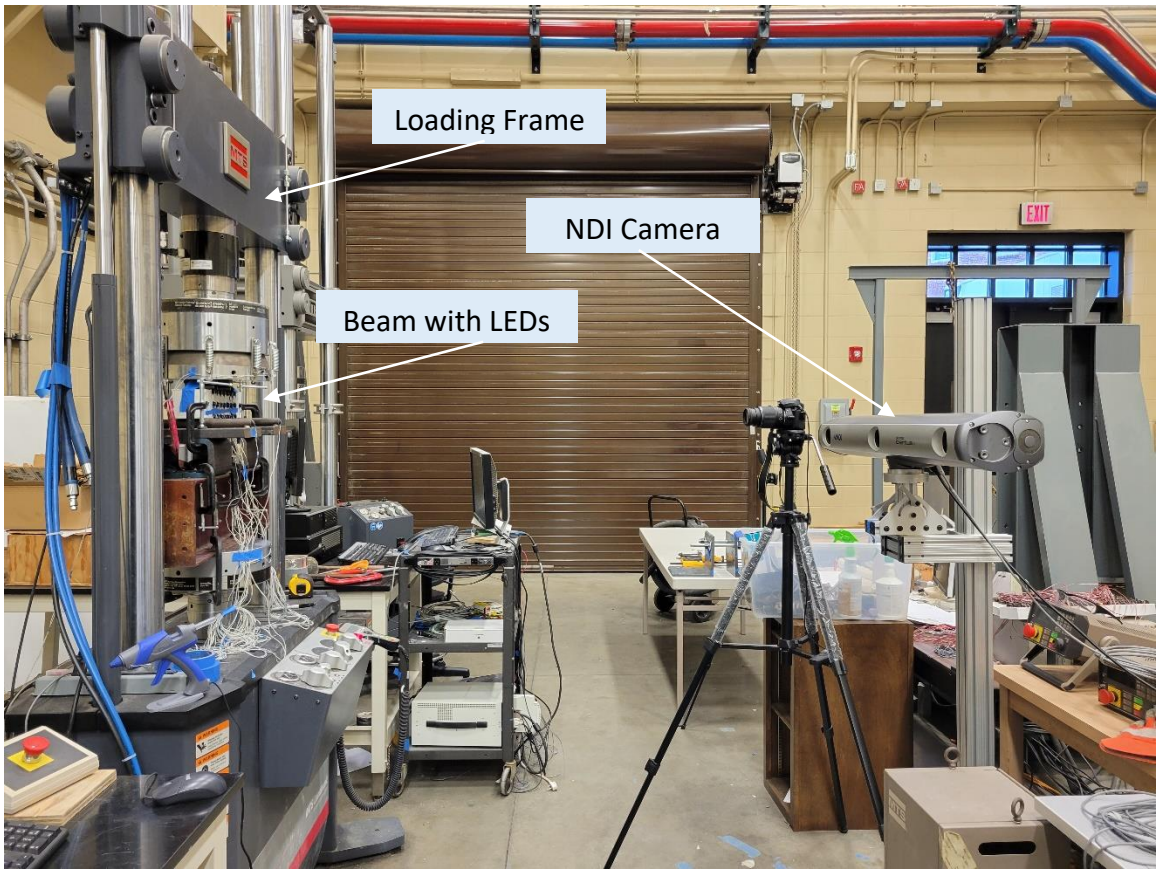

Figure 78: Experimental setup of four-point-bending tests. Loading frame is shown on the left, with the NDI camera on the right.

RESULTS AND DISCUSSION

Impact Testing of UHPFRC Panels

Analysis of the impact testing data attempts to explain the following phenomena: the maximum deflection of each panel and its deflection profile; each panel's dynamic response to determine an appropriate dynamic model; punching shear characteristics in the case of punching shear failure; and a determination of a "passing" or "failing" grade as per ICC/NSSA 500 criteria.

Preliminary panel results

As alluded to in the Experimental Program Chapter, the first two panels (AG_2x12 and AS_2x12) were extremely unsuccessful. Due to the high impact-energy-to-mass-ratio and low fiber content, both panels failed by punching shear and steel reinforcement disengagement. Neither panel will be included in the following discussion, as proper instrumentation was not included, and useful data was not collected. Photos of their impact failures are presented in the impact testing photos appendix.

Displacement-time response and dynamic modeling

Video from the high-speed camera and the Kinovea software were used to track several important measurements. First, the speed of the projectile on its inbound and outbound flights was found by tracking the path of the nose of the projectile and calculating an average velocity.

For inbound flight, the velocity was consistent with the speed displayed by the speed gates during testing; therefore, the researchers were comfortable using the same method to track outbound velocity even without a speed gate measurement to back it up. Second, the duration of impact was determined as the length of time in which the projectile was in contact with the panel. Finally, a single dot at the location of impact was tracked over the course of the entire video to capture the dynamic behavior of the panel after impact. **Figure 79** features examples of key images from the Kinovea analysis of the AS_1.25x12 panel.

Figure 79: Kinovea analysis of projectile motion. Left, tracking the flight path of the incoming projectile and right, tracking the path of the dot at the location of impact as it moves towards its maximum displacement.

The inbound and outbound velocities of each projectile, along with the known mass of the projectile, were used to calculate the impulse given to each panel upon impact. Knowing the duration of the impact, an average impact force could also be calculated. **Equations 2** and **3** were used to calculate impulse and force.

$$J = m\Delta v = m(v_2 - v_1) \tag{2}$$

$$F_{AVG} = \frac{J}{\Delta t} = \frac{m\Delta v}{\Delta t} \tag{3}$$

The displacement-time response of the dot at the impact location of each panel was graphed to observe the deflection of the panel over time. As an example, the displacement-time graph of AS_1.25x12 is shown in **Figure 80**. Clearly, the panel behaved in some sort of dynamically damped manner, as the deflection quickly peaks and then oscillates with lower peaks back toward its initial shape.

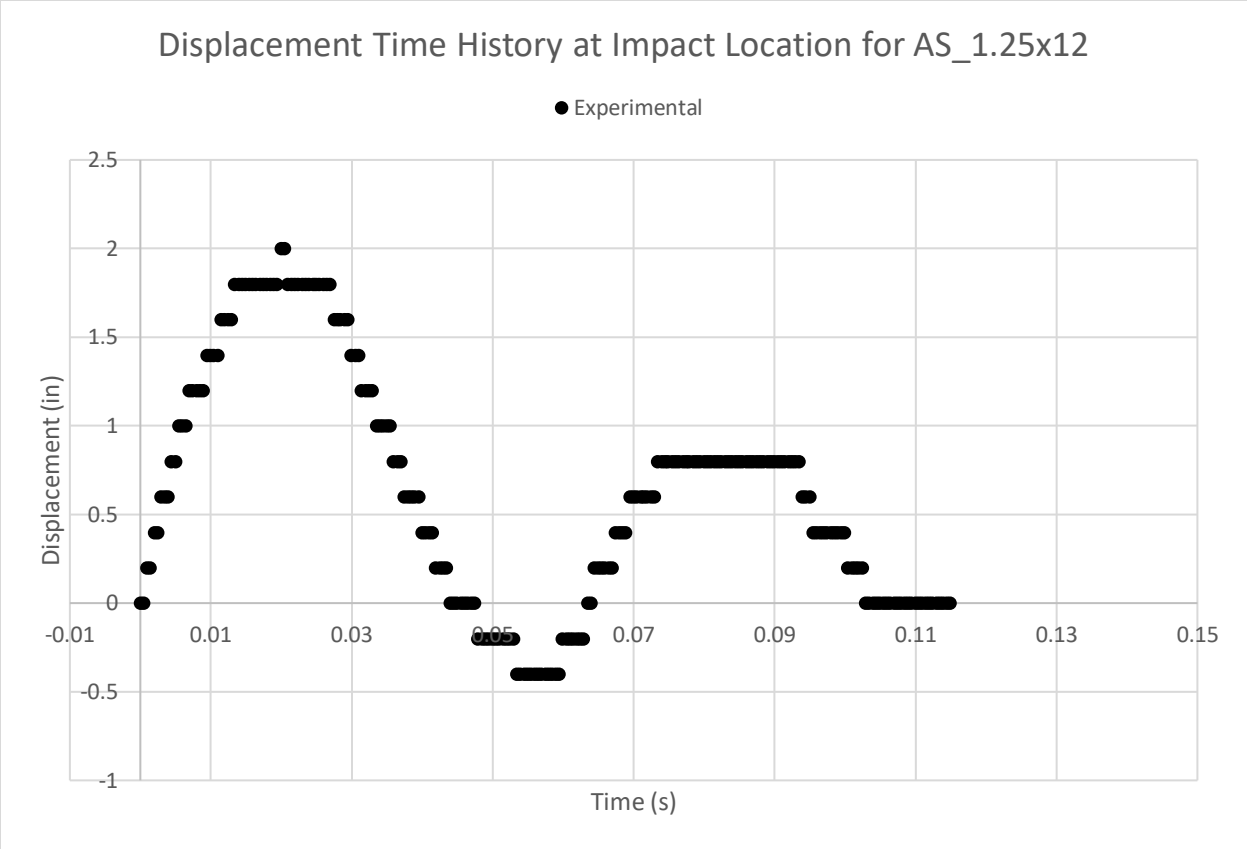

Figure 80: Displacement-time response of panel. Data shown for the AS_1.25x12 panel after impact.

To determine a suitable dynamic model for the panel, the following parameters were needed: stiffness of the panel, damping ratio, and type of impact force. The panel was modeled as a single degree of freedom (SDOF) system with its mass concentrated at the center of the panel at the point of impact. The stiffness would therefore come from the massless "columns" of UHPC above and below the center mass connecting it to the steel frame. Although the researchers assumed the panel was connected in a pinned manner at each end of the panel, a fixed connection was also investigated to find which connection type was more accurate. Simplified models of each connection type and their resulting stiffness equations are shown in **Figure 81**, **Equation 4**, and **Equation 5**. The modulus of elasticity of each panel was determined

from the flexural behavior tests discussed later in **Four-point-bending results**, while the moment of inertia was assumed to be 30% of the full value after cracking.

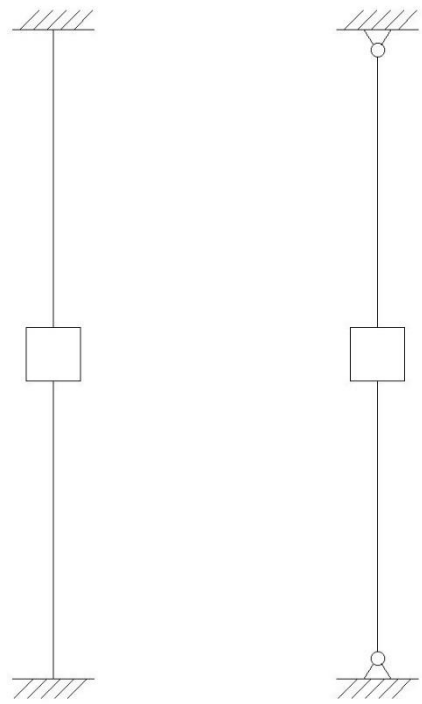

Figure 81: SDOF stiffness models. Idealized dynamic SDOF system with a concentrated mass at the center of the panel for left, a fix-fix connection type and right, a fix-pin connection type.

$$k_{fix-pin} = \frac{3EI}{L^3} \quad per\ column \tag{4}$$

$$k_{fix-fix} = \frac{12EI}{L^3} \quad per\ column \tag{5}$$

The damping ratio was obtained from the displacement-time graph of each panel using **Equation 6** to calculate the rate of decay between adjacent peaks.

$$\zeta \approx \frac{\ln\left(\frac{u_P}{u_{p+n}}\right)}{2\pi n} \tag{6}$$

Finally, two types of impact loads were chosen to represent the behavior of the projectile striking the panel. The first was a unit impulse load, characterized by a large force acting over an infinitesimally small duration of time whose area under the curve results in one unit of impulse. When the impulse imparted on a structure is something other than one, the response can be multiplied by the magnitude of the actual impulse to determine the appropriate displacement response. The second type of impact load is a rectangular pulse load, characterized by a constant force acting over a given duration of time that loads and unloads instantaneously. Given that the impact duration of each test ranged between 0.03 and 0.05 seconds, the researchers believed either impact type are reasonable approximations of the expected loading. The displacement response equations for each type of impact load are given in **Equations 7** and **8** (Chopra, 2007).

$$u_{unit\ impulse} = \frac{J_o}{M\omega_d} e^{-\zeta\omega_n t} \sin(\omega_d t)\ , t > 0 \tag{7}$$

$$u_{rectangular} = \frac{p_o}{k}\left[1 - \frac{1}{\sqrt{1-\zeta^2}} e^{-\zeta\omega_n t} \cos\left(\omega_d t - \arctan\left(\frac{\zeta\omega_n}{\omega_d}\right)\right)\right], 0 < t < t_d$$

$$u_{rectangular} = \frac{p_o e^{-\zeta\omega_n t}}{k\sqrt{1-\zeta^2}}\left[e^{\zeta\omega_n t_d} \cos\left(\omega_d(t-t_d) - \arctan\left(\frac{\zeta\omega_n}{\omega_d}\right)\right) - \cos\left(\omega_d t - arctan\left(\frac{\zeta\omega_n}{\omega_d}\right)\right)\right], t > t_d \tag{8}$$

Models with the following combinations were graphed on top of the experimental displacement-time curve of AS_1.25x12: a unit impulse with fix-pin stiffness; a rectangular pulse with fix-pin stiffness; a unit impulse with fix-fix stiffness; and a rectangular pulse with fix-fix stiffness. The results, shown in **Figure 82**, suggest that a unit impulse with a fix-fix stiffness is the most appropriate model for the AS_1.25x12 experimental impact data. Using a fix-fix stiffness with a unit impulse load also reasonably predicted the behavior of all other panels, suggesting that fix-fix stiffness with a unit impulse was indeed the most appropriate model for the experimental setup. Results from five other panels are shown in **Figure 83**. AS_1.625x24 is not included in the dynamic analysis as it failed by punching shear and will be discussed in the punching shear failure section.

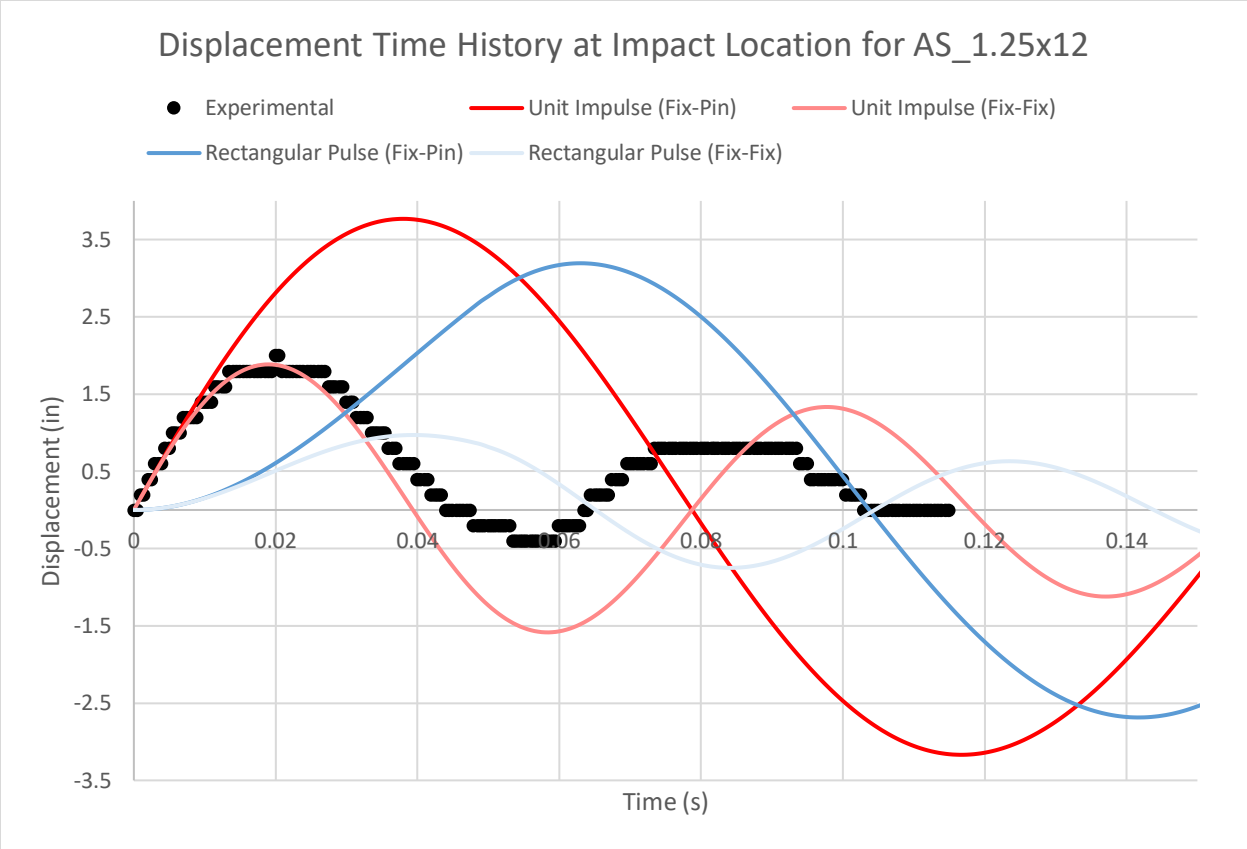

Figure 82: Comparison of dynamic models. Using AS_1.25x12 experimental data as the target displacement-time behavior, various pulse types and stiffness models are compared.

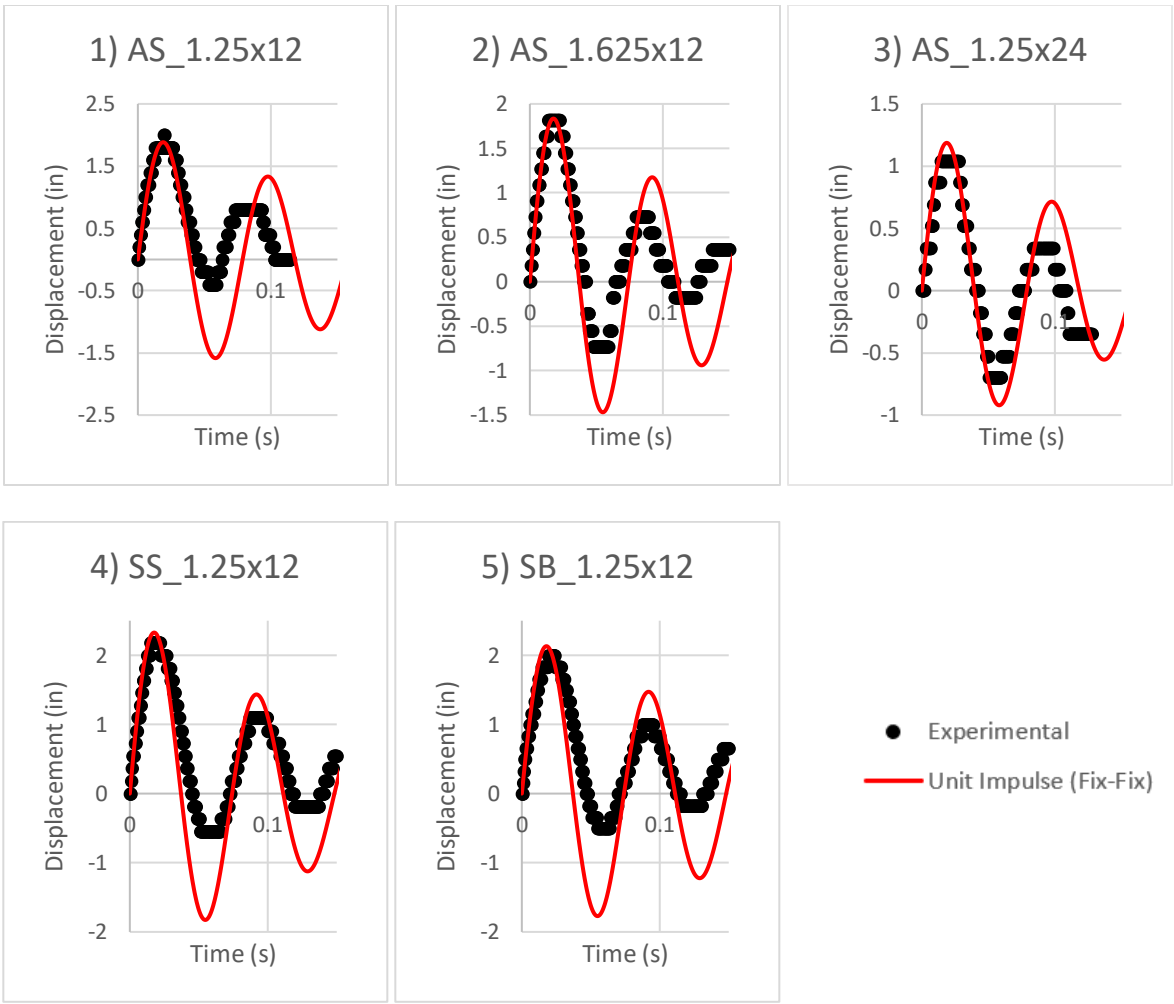

Figure 83: Experimental displacement-time histories versus dynamic model. Experimental data is compared to a fix-fix stiffness, unit impulse dynamic model for 1) AS_1.25x12, 2) AS_1.625x12, 3) AS_1.25x24, 4) SS_1.25x12, and 5) SB_1.25x12.

The dynamic models all reasonably predict the first peak immediately after impact; however, the models become less accurate throughout the duration of the panel's motion. In the panels cast with Aalborg Extreme and straight steel fibers (AS_1.25x12, AS_1.625x12, and AS_1.25x24) the period of the experimental data appears to shrink over time, leaving the model to lag behind the experimental curve. The problem is much less pronounced in the panels that used Steelike (SS_1.25x12 and SB_1.25x12) regardless of fiber type. The period of the dynamic model is determined by the trigonometric term in **Equation 7** such that changing the damped

frequency of the panel would change the period of oscillation. Damped frequency is described in **Equation 9**. A shrinking period from the experimental data would require a larger natural frequency, which could be achieved by increasing natural frequency or decreasing the damping ratio; natural frequency could be increased by decreasing mass or increasing stiffness. The damage done to the panel by its maximum initial deflection clearly changes the way the panel moves. More experimental tests could be done to understand how the dynamic model might change over time to better predict the motion.

$$\omega_d = \omega_n\sqrt{1-\zeta^2}\ ;\ \ \omega_n = \sqrt{\frac{k}{M}} \tag{9}$$

A second limitation of the dynamic models is the lack of accuracy when predicting negative or rebound deflections. For all panels except AS_1.25x24, the model severely over-predicts the rebounding deflection after the initial peak. This may be caused by the slight change in boundary conditions as the panel deflects to the left or to the right. The clamps used to attach each panel to the steel frame seems to provide more resistance as the panel moves outward (to the right) during the rebound than when it moves inward (to the left) during the impact.

Profile of maximum deflection

Another application of the high-speed videos and Kinovea software was to determine the profile of the panel and its maximum deflection, with the goal of modeling its shape and comparing its maximum deflection with the expected maximum from the impact force. The position of every dot along the side of the panel was recorded at the time of maximum panel

displacement to build a deflected shape for each impact. **Figure 84** shows an example of AS_1.25x12's deflected shape in Kinovea, as well as its actual deflection graphed next to an expected deflection shape. Based on the dynamic modeling analysis, a fix-fix connection is the correct support condition for the panel. The expected deflection is therefore based on a fix-fix connection type with a center point load. The equation for the deflected shape is given in **Equation 10**. The force used in the calculations was the average impact load calculated from **Equation 3**.

$$\Delta(y) = \frac{F_{AVG} y^2}{48EI}(3L - 3y) \tag{10}$$

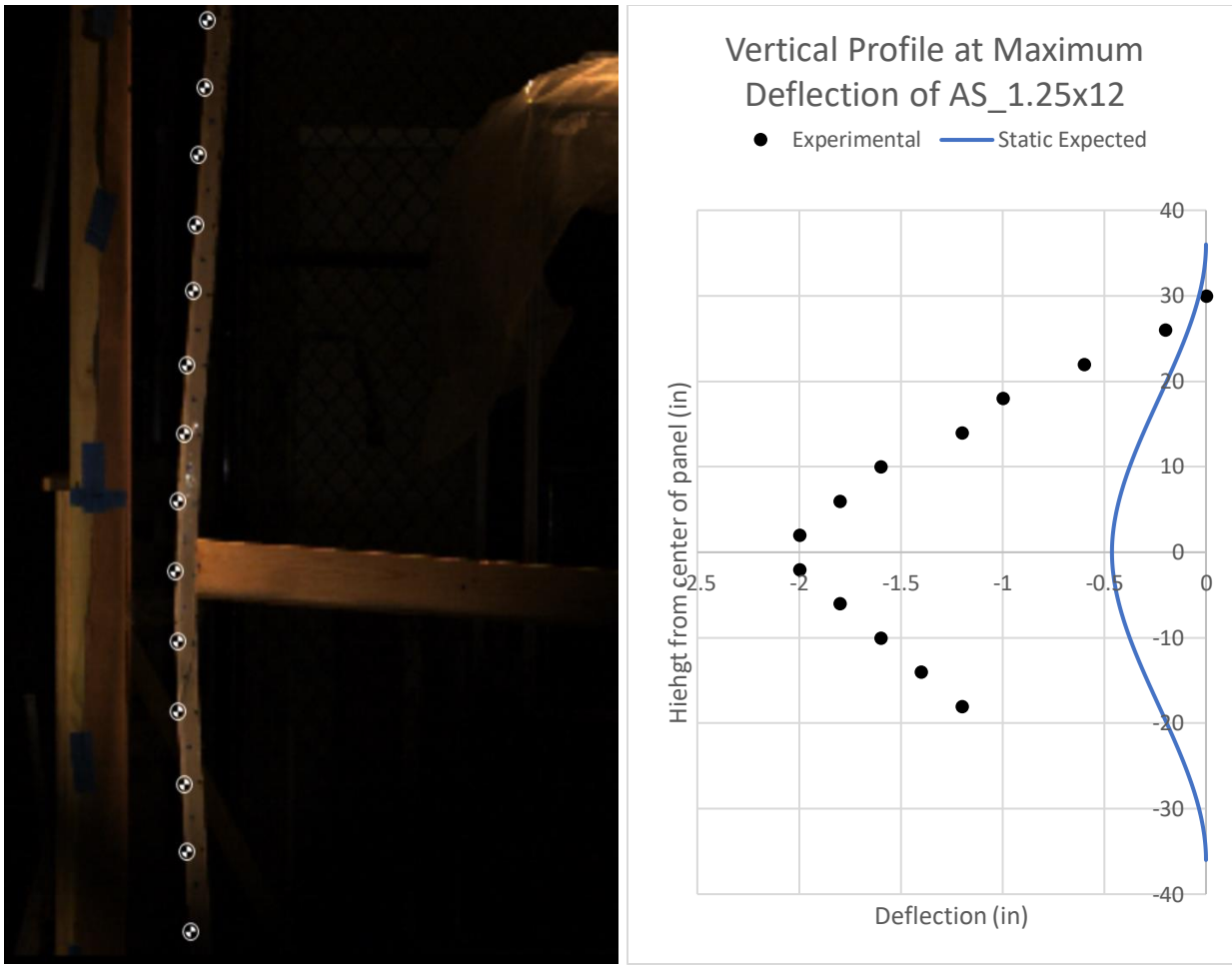

Figure 84: Kinovea analysis of maximum deflection profile. Left, deflected shape of AS_1.25x12 from Kinovea and right, experimental deflection compared with expected deflection for the average impact force.

Clearly, the expected deflection is much smaller than the actual deflection experienced by the panel. A dynamic amplification factor (DAF) can explain this difference. DAFs are used to correct for the difference between the average impact load and the peak impact load. A unit impulse load does not actually impart the same amount of force throughout the duration of impact, but instead starts smaller and builds to a peak impact force before dropping back to zero at the end of the impact. Using the average impact load in **Equation 3** therefore underestimates the maximum deflection because it is based on the smaller average impact load rather than the

larger peak impact load. Multiplying the average impact load with the correct DAF will more correctly predict the maximum deflected profile. **Figure 85** shows the experimental deflection of all five panels compared with the average load expected deflection and the increased peak load expected deflection. All the 12-inch panels' deflections are correctly predicted using a DAF between 3.7 and 4.3, suggesting that the impulse load from the 2x4 projectile has a DAF of approximately 4 for the 12-inch-wide panels. For the 24-inch panel, a DAF of 2.5 is more appropriate. The close correlation between the experimental data and the shape of the expected deflection also reinforced that the panels experienced a fix-fix connection type. The graph of AS_1.625x24 is not included because it failed by punching shear and did not deflect in the same manner as the other panels.

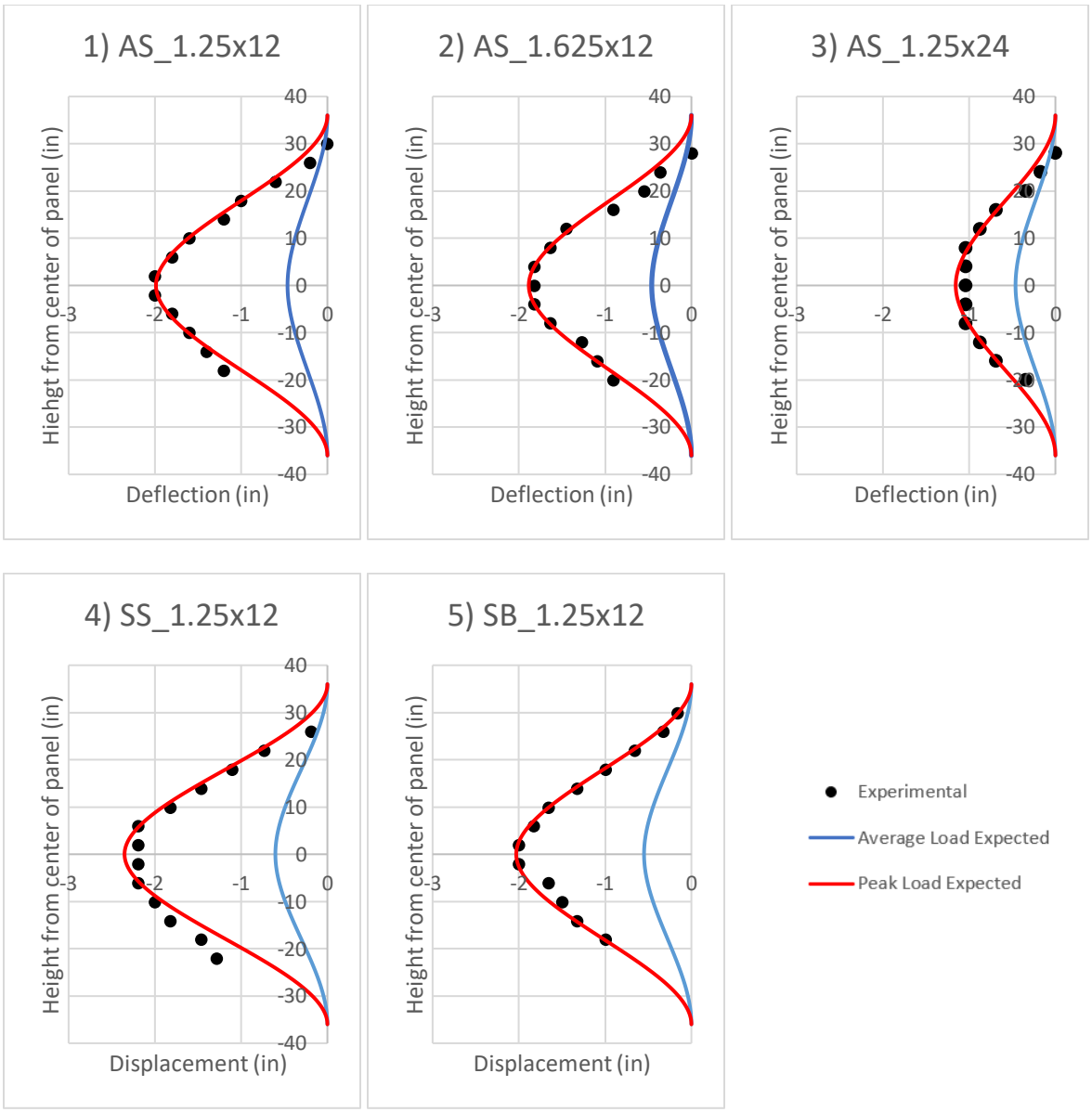

Figure 85: Experimental deflection profile versus beam-point-load models. Maximum deflected profiles compared with expected deflections from average and peak impact forces for 1) AS_1.25x12 with DAF=4.3, 2) AS_1.625x12 with DAF=4.1, 3) AS_1.25x24 with DAF=2.5, 4) SS_1.25x12 with DAF=3.9, and 5) SB_1.25x12 with DAF=3.7.

A few comparisons can be made about the maximum deflected profiles of each panel. First, AS_1.625x12 deflected slightly less than AS_1.25x12, which correlates with its larger thickness and therefore higher stiffness. AS_1.25x12 deflected twice as much as AS_1.25x24, which corresponds to AS_1.25x12 being half as stiff as AS_1.25x24. AS_1.25x12 and

SS_1.25x12 deflected similarly, with SS_1.25x12 deflecting slightly more. This suggests Aalborg Extreme is a stiffer mix than Steelike, which is supported by the consistency of each UHPC during casting. Finally, SB_1.25x12 deflected slightly less than SS_1.25x12, suggesting that the longer bent fibers provided more stiffness than the shorter straight fibers.

Punching shear failure

One panel, AS_1.625x24, failed by punching shear. Unlike the other panels that experienced major flexural deflection, AS_1.625x24 did not deflect and oscillate. Instead, it failed immediately when the 2x4 projectile punched a hole through the panel. Using **Equation 3**, the impact force from the projectile was calculated as 15,285 lbf.

ACI 318 provides an equation to calculate the punching shear capacity of concrete, but it relies on a failure mechanism shown in **Figure 86** where the punched-out concrete extends at a 45° angle from the projectile's cross section. The mechanism of punching shear capacity in UHPC is less understood than normal strength concrete, so the first step of the punching shear analysis was to demonstrate that the punching shear failure in AS_1.625x24 formed the correct 45° shape. **Figure 87** shows the front and back of the tested panel. The anticipated 45° shape was achieved on the back face of the panel, confirming that ACI 318's equations could be used.

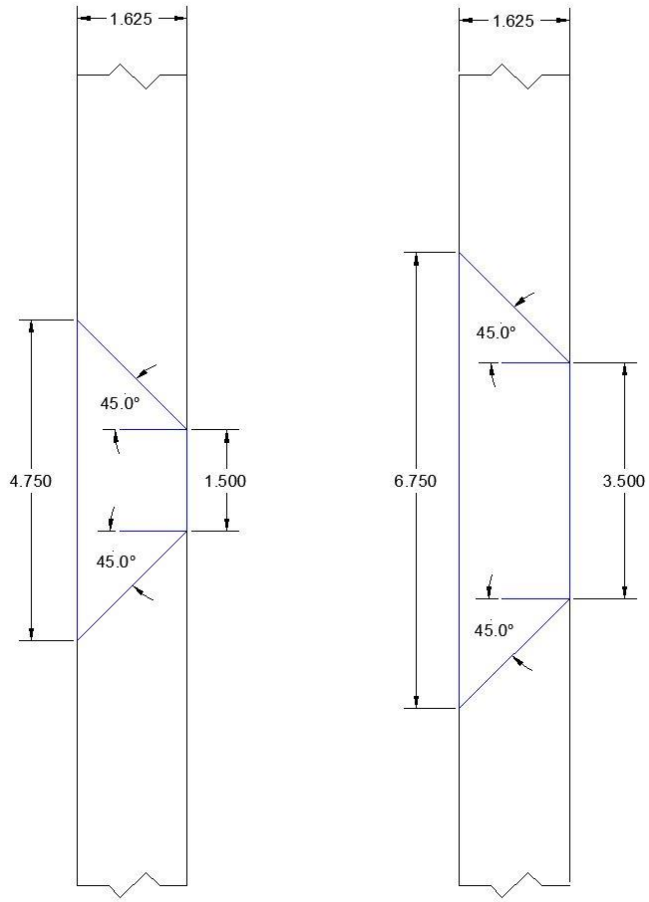

Figure 86: Punching shear failure mechanism. Idealized failure of a concrete slab due to punching shear. Left, a top view using the 1.5-inch side of the 2x4 projectile and right, a side view using the 3.5-inch side of the projectile. Specific measurements for the anticipated failure of a 1.625-inch-thick panel are included in the drawings. Values are shown in inches.

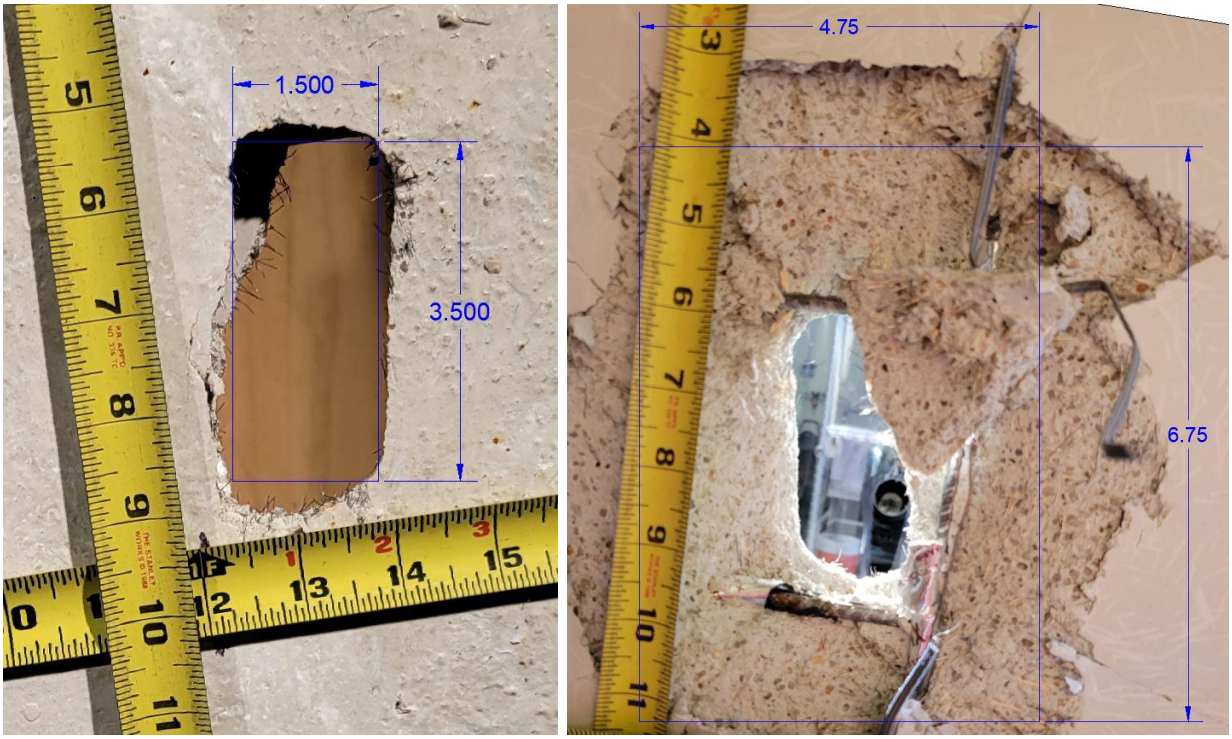

Figure 87: Punching shear failure of panel. Actual failure of the AS_1.624x24 panel. Left, front-face dimensions of the 2x4 projectile; right, back-face shear failure of the UHPC. The shape and dimensions of the back-face failure are consistent with the expected failure mechanism. Values are shown in inches.

Two additional equations from Harris (2005) were also used to predict the failure strength of UHPC as these two equations were modified to better explain the punching shear failure of UHPC panels. The results from Harris (2005) show that the original ACI 318 equation under-predicts the capacity, while the tensile-based equation over-predicts the capacity. The modified ACI 318 equation presented at the end of Harris (2005) best predicts the punching shear strength of UHPC. All three equations are presented as **Equations 11**, **12**, and **13**, respectively. The results from Harris (2005) are consistent with the results from this study, whereby the modified ACI 318 equation best predicted the shear strength of AS_1.625x24.

$$V_{ACI} = 4\sqrt{f'_c}b_o d \tag{11}$$

$$V_{tensile} = (f_t + f_{t,crack})b_o h \tag{12}$$

$$V_{ACI,modified} = 4\sqrt{f'_c}b_o h \tag{13}$$

Figure 88: Comparison of punching shear capacity equations. Calculations based on AS_1.625x24 panel.

Equation	***Results (lbf)***
Original ACI 318 (11)	6,992
Tensile based (21)	65,053
Modified ACI 318 (13)	13,984
Experimental Force	15,285

Reversing the calculation from **Equation 13** using the actual force from the experiment, the minimum panel thickness needed to resist the projectile would be around 1.75 inches.

Pass/fail analysis

ICC/NSSA 500 provides three qualifications to pass a missile impact test: no perforation of the interior surface of the panel; no dislodgement of any component and no excessive spall will be ejected from the panel such that the witness screen is punctured; and permanent deformation of less than three inches. **Figure 89** summarizes the performance of each panel and its pass/fail designation. Photos of each panel and witness screen after impact can be found in the impact testing photos appendix.

Figure 89: Pass/fail analysis of each panel. Summary of each panel's performance under impact.

Panel	***Interior perforation?***	***Witness screen perforation?***	***Maximum deformation (in)***	***Permanent deformation (in)***	***Pass/Fail?***
AS_1.25x12	No	No	2.0	0.0	Pass
AS_1.625x12	No	No	1.8	0.2	Pass
AS_1.25x24	No	No	1.0	0.0	Pass
AS_1.625x24	Yes	Yes	N/A	N/A	Fail
SS_1.25x12	No	No	2.2	0.3	Pass
SB_1.25x12	No	No	2.0	0.3	Pass

Material Properties Testing Results

Results from compressive and flexural tests are presented in the next two sections. Material properties from these tests, such as compressive strength, modulus of elasticity, and tensile strength, were used in the analyses above.

Compressive testing results

The compressive strengths from the cubes poured from the same mix as each panel are shown in **Figure 90**. The average compressive strength from each batch was used when needed in a calculation about impact performance.

Figure 90: Compression testing results. Compressive strengths of UHPC mixes corresponding to each panel.

Specimen Name	***Individual Cube Strengths (ksi)***	***Average Strength (ksi)***
AS_1.25x12	19.2 17.5 15.6	17.4
AS_1.625x12	19.9 16.7 18.3 19.0 18.1	18.4
AS_1.25x24	16.0 16.0 16.0	16.0
AS_1.625x24	14.8 15.1 14.6	14.8
SS_1.25x12	19.1 23.8	21.5
SB_1.25x12	20.4 21.6 20.0 20.8	20.7

Four-point-bending results

Moment of elasticity was calculated for each four-point-bending specimen by using the deflection of the beam at center span and the associated force that caused that deflection. Because the moment of inertia, deflection, force, and location along the beam were known, **Equation 10** was used to back calculate the modulus of elasticity. The compressive strength for each mix type was taken from the averages in **Figure 90**.

The moment-curvature relationship of each beam was graphed, then compared with a moment-curvature graph calculated from a given tensile stress-strain and compressive stress-

strain curve. The parameters of the tensile stress-strain curve were adjusted until the calculated graph lined up with the experimental graph. Once the ideal and experimental graphs matched, the researchers knew the correct tensile stress-strain curve had been found. The tensile stress-strain curve was then used for previously presented analyses on punching shear strength. **Figures 91** through **93** show the moment-curvature, tensile stress-strain, and compressive stress-strain for each beam. "AS" specimens are Aalborg Extreme with straight steel fibers; "SS" specimens are Steelike with straight steel fibers; and "SB" specimens are Steelike with bent steel fibers.

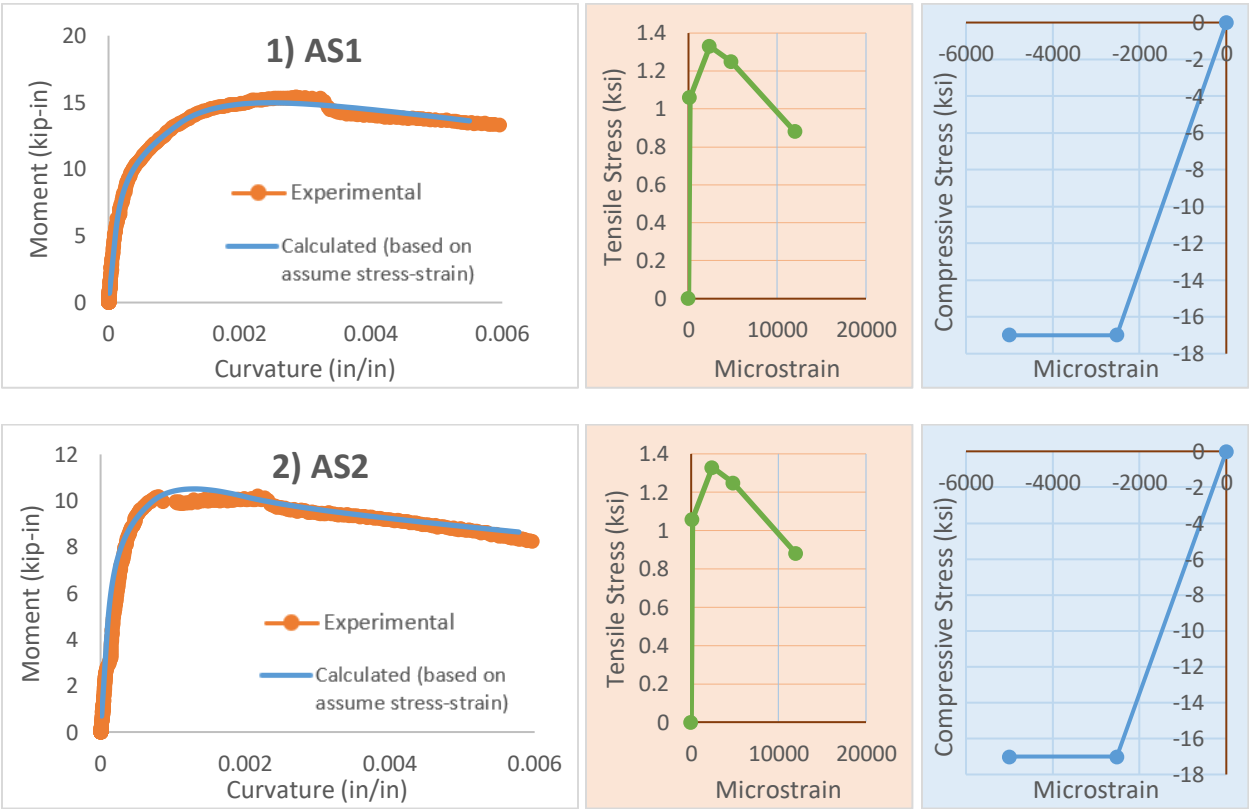

Figure 91: Four-point-bending results for AS1 and AS2. Left to right for each specimen, moment-curvature graphs, tensile stress-strain behavior, and compressive stress-strain behavior.

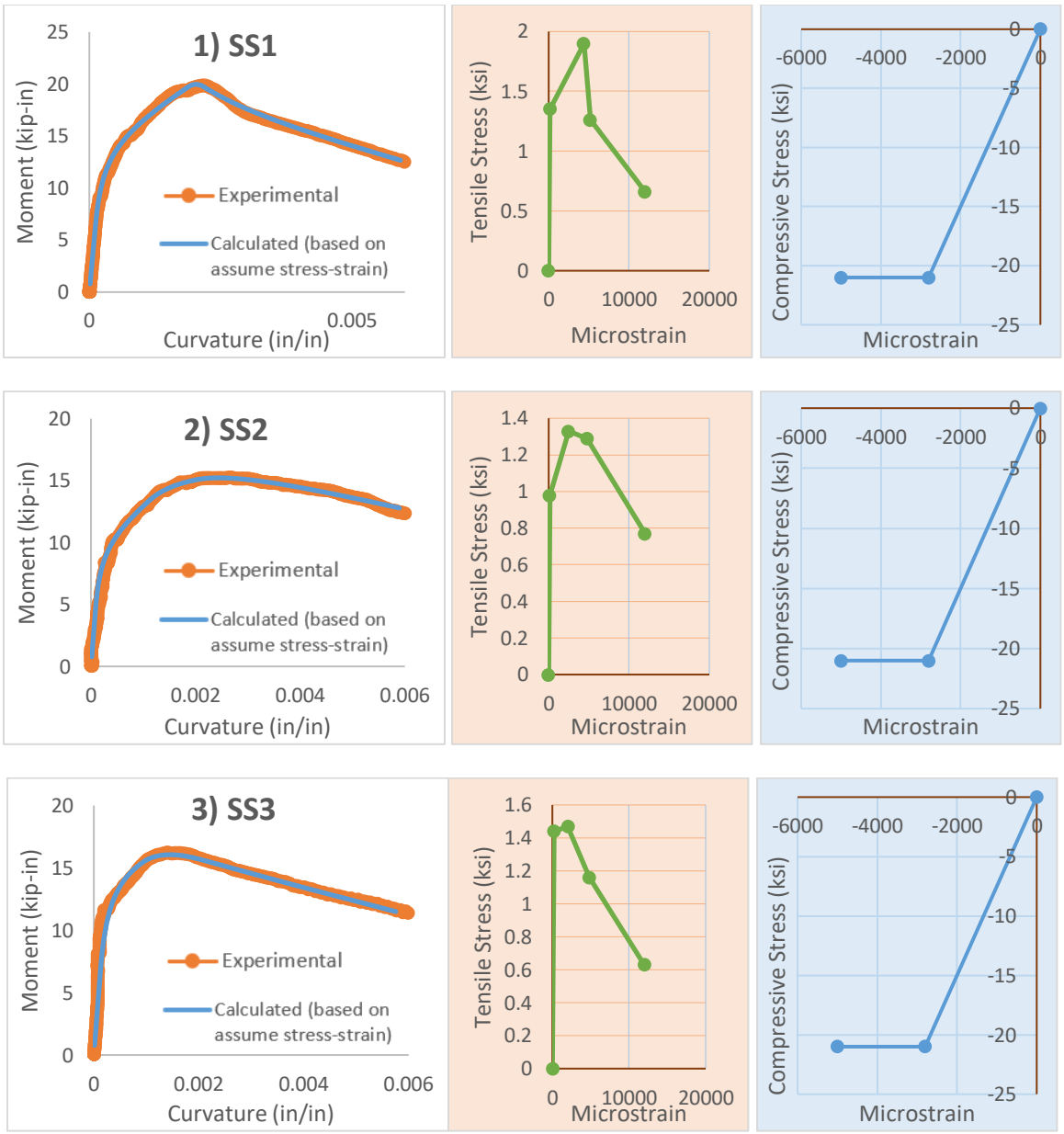

Figure 92: Four-point-bending results for SS1, SS2, and SS3. Left to right for each specimen, moment-curvature graphs, tensile stress-strain behavior, and compressive stress-strain behavior.

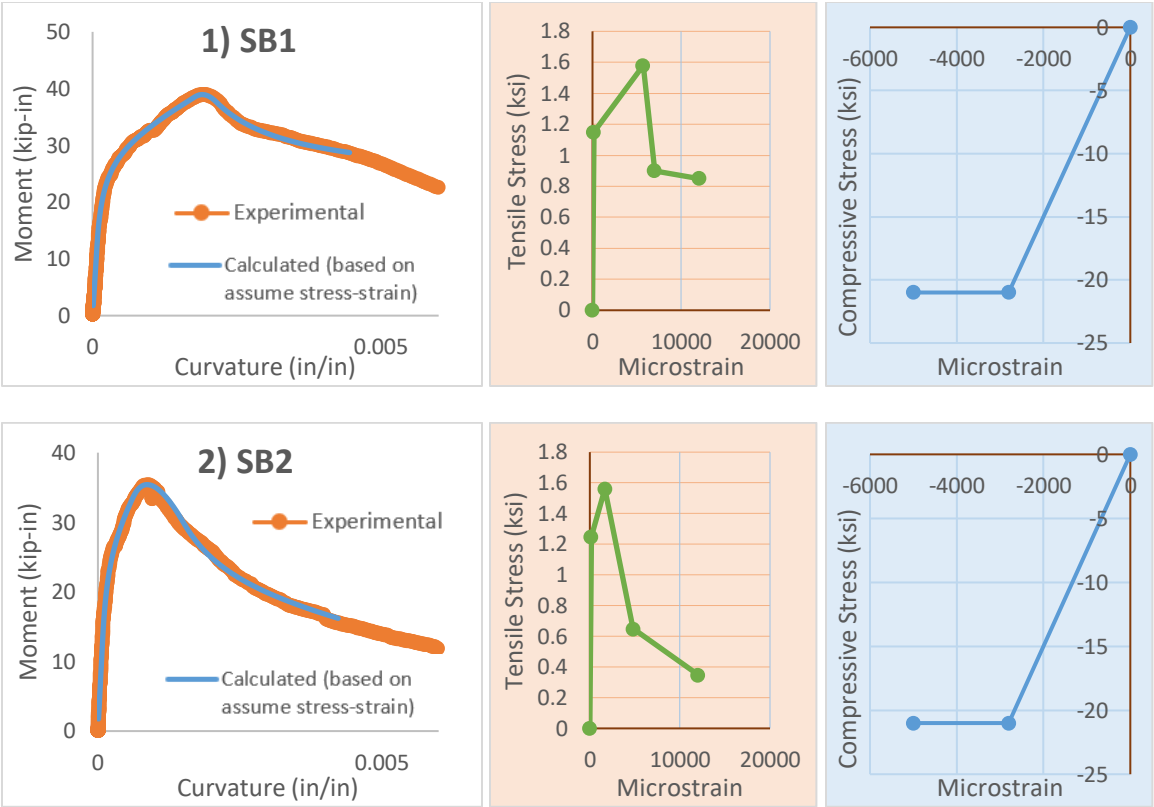

Figure 93: Four-point-bending results for SB1 and SB2. Left to right for each specimen, moment-curvature graphs, tensile stress-strain behavior, and compressive stress-strain behavior.

CONCLUSIONS

Experimental Conclusions

Based on the results presented in the previous chapter, several conclusions about the behavior of ultra-high-performance fiber reinforced concrete under tornado-debris-like impact loads can be made. First, the dynamic response of UHPFRC panels clamped to a strong structure such as the steel frame used in this study can be modeled accurately using a beam with fixed end boundary conditions and with mass concentrated at the center of the span. The force imparted by the 2x4 projectile is best modeled as a unit impulse load scaled up to reflect the magnitude of the change in momentum of the projectile. Although the model loses accuracy over the duration of the panels' motions due to a change in stiffness once the panel is damaged, the model correctly predicts the time and magnitude of the maximum deflection. The maximum deflection is the most important measure of a tornado shelter's success and therefore the most important part of the dynamic model.

Second, the deflection profile of the UHPFRC panels can be accurately modeled as a beam with fix-fix boundary conditions and a concentrated load at the center of the beam. The common deflection equation for a fix-fix beam gives an accurate shape but a diminished magnitude when used with the average impact force. Multiplying the magnitude with a dynamic amplification factor to obtain the correct maximum magnitude gives a prediction of the peak impact force that panel actually experiences during impact, reinforcing the idea that the projectile imparts an impulse that changes over the course of the impact rather than a rectangular pulse with constant magnitude.

The effect of UHPC and fiber type seemed to have a small impact on the performance of the panels. The stiffer Aalborg Extreme mix slightly outperformed the more flowable Steelike mix, while the longer bent steel fibers slightly outperformed the shorter straight steel fibers. Using a combination of the two fibers may prove to be the best option, as previous research suggests that mixing different sized fibers improves crack-bridging capabilities.

For AS_1.625x24, the only panel impacted at full speed according to ICC/NSSA 500 standards, punching shear rather than bending was the controlling failure mechanism. AS_1.625x24 was the stiffest panel investigated in the study; increasing the flexural stiffness may have encouraged the panel to fail from punching shear rather than excessive deflection, as a higher flexural stiffness reduces overall deflection. Increasing the thickness to 1.75 inches, as mentioned in the punching shear section, would further increase the stiffness, therefore reducing deflection which may result in punching shear failure. Contrary to a traditional design approach that recommends increasing the size of the specimen to avoid failure, decreasing the thickness of the UHPC panels may actually allow the panel to avoid punching shear failure (the more dangerous and unacceptable failure mode) by allowing the panel to deflect (the more acceptable failure mode). A critical thickness between 1.25 inches and 1.625 inches that would deflect enough to avoid punching shear failure but not enough to deflect more than the allowable 5-inch witness screen limit should be investigated in future UHPC panels tested under tornado simulation conditions. Although no panel tested in this study passed ICC/NSSA 500 standards under a full-speed, 15 lb, 2x4 projectile, important lessons were learned about UHPFRC panel performance under impact loads. A full-sized 4 ft by 6 ft panel between 1.25 and 1.625 inches thick might be best suited to resist tornado debris impact, both in terms of punching shear and flexural stiffness requirements.

Applications and Discussion

The results of this study show UHPFRC as a promising material for future tornado shelter design. Based on the recommended 1.25 inch to 1.625 inch panel, UHPFRC tornado shelters could be less than half the thickness of most conventional normal strength concrete shelters. Significantly decreasing the size and weight of a tornado shelter opens the door to many future applications.

For a 5-person, 4 ft by 4 ft by 6 ft tornado shelter with 2-inch-thick panels, approximately 19 cubic feet of UHPFRC and 112 square feet of steel reinforcing wire mesh would be needed. Some estimates suggest that UHPFRC can be produced for between $600 and $850 per cubic yard; welded wire mesh costs about $1.50 per square foot (Wille, 2013; Tadros et al., 2019; and Grainger, n.d.). Taking the higher end of the estimate, the panels of the tornado shelter could be manufactured for about $765. Including the necessary hardware and installations costs will undoubtedly increase the price; however, even increasing the price fivefold would keep a potential UHPFRC shelter competitive with existing tornado shelter options. **Figure 94** is re-presented with the price of a potential 5-person UHPFRC shelter as $3,825, showing that it is still below market price of other shelter options.

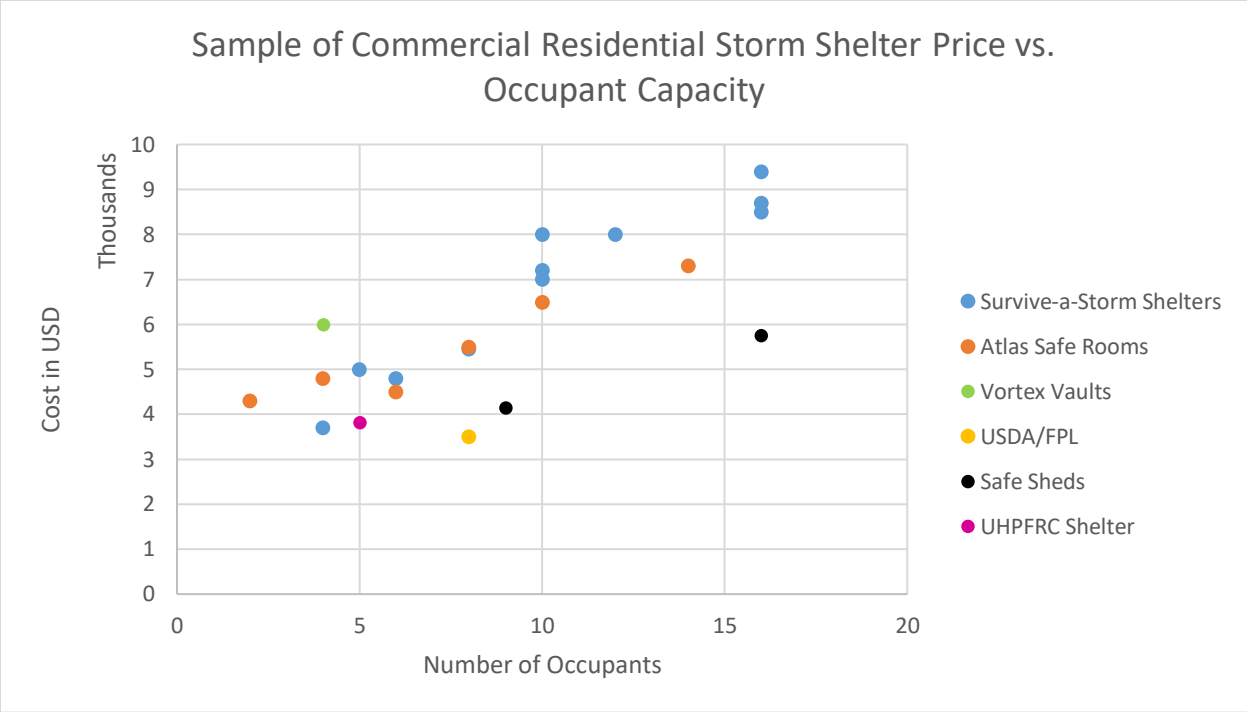

Figure 94: Price versus occupancy of tornado shelters, including proposed UHPFRC shelter.

A traditional stand-alone tornado shelter would clearly be a viable option. More interesting applications for UHPFRC tornado resistant building components may also be possible. UHPC countertops and side panels could make a kitchen island double as a tornado shelter, while decoratively imprinted UHPC walls could turn entire rooms or houses into tornado resistant structures. As ultra-high-performance concrete continues to grow in popularity throughout the United States, its versatility and unique casting options could make integrating tornado resistant panels into residential structures very easy. The more accessible a tornado resistant space is to the people who need shelter, the more likely it is that they will use it. UHPFRC panels have the potential to save lives by making tornado shelters extremely accessible.

Further Studies

To gain further knowledge about ultra-high-performance fiber reinforced concrete panels under tornado-debris-like impact loads, the following future studies are proposed:

- The effect of cracking damage after impact on the stiffness and damping ratio of the panels' dynamic motion should be studied to improve predictive dynamic models.
- Replicating similar impacts on panels that include load cells between the panel and the steel frame (or other strong support) would give more detailed information about the amount of force felt by the panel throughout the duration of the impact. By knowing the actual peak force imparted by the projectile, the maximum deflection of the panel can be compared with the expected deflection from the peak force.
- Panels with a mixture of short and long fibers should be studied and compared with panels having only one or the other to determine the optimal type of fiber to include in UHPFRC panels meant to withstand impact.
- "Full-size" panels (defined in this study as 4 ft by 6 ft dimensions) between 1.25 and 1.625 inches thick should be constructed and tested to determine if the punching shear and flexural behavior of the panels observed in this study are scalable.

REFERENCES

AALBORG EXTREME™ ULTRA HIGH PERFORMANCE CONCRETE. Lehigh White Cement. (n.d.). https://www.lehighwhitecement.com/aalborg-extreme-ultra-high-performance-concrete/.

Aguilar, C. (2014, October 13). *Fondation Louis Vuitton / Gehry Partners*. ArchDaily. https://www.archdaily.com/555694/fondation-louis-vuitton-gehry-partners.

American Concrete Institute. (2019). 318-19 Building Code Requirements for Structural Concrete

American Society of Civil Engineers. (2010). Minimum Design Loads for Buildings and Other Structures

Architizer. (2014, February 20). *Jean Bouin Stadium by Trust In Design*. Architizer. https://architizer.com/projects/jean-bouin-stadium/.

ASTM International. (2017). C1856/C1856M-17 Standard Practice for Fabricating and Testing Specimens of Ultra-High Performance Concrete. Retrieved from https://doi-org.libdata.lib.ua.edu/10.1520/C1856_C1856M-17

ASTM International. (2019). C1609/C1609M-19a Standard Test Method for Flexural Performance of Fiber-Reinforced Concrete (Using Beam With Third-Point Loading). Retrieved from https://doi-org.libdata.lib.ua.edu/10.1520/C1609_C1609M-19A

ASTM International. (2021). C39/C39M-21 Standard Test Method for Compressive Strength of Cylindrical Concrete Specimens. Retrieved from https://doi-org.libdata.lib.ua.edu/10.1520/C0039_C0039M-21

Atlas Safe Rooms. (n.d.). *Residential Storm Shelters Options & Pricing*. Atlas Safe Rooms. https://atlassaferooms.com/safe-rooms/.

Azmee, N. M., & Shafiq, N. (2018). Ultra-high performance concrete: From fundamental to applications. *Case Studies in Construction Materials*, *9*. https://doi.org/10.1016/j.cscm.2018.e00197

Bekaert. (n.d.). *Steel wire transformation and coatings*. Bekaert. https://www.bekaert.com/.

Beppu, M., Kataoka, S., Ichino, H., & Musha, H. (2020). Failure characteristics of UHPFRC panels subjected to projectile impact. *Composites Part B: Engineering*, *182*, 107505. https://doi.org/10.1016/j.compositesb.2019.107505

Bischoff, P. H., Perry, S. H., & Eibl, J. (1990). Contact force calculations with a simple spring-mass model for hard impact: A case study using polystyrene aggregate concrete. *International Journal of Impact Engineering*, *9*(3), 317–325. https://doi.org/10.1016/0734-743x(90)90005-g

Centers for Disease Control and Prevention. (2021, March 29). *Staying Safe in a Tornado*. CDC: Environmental Health. https://www.cdc.gov/nceh/features/tornadosafety/index.html.

Chang, W. S. (1981). Impact of Solid Missiles on Concrete Barriers. *Journal of the Structural Division*, *107*(2), 257–271. https://doi.org/10.1061/jsdeag.0005640

Charmant, J. (n.d.). Kinovea. https://www.kinovea.org/.

CW Staff. (2021, March 18). *'Dixieland Delight' and Few Masks in Sight: Reflections on sheltering at peak capacity*. The Crimson White. https://cw.ua.edu/81069/news/dixieland-delight-and-few-masks-in-sight-reflections-on-sheltering-at-peak-capacity/#photo.

Environment Analyst. (2018). *Cross laminated timber market to grow 15% by 2025, says report*. Environment Analyst UK. https://environment-analyst.com/register?o=70377&productID=8&layout=main.

Falk, R. H., Bridwell, J. J., Williamson, T., & Black, T. (2019). Development of a ready-to-assemble tornado shelter from cross-laminated timber (CLT): impact and wind pressure testing. https://doi.org/10.2737/fpl-gtr-266

Federal Highway Administration. (2019). *North American Deployments of UHPC in Highway Bridge Construction*. Deployments. https://highways.dot.gov/research/structures/ultra-high-performance-concrete/deployments.

Fujikake, K., Senga, T., Ueda, N., Ohno, T., & Katagiri, M. (2006, March 8). *Effects of Strain Rate on Tensile Behavior of Reactive Powder Concrete*. Journal of Advanced Concrete Technology. https://www.jstage.jst.go.jp/article/jact/4/1/4_1_79/_article.

Gagan, J. P., Gerard, A., & Gordon, J. (2010). A Historical and Statistical Comparison of "Tornado Alley" to "Dixie Alley". *National Weather Digest*, *34*(2), 145–155.

Grainger. (n.d.). *Mesh, 1/4", 4 ft. W, Black*. Grainger Products. https://www.grainger.com/product/DIRECT-METALS-Mesh-38MH33.

Habel, K., & Gauvreau, P. (2008). Response of ultra-high performance fiber reinforced concrete (UHPFRC) to impact and static loading. *Cement and Concrete Composites*, *30*(10), 938–946. https://doi.org/10.1016/j.cemconcomp.2008.09.001

Harbor Enterprises. (2021, February 23). *Residential Storm Shelters*. Survive-a-Storm Shelters. https://survive-a-storm.com/residential-storm-shelters/.

Harris, D. K., & Roberts-Wollmann. (2005). (rep.). *Characterization of the punching shear capacity of thin ultra-high performance concrete slabs* (pp. 1–64). Richmond, Virginia: Virginia Department of Transportation.

HHBC Consulting. (n.d.). *Tresor, Vaults, and Strong Rooms*. HHBC Consulting. https://www.hhbc-consulting.de/kopie-military.

Julian, A., Bishop, B., Ehrlich, G., Flores, C., & Hainer, C. (2014). Standard for the Design and Construction of Storm Shelters. *International Code Council*.

Life Lift Systems. (n.d.). *Vortex Vaults Storm Shelters*. Life Lift Systems. https://vortexvaults.com/.

Lomholt, I., & Welch, A. (2021, February 9). *MUCEM Marseille Building Design*. e-Architect. https://www.e-architect.com/marseille/mucem-museum-marseille.

Malvar, L. J. (1998). Review of Strain Rate Effects for Concrete in Tension. *ACI Materials Journal*, *95*(6). https://doi.org/10.14359/418

Mao, L., Barnett, S., Begg, D., Schleyer, G., & Wight, G. (2014). Numerical simulation of ultra high performance fibre reinforced concrete panel subjected to blast loading. *International Journal of Impact Engineering*, *64*, 91–100. https://doi.org/10.1016/j.ijimpeng.2013.10.003

Naaman, A. E. (1972). A Statistical Theory of Strength for Fiber Reinforced Concrete. *Massachusetts Institute of Technology* .

National Association of Home Builders. (2019). *Tornado Shelters: Guides & Resources for Construction*. Home Innovation Research Labs. https://www.homeinnovation.com/tornadoshelters.

National Association of Home Builders. (2019, April 15). *Forest Service Wood Tornado Shelter Provides Safe, Affordable Storm Protection*. Home Innovation Research Labs. https://www.homeinnovation.com/about/news_and_events/home_innovation_news/2019_0415_forest_service_wood_tornado_shelter_provides_safe_affordable_storm_protection.

NOAA. (2016, August 6). *Tuscaloosa-Birmingham Tornado - April 27, 2011*. National Weather Service. https://www.weather.gov/bmx/event_04272011tuscbirm.

NOAA. (2020). *Annual Fatal Tornado Summary*. NOAA/NWS Storm Prediction Center. https://www.spc.noaa.gov/climo/torn/fatalmap.php#viewDiv.

NOAA. (n.d.). *Tornado Detection*. The National Severe Storms Laboratory. https://www.nssl.noaa.gov/education/svrwx101/tornadoes/detection/.

NOAA. (n.d.). *Tornado Forecasting*. The National Severe Storms Laboratory. https://www.nssl.noaa.gov/education/svrwx101/tornadoes/forecasting/.

NOAA. (n.d.). *Types of Tornados*. The National Severe Storms Laboratory. https://www.nssl.noaa.gov/education/svrwx101/tornadoes/types/.

Nuance Studio. (2020). *Concrete Designer Panels for Interior Design and Facade Design*. Nuance Studio. https://thenuancestudio.com/fuji.html.

Nuclear Energy Institute. (2011). 07-13 Methodology for Performaing Aircraft Impact Assessments for New Plant Designs.

Nöldgen, M., Millon, O., Thoma, K., & Fehling, E. (2009). Hochdynamische Materialeigenschaften von Ultrahochleistungsbeton (UHPC). *Beton- Und Stahlbetonbau*, *104*(11), 717–727. https://doi.org/10.1002/best.200900038

Owens Corning. (n.d.). *Fiberglass Rebar*. Owens Corning. https://www.owenscorning.com/en-us/composites/products/product-types/fiberglass-rebar.

Park, S. H., Kim, D. J., & Kim, S. W. (2016). Investigating the impact resistance of ultra-high-performance fiber-reinforced concrete using an improved strain energy impact test machine. *Construction and Building Materials*, *125*, 145–159. https://doi.org/10.1016/j.conbuildmat.2016.08.027

Protections Shelters. (2020, December 23). *Above Ground Storm Tornado Shelters*. Protection Shelters. https://protectionshelters.com/storm-shelters/above-ground/.

Raymond, Augustus L., "An Exploration into Tornado Resistant Residential CLT Structures" (2019). All eses. 3095. h4ps://tigerprints.clemson.edu/all_theses/3095

Richard, P., & Cheyrezy, M. (1995). Composition of reactive powder concretes. *Cement and Concrete Research*, *25*(7), 1501–1511. https://doi.org/10.1016/0008-8846(95)00144-2

Riedel, W., Nöldgen, M., Straßburger, E., Thoma, K., & Fehling, E. (2010). Local damage to Ultra High Performance Concrete structures caused by an impact of aircraft engine missiles. *Nuclear Engineering and Design*, *240*(10), 2633–2642. https://doi.org/10.1016/j.nucengdes.2010.07.036

RTA. (2021, March 16). *Ready-to-Assemble Panel System*. RTA Outdoor Living. https://rtaoutdoorliving.com/our-technology-approach/.

Safe Sheds. (n.d.). *Small Family Storm Shelter*. Safe Sheds Sales. https://www.safesheds.com/smallfamilystormshelter.html.

Schickhofer, G., & Guggenberger, W. (1994). Elastic Analysis of Flexibly Jointed Laminated Timber Plates. In 1st Congress of Croatian Society of Mechanics, Pula 14-17 Sept 1994: Conference Proceedings

Steelike Concrete. (2021, March 23). https://steelike.com/.

Suwannakarn, S. W. (2009). Post-cracking Characteristics of High Performance Fiber Reinforced Cementitious Composites. *The University of Michigan*.

Tadros, M. K., Sevenker, A., & Berry, R. (2019, April). *Ultra-High-Performance Concrete*. STRUCTURE Magazine. https://www.structuremag.org/?p=14370.

TAKTL. (2021). *TAKTL A-UHPC*. TAKTL Ultra High Performance Concrete. https://www.taktl-llc.com/.

Thai, D. K., & Kim, S. E. (2015). Failure analysis of UHPFRC panels subjected to aircraft engine model impact. *Engineering Failure Analysis*, *57*, 88–104. https://doi.org/10.1016/j.engfailanal.2015.07.005

U.S. Department of Commerce. (2011, April 17). *Tornadoes 101*. National Oceanic and Atmospheric Administration. https://www.noaa.gov/stories/tornadoes-101.

UCAR. (n.d.). *How Tornadoes Form*. How Tornadoes Form | UCAR Center for Science Education. https://scied.ucar.edu/learning-zone/storms/how-tornadoes-form.

Verma, M., Prem, P. R., Rajasankar, J., & Bharatkumar, B. H. (2016). On low-energy impact response of ultra-high performance concrete (UHPC) panels. *Materials & Design*, *92*, 853–865. https://doi.org/10.1016/j.matdes.2015.12.065

WBRC Staff. (2021, March 17). *NWS: EF-2 tornado damage confirmed in Chilton County, EF-1 damage in Moundville*. 6WBRC. https://www.wbrc.com/2021/03/17/tornado-damage-hale-county-moundville/.

Wille, K. (2013, October). *Development of Non-Proprietary Ultra-High-Performance Concrete for Use in The Highway Bridge Sector*. FHWA Techbrief. https://www.fhwa.dot.gov/publications/research/infrastructure/structures/bridge/13100/index.cfm#:~:text=This%20value%2C%20when%20combined%20with,(%241%2C110%2Fm3.

Yoo, D.-Y., & Banthia, N. (2017). Mechanical and structural behaviors of ultra-high-performance fiber-reinforced concrete subjected to impact and blast. *Construction and Building Materials*, *149*, 416–431. https://doi.org/10.1016/j.conbuildmat.2017.05.136

APPENDIX: LOAD CALCULATIONS

Although the focus of this study is on the impact resistance of UHPC panels, another important aspect of tornado shelter design are load calculations from other environmental factors. Wind and flood loads are of particular interest for tornado shelters, as both commonly occur in conjunction with tornado events. Following ASCE 7-10 and ICC/NSSA 500 guidelines, the demand on a 4 ft by 4 ft base and 6 ft tall tornado shelter were calculated. Then, the moment and shear capacity of a 1.75-inch-thick wall and roof component were calculated and compared to the demand to ensure adequate strength was provided. Load Resistance Factored Design (LRFD) principles were used throughout the calculations.

Wind Load

Wind load calculations are covered in ASCE 7-10 Chapters 26 through 31. Values of constants are summarized in **Figure 95**.

Figure 95: Summary of wind load parameters.

Variable	***Value***	***Reference***
K_Z	0.85	ASCE 27.3.1
k_{zt}	1.0	ICC 304.5
K_d	1.0	ICC 304.3
V	250 mph	ICC 304.2
GC_{pi}	±0.55	ICC 304.7 / ICC 702.1.1
G	0.85	ASCE 26.9.1
C_p	0.8 (windward wall) -0.5 (leeward wall) -0.7 (side walls) -1.3 (roof, windward half) -0.7 (roof, leeward half)	ASCE 27.4.1

**q_i will equal q for all cases because the structure is less than 15 ft tall.*

$$q = 0.00256 K_Z k_{zt} K_d V^2 = 136\, psf \tag{14}$$

$$p = qGC_p - q_i\left(GC_{pi}\right) = \begin{cases} 167\, psf\ (windward\ wall) \\ -133\, psf\ (leeward\ wall) \\ -156\, psf\ (side\ walls) \\ -225\, psf\ (roof, windward\ half) \\ -156\, psf\ (roof, leeward\ half) \end{cases} \tag{15}$$

Positive pressures indicate the force acts toward the structure, while negative indicates the force acts away from the structure. Because the UHPC panels are reinforced with steel wire mesh at their center and are therefore symmetric through their depth, they will have the same shear and moment capacity regardless of positive or negative shear and moment directions. The windward wall and roof will be the most critical elements and are the two that will be considered below.

Flood Load

Flood load calculations are covered in ASCE 7-10 Chapter 5. Values of constants are summarized in **Figure 96**.

Figure 96: Summary of flood load parameters.

Variable	***Value***	***Reference***
a	1.25	ASCE 5.4.3
v	10 ft/s	ASCE 5.4.3
g	32.2 ft/s^2	
DFE_o	1 ft	ICC 303.4 / ASCE 5.2
γ	62.4 psf	

$$d_h = \frac{av^2}{2g} = 1.94\ ft \tag{16}$$

$$DFE = DFE_o + d_h = 2.94\ ft \tag{17}$$

$$p = \gamma DFE = 183.5\ psf \tag{18}$$

Flood loads are applied as a triangular distributed load, with maximum pressure at the ground decreasing to zero at the design flood elevation. Rain loads are not considered for this structure because it has a flat roof which will not allow for water accumulation.

Load Combinations

Per ASCE 2.3.3, structures experiencing flood loads will replace *1.0W* with *1.0W+2.0F* in every load combination. Self-weight will not be considered because it is negligible compared to the other loads. With no other loads acting on the structure, the only combination considered will be *1.0W + 2.0F* for the windward wall and *1.0W* for the roof.

RISA 2D Diagrams

The structural analysis program RISA 2D was used to calculate demand on the structure on a per-foot-of-width basis. **Figure 97** shows the loads applied to the windward wall and the resulting bending moment, shear force, and deflection diagrams assuming a fix-fix boundary condition of each end of the panel. **Figure 98** shows the same diagrams for the roof. The maximum deflections are less than the 3 inches of permanent deflection allowed by ICC/NSSA 500.

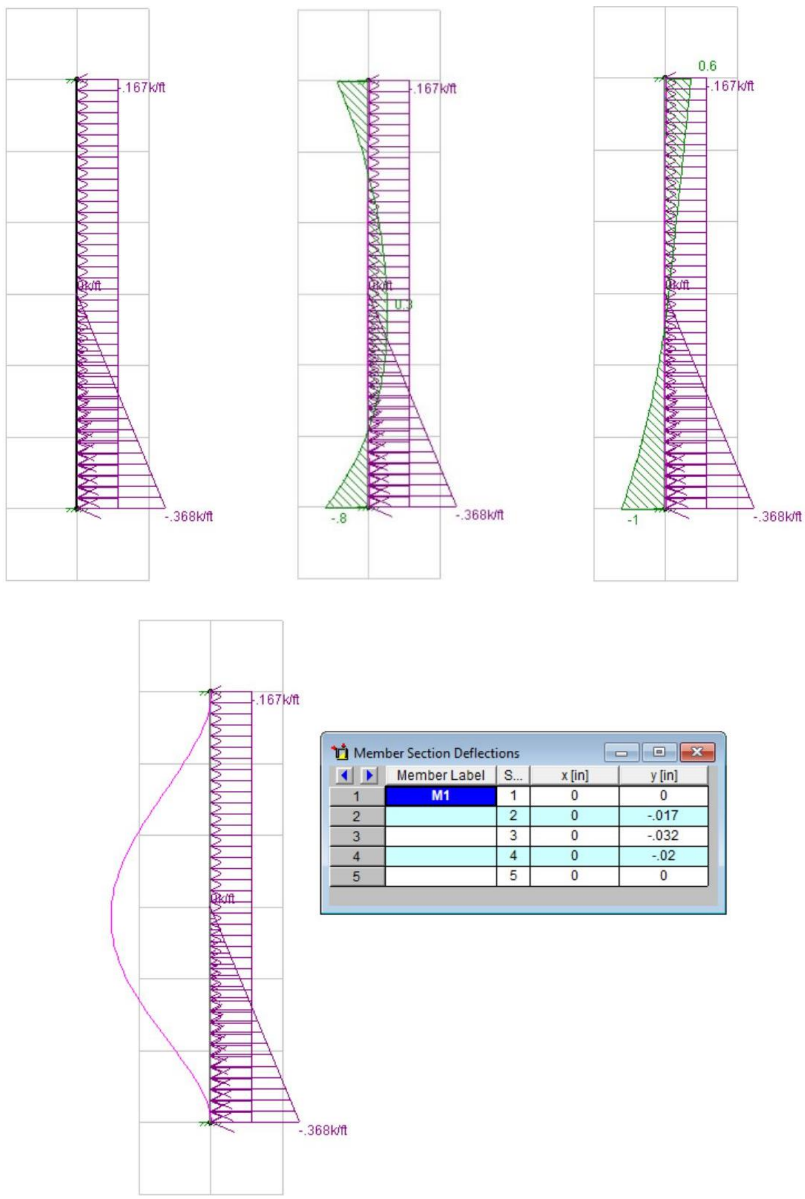

Figure 97: Loading and response of windward wall panel. Top from left to right, distributed loads, bending moment diagram, and shear force diagram for the windward wall. Bottom, deflected shape of the windward wall. Deflection values are in inches.

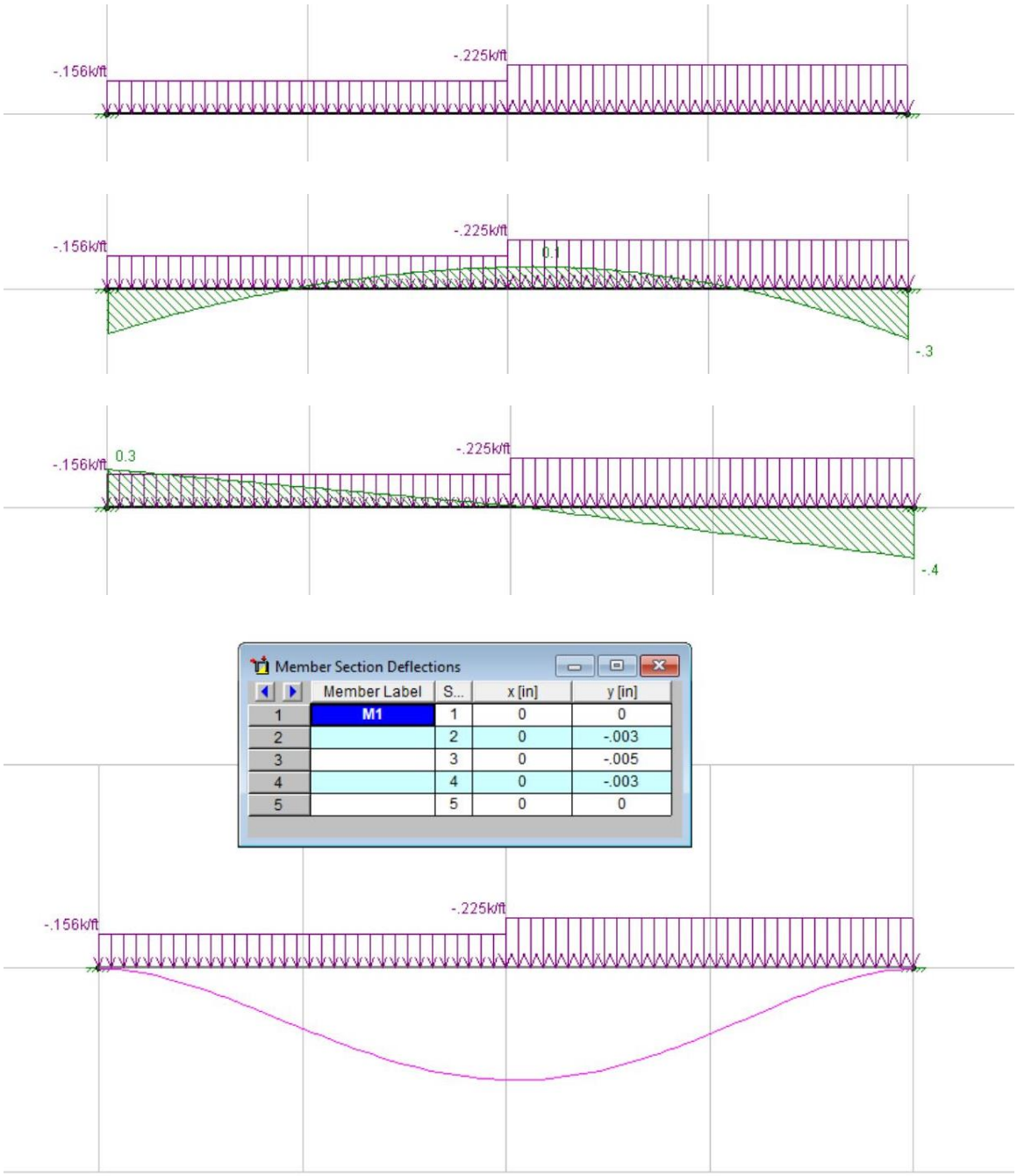

Figure 98: Loading and response of roof panel. From top to bottom, distributed loads, bending moment diagram, shear force diagram, and deflected shape for the roof. Deflection values are in inches.

Moment Capacity of Panel

Steel reinforcement at the center of the panel is 60 ksi steel with a total area of 0.0982 in^2 per foot of UHPC width. A compressive stress of 21 ksi and a tensile stress of 1 ksi from the Material Property Testing Results section were used with the stress distribution in **Figure 99** to calculate the moment capacity of the UHPC panels. A neutral axis of 0.1867 inches from the top of the panel balances the forces.

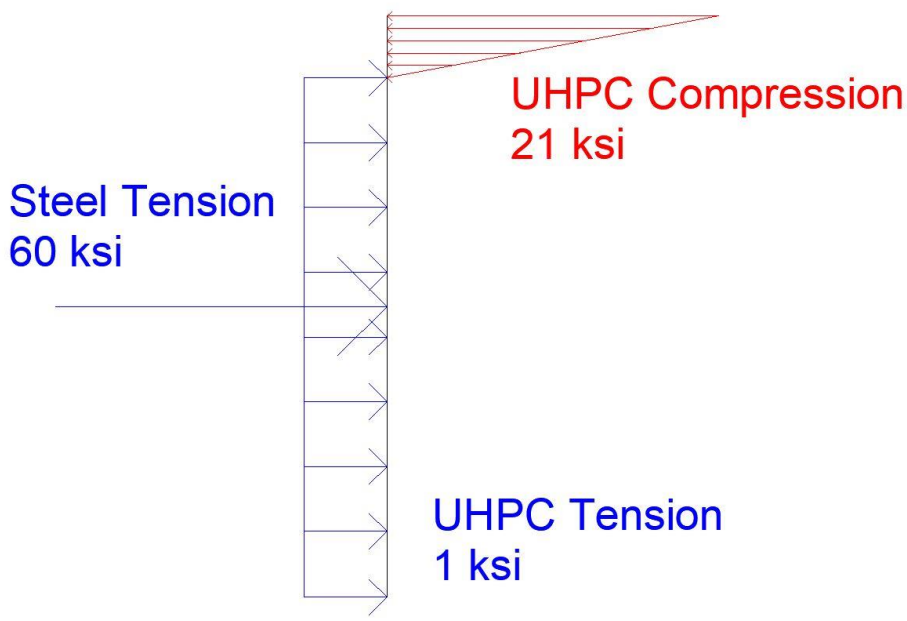

Figure 99: Stress distribution through UHPC cross-section. Neutral axis shown for the 1.75-inch-thick UHPC panel. Steel wire mesh is at the center of the panel.

Calculating the moment about the neutral axis point and applying a reduction factor of 0.9, the moment capacity of the 1.75-inch-thick UHPC panel is 18.2 kip-in, or 1.52 kip-ft.

Shear Capacity of Panel

Using the shear capacity equations given in ACI 318 and a compressive strength of 21 ksi, the following shear capacity is calculated per 1 ft width of the UHPC panel.

$$V_c = 10\phi\sqrt{f'_c}b_w d = 10(0.75)\sqrt{21000psi}\,(12in)(0.875in) = 11.4\ kips \qquad (19)$$

Comparison

The maximum magnitude of moment experienced on either the wall of the roof is 0.8 kip-ft and the maximum shear is 1 kip. Comparing these values with the moment capacity of 1.52 kip-ft and shear capacity of 11.4 kips, the UHPC panel is adequate to resist the other loads associated with tornado events.

APPENDIX: IMPACT TESTING PHOTOS

Figure 100: AG_2x12 impact testing phots. Left, front face and right, back face damage to AG_2x12. The panel failed by punching shear as the projectile went through the panel. Glass fibers can be seen poking out of the UHPC on the front hole. Extensive damage was done to the steel reinforcement, causing the rebar to bend out of the panel and rip UHPC out with it.

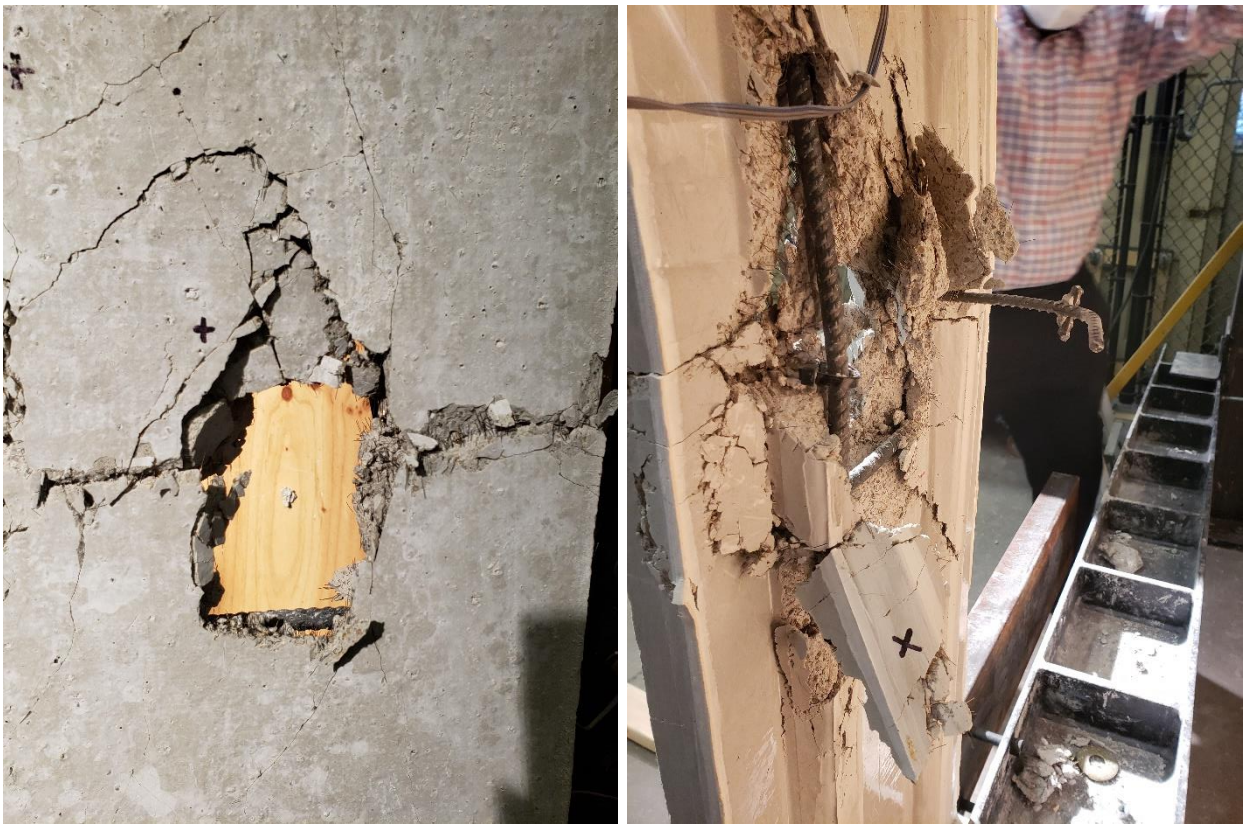

Figure 101: AS_2x12 impact testing photos. Left, front face and right, back face damage to AS_2x12. The panel failed by punching shear as the projectile went through the panel. Chunks of UHPC were ejected from the panel and lodged in the plywood on the wall behind the steel frame. Large amounts of damage were done to the steel reinforcement, causing it to tear out of the concrete.

Figure 102: AS_1.25x12 impact testing photos. Top left, before testing with the witness screen behind the panel; top right, after testing with multiple shear cracks marked on the front face of the panel; bottom left, after testing with cracks marked on the side of the panel and no damage to the witness frame; and bottom right, after testing with flexural cracks on the back face of the panel.

Figure 103: AS_1.625x12 impact testing photos. Top left, before testing; top right, after testing with multiple shear cracks marked on the front face of the panel; bottom left, after testing with cracks marked on the side of the panel, no damage to the witness frame, and a small permanent deformation; and bottom right, after testing with flexural cracks on the back face of the panel.

Figure 104: AS_1.25x24 impact testing phots. Top left, before testing; top right, after testing with a circular crack pattern marked on the front face of the panel; bottom left, after testing with cracks marked on the side of the panel, no damage to the witness frame and no permanent deformation observed; and bottom right, after testing with a very small flexural crack marked on the back face of the panel.

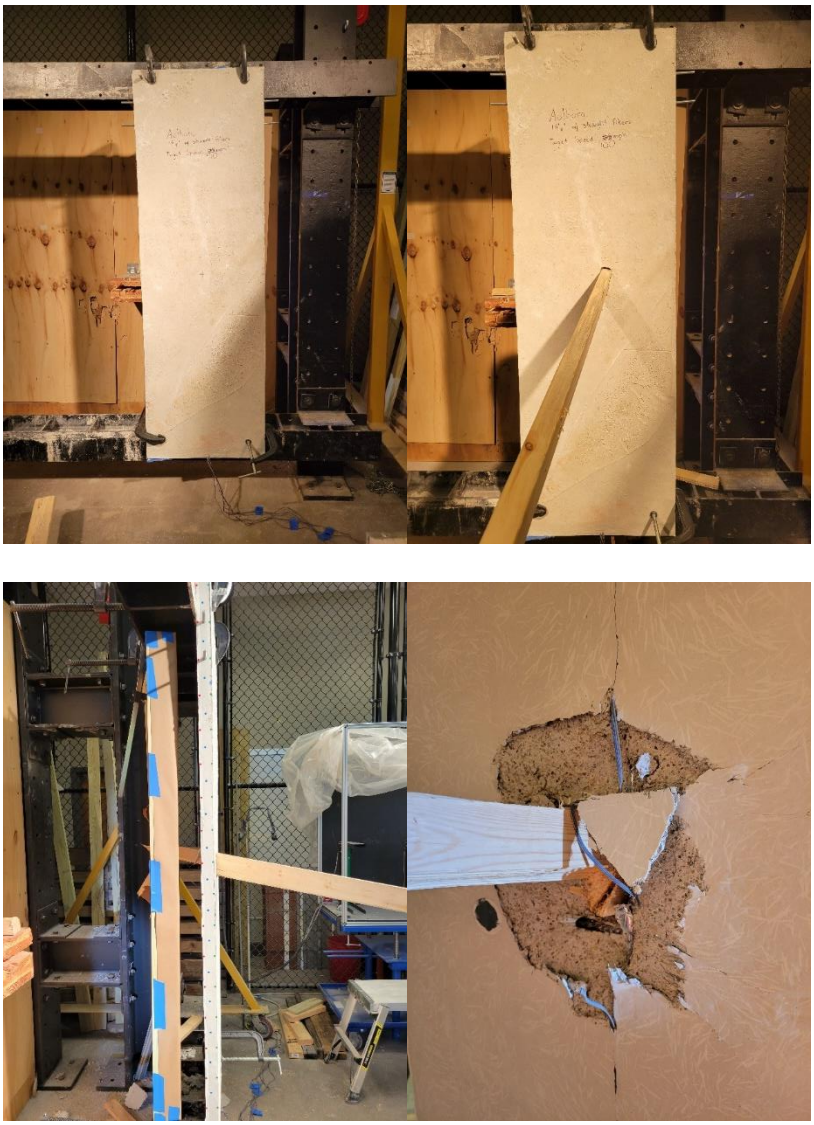

Figure 105: AS_1.625x24 impact testing photos. Top left, before testing; top right, after the 2x4 projectile protruding from the front of the panel; bottom left, after testing with the 2x4 projectile having punched through the panel and the witness screen; and bottom right, after testing with the back-face scabbing associated with the punching shear failure.

Figure 106: SS_1.25x12 impact testing photos. Top left, before testing; top right, after testing with a circular crack pattern marked on the front face of the panel; bottom left, after testing with a small but noticeable permanent deflection and no damage to the witness frame; and bottom right, after testing with a flexural crack on the back face of the panel.

Figure 107: SB_1.25x12 impact testing photos. Top left, before; top right, after testing with multiple shear cracks marked on the front face of the panel; bottom left, after testing with a crack marked on the side of the panel and no damage to the witness frame; and bottom right, after testing with one flexural crack on the back face of the panel.